



University of  
Stavanger

Faculty of Science and Technology

## MASTER'S THESIS

Study program/Specialization:

**Offshore Technology/Marine and Subsea**

Spring semester, 2016

**Open**

Writer:

**Muhammad Ahmad Tauqeer**

Faculty supervisor:

**Prof. Muk Chen Ong**

Title of thesis:

**Geometry Optimization of Glass Reinforced Plastic (GRP) Subsea Protection Covers**

Credits (ECTS): 30

Key words:

*Pipeline cover, GRP, Protection cover, Subsea, Computational fluid dynamics, Finite element method, On-bottom stability, Fishing loads, Drop-object impact, Drag coefficient, lift coefficient*

Pages: 110

Enclosure: Appendix + 1 CD

**Stavanger, 15-06-2016**



NOTE: 'Society of Petroleum Engineers style-guide' document layout is followed in this thesis and Harvard referencing style is adopted for citation purpose.

(Intentionally left blank)

# *Abstract*

Subsea pipelines are exposed to fishing activity loads and drop-object impacts. Protection covers are used to protect the pipelines from these loads and are manufactured from Glass Reinforced Plastics (GRP) for high strength to weight ratio, manufacturability and low cost. These covers have the primary requirement to protect the pipelines from the loads that they are not designed for, such as loads from the offshore fishing activity and drop-objects. Furthermore, a GRP cover is also exposed to other loading conditions like transportation, installation, lowering through splash zone and on-bottom stability. In all the loading conditions identified, on-bottom stability analysis, fishing activity and drop-object impact loads are the design governing loading conditions. Square, triangular and semi-circular GRP cover geometries are selected for the present study. A sensitivity analysis of the selected GRP cover cross-sections is carried out for the three aforementioned GRP covers under different governing loading conditions.

The current thesis includes a numerical study of square, triangular and semi-circular GRP cover geometries under different loads and a discussion on the geometry optimization, which can assist protection cover designers as an initial design guideline. In order to analyse the GRP cover geometries, hydrodynamic force coefficients are required to compute the forces since hydrodynamic force coefficients data was absent in the open literature. This data is necessary for the present study. Therefore, Computational Fluid Dynamics (CFD) simulations are performed to calculate hydrodynamic force coefficients of the selected geometries. Steady state Reynolds-Averaged Navier-Stokes equations (RANS) with the standard  $k-\epsilon$  turbulence model under seabed boundary layer flow are used to calculate the hydrodynamic force coefficients. The present study further reveals that the square geometry cover has a drag coefficient of  $0.90$  and lift coefficient of  $0.65$ , triangular geometry cover has a drag coefficient of  $0.80$  and lift coefficient of  $0.15$  and semi-circular geometry cover has a drag coefficient of  $0.23$  and lift coefficient of  $1.40$  on average for different boundary layer thicknesses. These drag and lift coefficients are further used for the on-bottom stability analysis of the GRP covers.

The on-bottom stability analysis is carried out using Morrison equations for two different sea states. It concluded that the triangular cover has the highest stability for vertical forces while semi-circular cover has the highest lateral stability.

In fact, fishing activity loads are one of the significant loads for the GRP covers. Finite Element Method (FEM) is used to calculate the load-bearing capacity of the three covers for these loads. Semi-circular geometry cover is determined to be suitable in bearing fishing activity loads as compared to the other two geometry covers.

Similarly, offshore drop-objects are also one of the significant loads for the GRP covers. Drop-object impact analysis is carried out by subjectively selecting offshore drop-objects such as offshore equipment and fishing gear. Impact energies of the selected drop-objects are calculated using energy conservation. The impact absorption capacity of the GRP covers is calculated using FEM. Finally, the calculated impact energies of the drop-objects are compared with the calculated impact absorption capacity of each cover. It is concluded that the semi-circular cover is the most suitable cover among the covers analysed in bearing drop-object impact loads.

The present study inferred that each GRP cover has its own pros and cons. Therefore, it is recommended that the cover geometry should be selected based upon the exposed loading conditions to the cover.

## *Acknowledgements*

I would like to pay my gratitude to Prof. Muk Chen Ong for his consistent support and motivation throughout the completion of this thesis. His remarkable and gracious benefactions through word and perception has been of countless worth.

Secondly, I am grateful to the PhD candidate Zhong Li who has made available his support in a number of ways.

Thirdly, the numerical simulations presented in this thesis are conducted on Vilje (super computer) operated by NOTUR. I would acknowledge this high computational power support granted by NOTUR, which helped me finish the simulations within timeframe.

Lastly, I offer my regards to my parents Tauqeer Ahmad and Farnaz Tabassum for their deep affection and motivational support in all the challenges that I have been through in my life.

(Intentionally left blank)



# *Table of Contents*

## Chapter 1

Introduction .....	1
1.1 Hydrodynamic force coefficients.....	2
1.1.1 Hydrodynamic drag coefficient.....	3
1.1.2 Hydrodynamic lift coefficient .....	4
1.1.3 Reynolds number .....	5
1.2 On-bottom stability.....	5
1.2.1 Vertical stability .....	5
1.2.2 Lateral stability .....	6
1.3 Fishing activity loads.....	7
1.4 Drop-object impact analysis .....	8
1.5 Objectives of this thesis.....	9
1.6 Outline of this thesis.....	9

## Chapter 2

Hydrodynamic force coefficients of GRP covers.....	11
2.1 Introduction .....	11
2.1.1 Literature review.....	12
2.1.2 Overview of the study in this Chapter .....	13
2.1.3 Nomenclature .....	14
2.2 Basic theory of fluid flow .....	15
2.2.1 Flow physics.....	15
2.2.2 Turbulence modelling .....	17
2.2.3 Turbulent boundary layer flow .....	18
2.2.4 Mass and momentum conservation .....	20
2.2.5 Turbulence model .....	21
2.2.6 Lift and drag forces acting on the body .....	22
2.3 Mesh and boundary conditions.....	23
2.3.1 Domain .....	23
2.3.2 Mesh set-up.....	25

2.3.3	Boundary Conditions	30
2.3.4	Similarity parameters	33
2.4	Numerical set-up validation study	34
2.4.1	Mesh and domain convergence	34
2.5	Results comparison with Fujimoto et al. (1975)	36
2.5.1	Force coefficients:	36
2.6	Results	37
2.6.1	Drag coefficient, lift coefficient and recirculation length	37
2.6.2	Velocity profiles at different locations of the three GRP covers	40
2.6.3	Velocity contours	47
2.6.4	Streamlines	50
2.7	Conclusion	52

## Chapter 3

	On-bottom stability analysis	53
3.1	Introduction	53
3.2	Static stability	53
3.3	Dynamic stability	56
3.3.1	Assumptions	56
3.3.2	Sea State	57
3.3.3	Hydrodynamic force coefficients	57
3.3.4	Wave Velocity and Acceleration	58
3.3.5	Morrison equation applicability	60
3.3.6	Vertical force	61
3.3.7	Horizontal force	62
3.4	Conclusion	64

## Chapter 4

	Fishing activity loads	65
4.1	Introduction	65
4.1.1	Trawl-net friction	66
4.1.2	Trawlboard overpull	66
4.1.3	Trawlboard impact	67

4.2	Theory of the GRP material	68
4.2.1	Orthotropic material	68
4.2.2	Cartesian coordinate system	68
4.2.3	Stress	69
4.2.4	Strain	69
4.2.5	Hooke's law	70
4.2.6	Engineering constants	71
4.3	Finite element analysis	73
4.4	Material model	74
4.5	Failure criterion	75
4.6	Load and resistance factors	76
4.6.1	Summary of load factors (resistance and load)	77
4.6.2	Geometry of the GRP covers	78
4.6.3	Mesh	79
4.7	Trawl-net friction loading	81
4.7.1	Loading and constraint for trawl-net friction loading	81
4.7.2	Results of trawl-net friction loading	83
4.7.3	Results discussion of trawl-net friction loading	84
4.8	Trawl-board overpull loading	85
4.8.1	Loading and constraint of trawl-board overpull loading	86
4.8.2	Results, trawl-board overpull	88
4.8.3	Results discussion of trawl-board overpull loading	89
4.9	Conclusion	90

## Chapter 5

	Assessment of impact damage caused by drop-objects on glass reinforced plastic (GRP) covers	91
5.1	Introduction	91
5.2	Impact energy	92
5.2.1	Terminal velocity	92
5.2.2	Selection of drag coefficient	93
5.2.3	Calculation of impact energies	94
5.2.4	Converged solution	95
5.2.5	Discussion	96
5.3	Impact absorption capacity	98

5.3.1	Drop-object impact modelling	98
5.3.2	Results discussion	98
5.3.3	Square cover	98
5.3.4	Triangular geometry	99
5.3.5	Semi-circular geometry	100
5.4	Conclusion	101

## Chapter 6

Conclusion	103
Recommended future work	105
References	106

<i>Appendix A</i>	i
<i>Appendix B</i>	iii
<i>Appendix C</i>	vii
<i>Appendix D</i>	xix

# *List of Figures*

Figure 1.1 GRP protection covers taken from PJNC (2016) .....	2
Figure 1.2 Fluid flow over a body partially immersed taken from Cengel & Cimbala (2010) ..	2
Figure 1.3 Fluid flow over a circular body taken from Cengel & Cimbala (2010) .....	4
Figure 2.1 Subsea GRP protection covers adapted from CSUB (2016) .....	11
Figure 2.2 A typical flow around GRP cover taken from the present simulations .....	13
Figure 2.3 Schematic illustration of a boundary layer flow over square GRP cover placed on the seabed.....	14
Figure 2.4 Schematic illustration of boundary layer flow over triangular GRP cover placed on the seabed.....	15
Figure 2.5 Schematic illustration of boundary layer flow over semi-circular GRP cover placed on the seabed.....	15
Figure 2.6 Vortex shedding taken from Sumer & Fredsøe (1997).....	16
Figure 2.7 Laminar and turbulent flow taken from Versteeg & Malalasekera (2007).....	17
Figure 2.8 Turbulent instantaneous velocity variation with respect to time taken from Versteeg & Malalasekera (2007) .....	17
Figure 2.9 Energy cascade taken from Ecke (2005) .....	18
Figure 2.10 Boundary layer flow over a flat plate taken from Frei (2013) .....	19
Figure 2.11 Boundary layer regions modified from Versteeg & Malalasekera (2007).....	20
Figure 2.12 Computational domain of square GRP cover .....	24
Figure 2.13 Computational domain of triangular GRP cover .....	25
Figure 2.14 Computational domain of semi-circular GRP cover .....	25
Figure 2.15 Block topology of square geometry cover.....	26
Figure 2.16 Block topology of triangular geometry cover .....	27
Figure 2.17 Block topology of semi-circular geometry cover.....	27
Figure 2.18 Law of wall approach and first node height .....	27
Figure 2.19 Average $y^+$ convergence algorithm.....	28
Figure 2.20 Global mesh of square geometry cover for $\delta/D = 0.73$ and $Re_D = 1.19 \times 10^5$ ....	28
Figure 2.21 Local mesh of square geometry cover for $\delta/D = 0.73$ and $Re_D = 1.19 \times 10^5$ .....	29
Figure 2.22 Global mesh of triangular geometry cover for $\delta/D = 0.73$ and $Re_D = 1.00 \times 10^6$ .....	29
Figure 2.23 Local mesh of triangular geometry cover for $\delta/D = 0.73$ and $Re_D = 1.00 \times 10^6$ ..	29
Figure 2.24 Global mesh of semi-circular geometry cover for $\delta/D = 0.73$ and $Re_D = 1.00 \times 10^6$ .....	30
Figure 2.25 Local mesh of semi-circular geometry cover for $\delta/D = 0.73$ and $Re_D = 1.00 \times 10^6$ .....	30

Figure 2.26 Boundary conditions, square GRP cover.....	31
Figure 2.27 Boundary conditions, triangular GRP cover.....	31
Figure 2.28 Boundary conditions, semi-circular GRP cover.....	31
Figure 2.29 Fitted logarithmic boundary layer profile on experimental boundary layer from Fujimoto et al. (1975) at the upstream location.....	33
Figure 2.30 Comparison of $C_D$ numerical and experimental results (Fujimoto et al., 1975) for $\delta/D = 0.73, 1.70$ & $2.55$ .....	37
Figure 2.31 Locations of velocity profiles plotted on the square cover.....	41
Figure 2.32 Velocity profiles on the square cover at different locations.....	42
Figure 2.33 Velocity profiles on the square cover at different locations.....	43
Figure 2.34 Locations of velocity profiles plotted on the triangular cover.....	44
Figure 2.35 Velocity profiles on the triangular cover at different locations.....	45
Figure 2.36 Locations of velocity profiles plotted on the semi-circular cover.....	45
Figure 2.37 Velocity profiles on the semi-circular cover at different locations.....	46
Figure 2.38 Velocity contours for the square cover a) $\delta/D = 0.73, Re = 1.19 \times 10^5$ b) $\delta/D = 1.70, Re = 5.12 \times 10^4$ c) $\delta/D = 2.55, Re = 3.41 \times 10^4$ .....	47
Figure 2.39 Velocity contours for the square cover a) $\delta/D = 0.73, Re = 1.0 \times 10^6$ b) $\delta/D = 1.70, Re = 1.0 \times 10^6$ c) $\delta/D = 2.55, Re = 1.0 \times 10^6$ .....	48
Figure 2.40 Velocity contours for the triangular cover a) $\delta/D = 0.73, Re = 1.0 \times 10^6$ b) $\delta/D = 1.70, Re = 1.0 \times 10^6$ c) $\delta/D = 2.55, Re = 1.0 \times 10^6$ .....	49
Figure 2.41 Velocity contours for the semi-circular cover a) $\delta/D = 0.73, Re = 1.0 \times 10^6$ b) $\delta/D = 1.70, Re = 1.0 \times 10^6$ c) $\delta/D = 2.55, Re = 1.0 \times 10^6$ .....	49
Figure 2.42 Streamlines on the square cover a) $\delta/D = 0.73, Re = 1.19 \times 10^5$ b) $\delta/D = 1.70, Re = 5.12 \times 10^4$ c) $\delta/D = 2.55, Re = 3.41 \times 10^4$ d) $\delta/D = 0.73, Re = 1.0 \times 10^6$ e) $\delta/D = 1.70, Re = 1.0 \times 10^6$ f) $\delta/D = 2.55, Re = 1.0 \times 10^6$ .....	50
Figure 2.43 Stream lines on the triangular cover a) $\delta/D = 0.73, Re = 1.0 \times 10^6$ b) $\delta/D = 1.70, Re = 1.0 \times 10^6$ c) $\delta/D = 2.55, Re = 1.0 \times 10^6$ .....	51
Figure 2.44 Stream lines on the semi-circular cover a) $\delta/D = 0.73, Re = 1.0 \times 10^6$ b) $\delta/D = 1.70, Re = 1.0 \times 10^6$ c) $\delta/D = 2.55, Re = 1.0 \times 10^6$ .....	51
Figure 3.1 The horizontal and vertical forces calculation scheme.....	56
Figure 4.1 A typical fishing gear (figure developed for this thesis).....	65
Figure 4.2 Schematic, trawlboard overpull (figure developed for this thesis).....	66
Figure 4.3 Impact convergence algorithm.....	67
Figure 4.4 Stress components in three directions.....	69
Figure 4.5 Simple stress states used for engineering parameters (Gibson, 1994).....	71
Figure 4.6 The geometry of the square GRP cover.....	78
Figure 4.7 The geometry of the triangular GRP cover.....	79
Figure 4.8 The geometry of the semi-circular GRP cover.....	79
Figure 4.9 The mesh used on square cover.....	80

Figure 4.10 The mesh used on triangular cover .....	80
Figure 4.11 The mesh used on semi-circular cover .....	80
Figure 4.12 A typical trawl-net friction over GRP cover (figure developed for this thesis) .....	81
Figure 4.13 Load and constraint for trawl-net friction loading on square cover .....	82
Figure 4.14 Load and constraint for trawl-net friction loading on triangular cover .....	82
Figure 4.15 Load and constraint for trawl-net friction loading on semi-circular cover .....	82
Figure 4.16 Equivalent stress for trawl-net friction loading on square cover .....	83
Figure 4.17 Equivalent stress for trawl-net friction loading on triangular cover .....	83
Figure 4.18 Equivalent stress, trawl-net friction loading on semi-circular cover .....	84
Figure 4.19 Load distribution of trawl-board overpull on a GRP cover .....	86
Figure 4.20 Load and constraint of trawl-board overpull on a square cover .....	87
Figure 4.21 Load and constraint of trawl-board overpull on triangular cover .....	87
Figure 4.22 Load and constraint of trawl-board overpull on a semi-circular cover .....	87
Figure 4.23 Equivalent stress for trawl-board overpull on square cover .....	88
Figure 4.24 Equivalent stress of trawl-board overpull on triangular cover .....	88
Figure 4.25 Equivalent stress of trawl-board overpull on semi-circular cover .....	89
Figure 5.1 Terminal velocity calculation algorithm .....	94
Figure 5.2 Impact absorption capacity of square GRP cover at different locations .....	99
Figure 5.3 Impact absorption capacity of triangular GRP cover at different locations .....	100
Figure 5.4 Impact absorption capacity of semi-circular GRP cover at different locations .....	101
Figure 6.1 Hybrid cover cross-sections .....	105

(Intentionally left blank)



# *List of Tables*

Table 2.1 Skewness mesh metrics spectrum taken from Bakker (2006) .....	26
Table 2.2 Hydrodynamic quantities from grid convergence study for square cover at experimental parameters ( $\delta/D = 0.73, 1.70$ & $2.55$ at $Re_D = 1.19 \times 10^5, 5.12 \times 10^4$ & $3.41 \times 10^4$ ) .....	35
Table 2.3 Hydrodynamic quantities from given domain height when $\delta/D = 0.73$ and $Re_D = 1.19 \times 10^5$ .....	35
Table 2.4 Hydrodynamic quantities for square cross-section compared to the equivalent values from experiments performed by Fujimoto et al. (1975) .....	36
Table 2.5 $C_D, C_L$ and $x_R/D$ of square geometry .....	38
Table 2.6 $C_D, C_L$ and $x_R/D$ of triangular geometry .....	39
Table 2.7 $C_D, C_L$ and $x_R/D$ of semi-circular geometry .....	40
Table 3.1 Summary of the results of static vertical stability .....	55
Table 3.2 Sea state data for 1-year and 10-year return conditions .....	57
Table 3.3 Hydrodynamic force coefficients for the geometries .....	58
Table 3.4 Summary of wave results for 1-year and 10-year return conditions .....	60
Table 3.5 Summary of the vertical forces for 10-year waves with 1-year return current .....	61
Table 3.6 Summary of vertical forces for 1-year waves with 10-year return current .....	61
Table 3.7 Summary of horizontal forces for 10-year waves and 1-year return current .....	62
Table 3.8 Summary of horizontal forces for 1-year waves and 10-year return current .....	62
Table 3.9 Summary of maximum utilization of horizontal force against frictional force .....	63
Table 4.1 Orthotropic material properties .....	74
Table 4.2 Load and resistance factors .....	76
Table 4.3 Load and resistance factors .....	78
Table 4.4 Summary of equivalent stress for trawlnet friction loading .....	85
Table 4.5 Summary of equivalent stress for trawlnet overpull .....	90

(Intentionally left blank)

# List of Symbols

$a$	WAVE AMPLITUDE
$a_u$	HORIZONTAL VELOCITY ACCELERATION
$a_v$	VERTICAL VELOCITY ACCELERATION
$A$	PROJECTED AREA
$B$	BUOYANCY FORCE
$C_a$	COEFFICIENT OF ADDED MASS
$C_D$	DRAG COEFFICIENT
$C_l$	LIFT COEFFICIENT
$d$	WATER DEPTH
$D$	STRUCTURE HEIGHT
$D_f$	FRICTION DRAG
$D$	HYDRAULIC DIAMETER
$D_p$	PRESSURE DRAG
$F$	SURFACE ROUGHNESS
$F_D$	DRAG FORCE
$F_L$	LIFT FORCE
$F_f^*$	NORMALIZED FRICTION FORCE
$g$	GRAVITATIONAL ACCELERATION
$h_p$	FIRST NODE HEIGHT
$H$	DOMAIN HEIGHT
$H_s$	SIGNIFICANT WAVE HEIGHT
$L_U$	DISTANCE BETWEEN DOMAIN INLET AND GRP COVER
$L_D$	DISTANCE BETWEEN GRP COVER AND DOMAIN OUTLET
$M$	MASS OF COVER
$Ma$	MACH NUMBER
$N$	NET FORCE
$p$	PRESSURE
$Re_D$	REYNOLDS NUMBER BASED ON STRUCTURE HEIGHT 'D'
$Re_{Dh}$	REYNOLDS NUMBER BASED ON HYDRAULIC DIAMETER $D_h$
$s_g$	SPECIFIC GRAVITY
$S$	EQUIVALENT STRESS
$t$	TIME
$T_p$	PEAK PERIOD
$u$	HORIZONTAL VELOCITY

$u_t$	<i>SHEAR VELOCITY</i>
$u'$	<i>INSTANTANEOUS VELOCITY</i>
$u^+$	<i>RATIO OF THE VELOCITY TO THE SHEAR VELOCITY</i>
$U$	<i>UTILIZATION</i>
$U_\infty$	<i>FREE STREAM VELOCITY</i>
$v$	<i>VERTICAL VELOCITY</i>
$V$	<i>VOLUME OF DISPLACED WATER</i>
$V_{cover}$	<i>VOLUME OF COVER</i>
$v_c$	<i>CURRENT VELOCITY</i>
$W$	<i>SUBMERGED WEIGHT</i>
$x_R$	<i>RECIRCULATION LENGTH</i>
$X_1$	<i>HORIZONTAL AXIS</i>
$X_2$	<i>VERTICAL AXIS</i>
$X_3$	<i>OUT OF THE PLANE AXIS</i>
$y$	<i>VERTICAL DISTANCE NORMAL TO THE WALL</i>
$y^+$	<i>NON-DIMENSIONAL VERTICAL DISTANCE</i>
$\rho$	<i>DENSITY OF THE FLUID</i>
$\rho_{grp}$	<i>DENSITY OF GRP</i>
$\rho_{sw}$	<i>DENSITY OF SEA WATER</i>
$\Delta$	<i>BOUNDARY LAYER THICKNESS</i>
$\Phi$	<i>FRICTION ANGLE</i>
$\gamma_w$	<i>SAFETY FACTOR</i>
$\tau$	<i>FRICTION PER UNIT AREA</i>
$\theta$	<i>ANGLE AT A PERTICULAR LOCATION</i>
$\nu$	<i>KINEMATIC VISCOSITY</i>
$\mu$	<i>DYNAMIC VISCOSITY</i>
$\delta$	<i>BOUNDARY LAYER THICKNESS</i>
$\gamma$	<i>PEAK ENHANCEMENT FACTOR</i>
$\omega$	<i>ANGULAR FREQUENCY</i>
$\mu_s$	<i>STATIC FRICTION FACTOR</i>
$\sigma_{ij}$	<i>STRESS ON <math>ij</math> PLANE</i>
$\tau_{ij}$	<i>SHEAR STRESS ON <math>ij</math> PLANE</i>
$\epsilon_{ij}$	<i>STRAIN ON <math>ij</math> PLANE</i>
$\gamma_{ij}$	<i>SHEAR STRAIN ON <math>ij</math> PLANE</i>

# Abbreviations

<i>AUV</i>	<i>AUTONOMOUS UNDERWATER VEHICLE</i>
<i>CAD</i>	<i>COMPUTER AIDED DESIGN</i>
<i>CFD</i>	<i>COMPUTATIONAL FLUID DYNAMICS</i>
<i>DNS</i>	<i>DIRECT NUMERICAL SIMULATIONS</i>
<i>DNV</i>	<i>DET NORSKE VERITAS</i>
<i>FEM</i>	<i>FINITE ELEMENT METHOD</i>
<i>GRP</i>	<i>GLASS REINFORCED PLASTICS</i>
<i>LES</i>	<i>LARGE EDDY SIMULATIONS</i>
<i>NPD</i>	<i>NORWEGIAN PETROLEUM DIRECTORATE</i>
<i>OS</i>	<i>OFFSHORE STANDARD</i>
<i>QRA</i>	<i>QUANTITATIVE RISK ASSESMENT</i>
<i>RANS</i>	<i>REYNOLDS-AVERAGED NAVIER-STOKES</i>
<i>RP</i>	<i>RECOMMENDED PRACTICE</i>
<i>ROV</i>	<i>REMOTELY OPERATED VEHICLE</i>
<i>2D</i>	<i>TWO-DIMENSIONAL</i>
<i>3D</i>	<i>THREE-DIMENSIONAL</i>

(Intentionally left blank)

# *Chapter 1*

## Introduction

Subsea pipelines are used to transport oil and gas from one location to another. These pipelines are exposed to fishing activity loads as well as drop-objects. Fishing activities have the possibility to cause damage to these pipelines. Several pipeline damage accidents by fishing activities or drop-objects have taken place in different parts of the world. Unlike other parts of the world, North Sea has significant fishing activities along with the offshore oil & gas activities (Liu et al., 2013).

Different measures are implemented to protect the pipelines from fishing activity loads or drop-objects. Some of the commonly used measures are pipeline routing, trenching etc. Subsea protection covers are one of these tentative measures. Subsea protection covers are being manufactured from concrete as well as Glass Reinforced Plastic (GRP). Currently, most of the subsea protection covers are manufactured from GRP because of its low cost and lightweight. The lightweight of GRP covers minimizes installation complications as compared to concrete covers.

As the oil and gas industry is moving towards cost-optimized solutions, a room for the study of GRP subsea cover optimization exists. Through the literature review, it is identified that no research study on the geometry optimization of GRP covers is conducted until date.

In this thesis, three different GRP cover geometries are presented for the hydrodynamic force coefficients, on-bottom stability, fishing and drop-object loads. Square, triangular and semi-circular cover geometries are the three geometries selected for the present study. Typical square GRP covers with chamfered edges in a stacked arrangement are shown in Figure 1.1.



Figure 1.1 GRP protection covers taken from PJNC (2016)

### 1.1 Hydrodynamic force coefficients

When a solid body (in our case GRP cover) is placed in a uniform fluid current, the fluid interacts with the body and induces certain forces. When fluid approaches the body, the body acts as an obstacle for fluid flow and the velocity of fluid changes. Moreover, the fluid imposes a force due to its inertia and attempts to move across the body as shown in the Figure 1.2 for the case of a cylinder. Due to no slip condition, the layer of the fluid in contact with the body is static. Different boundary layers are formed above the body due to the fluid viscosity. The flow separates from the body due to inertia. A recirculation region or separation bubble is created at the downstream of the cylinder. Hydrodynamic forces are induced on the cylinder because of pressure differences on the different sides of the cylinder according to Cengel & Cimbala (2010).

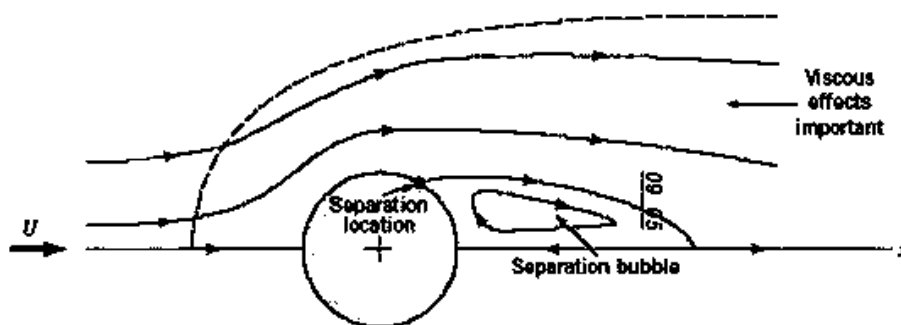


Figure 1.2 Fluid flow over a body partially immersed taken from Cengel & Cimbala (2010)



The nature and magnitude of these induced forces are influenced by many factors i.e. shape of the body, Reynolds number, angle of attack, roughness factor of the body, effect of 3D or 2D flow, flow separation point, length of flow recirculation region, etc. Due to these dependencies, the principles of the fluid-body interaction forces cannot be explained through simple mathematical relations or physical laws. Efforts have been made to minimize these dependencies by combining or defining them together, in order to make the calculation of fluid-body interaction forces as simple as possible. Hydrodynamic force coefficients are introduced to achieve this goal. Hydrodynamic force coefficients are the quantities that are used to compare hydrodynamic forces non-dimensionally on a structure. These coefficients are calculated experimentally or through Computational Fluid Dynamics (CFD) simulations for different geometries. These coefficients accommodate many of the dependencies on which the magnitude and nature of forces are based on. Hence, instead of introducing all the defining factors in the mathematical calculations of forces, these coefficients are introduced. The two most important coefficients that are used for the calculation of lift and drag forces are drag and lift coefficients.

### 1.1.1 Hydrodynamic drag coefficient

A body within a constant fluid flow experiences two types of drags i.e. pressure drag and friction drag. Pressure drag is due to the difference in the pressure between the upstream region and downstream region. For a body with projected area  $A$ , friction per unit area  $\tau$ , with pressure  $p$  acting on an infinitesimally small area  $dA$  (shown in Figure 1.3), placed in a fluid of free stream velocity  $U_\infty$ , with an angle  $\theta$  at a particular location, the pressure drag  $D_p$  is calculated through following mathematical relation, (Cengel & Cimbala, 2010)

$$D_p = \int p dA \cos\theta \quad (1.1)$$

Friction drag  $D_f$  is due to the no slip condition and viscosity in the fluid and calculated through following mathematical relation, (Cengel & Cimbala, 2010) for the case defined in Figure 1.3:

$$D_f = \int \tau dA \sin\theta \quad (1.2)$$

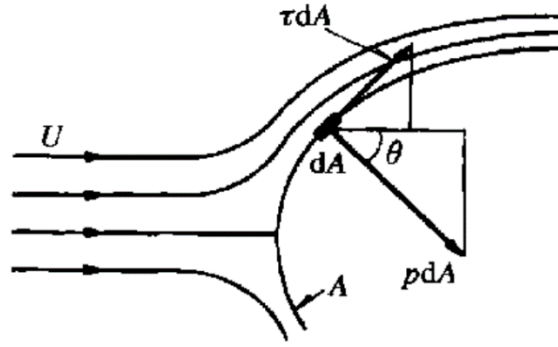


Figure 1.3 Fluid flow over a circular body taken from Cengel & Cimbala (2010)

The integrations of these relations are very complex processes as a number of different factors change as we move across the area. To make the calculations simple, an experimental relation is introduced which accommodates both of the above relations and does not require any complex integration.

$$F_D = C_D A \frac{\rho U_\infty^2}{2} \quad (1.3)$$

where,  $F_D$  is the drag force and  $C_D$  is hydrodynamic drag coefficient. It is calculated either experimentally or by performing Computational Fluid Dynamic (CFD) simulations for every specific body and eliminates all the complexity from the calculations.

### 1.1.2 Hydrodynamic lift coefficient

Similar to drag force, lift force calculation also requires complex integrations and introduction of many factors to achieve the desirable results. Therefore, the experimentally developed simplified relation between lift force and the lift coefficient (Cengel & Cimbala, 2010) is as following:

$$F_L = C_l A \frac{\rho U_\infty^2}{2} \quad (1.4)$$

where  $F_L$  is the lift force and  $C_l$  is the hydrodynamic coefficient of lift. The detailed study of the hydrodynamic force coefficients of the GRP covers is carried out in Chapter 2.

### 1.1.3 Reynolds number

One of the most important parameter for any flow field is Reynolds number. It is the ratio between inertial forces and viscous forces (Cengel & Cimbala, 2006).

$$Re_D = \frac{U_\infty D}{\nu} \quad (1.5)$$

where  $U_\infty$  is the free stream velocity,  $D$  is the characteristic length scale of the geometry and  $\nu$  is the kinematic viscosity of the fluid (Cengel & Cimbala, 2006). The characteristic length scale  $D$  is height of the GRP cover for all the cases in the present study.

## 1.2 On-bottom stability

Subsea installations are exposed to harsh ocean conditions. When a structure is installed in a particular subsea environment, it experiences a large number of external loads. The most common loads are hydrodynamic loads (lift and drag forces, rotational moment and buoyancy). Thus, it is a requirement in a design of the subsea structure that it must be able to withstand all of these loads and stay intact on its installed position. The term used for the stability of the structure in subsea environment is on-bottom stability. On-bottom stability of a structure is its ability to withstand all the possible environmental loads that are implied throughout its life.

All the loads that a structure experiences in a subsea environment can be resolved in two types of loads i.e. vertical loads and lateral loads. To ensure the on-bottom stability, vertical and lateral stabilities are analysed. In the present study, vertical and lateral stability is analysed and discussed in the Chapter 3.

### 1.2.1 Vertical stability

Vertical stability is the stability of structure against the vertical forces it experiences in the subsea environment. A structure submerged in water experiences buoyancy force in the vertically upwards direction and the weight of the body acting vertically downwards direction. To ensure the vertical stability, the weight of the body must be greater than the buoyancy force

it will experience (DNV-RP-F109, 2010). To keep the safety margin and accommodate the design uncertainties, a safety factor is also introduced. The check for vertical stability according to DNV-RP-F109 (2010) is as following:

$$\frac{\gamma_w}{s_g} \leq 1 \quad (1.6)$$

where,  $\gamma_w$  is the safety factor. Usually its value is taken as 1.1.  $s_g$  is the specific gravity of the subsea structure.

### 1.2.2 Lateral stability

Lateral stability is the stability of the structure against the lateral forces it experiences in subsea environment. A detailed study of following conditions is carried out to ensure lateral stability of the submerged structures according to DNV-RP-F109 (2010).

- **Current conditions:** Lateral stability analysis is carried out at the maximum possible current velocity for the selected return period. Current at GRP cover may have component from (DNV-RP-F109, 2010):
  - Wind induced current
  - Tidal current
  - Density driven current
  - Storm surge induced current
- **Short term waves conditions:** Sea wave behaviour of different seas all around the world is different and very complex. Each sea is defined by a specific statistical model. The waves may affect the on-bottom stability of structures as sometimes their effect can be felt on the seafloor. A proper statistical model and a return period depending upon the life span of the structure is chosen and effect of the waves on the on-bottom lateral stability is analysed.
- **Hydrodynamic loads:** Hydrodynamic load coefficients are calculated to compute hydrodynamic loads. For all types of GRP covers under consideration, lateral stability analysis is carried out based on these loads.

- **Load reduction possibilities:** There are many load reduction techniques applied by the industries for subsea structures. Some of the possibilities of load reduction are following according to DNV-RP-F109 (2010):
  - Load reduction due to trenching
  - Load reduction due to penetration
  - Load reduction due to pipe soil interaction
  - Load reduction due to permeable seabed
  
- **Seafloor resistance:** Soil resistance is a very important factor that contributes toward the lateral stability either positively or negatively. The Seafloor topography is very complex and vary from place to place. Therefore, the soil friction of the location of interest is first calculated experimentally and then included in the analysis. In general, there are four types of seafloors and experimental models are being developed to approximate seafloor resistance of all the four types (DNV-RP-F109, 2010)
  - Sand
  - Clay
  - Rock
  - Combination of above three

First, the seafloor chemistry is identified and then a proper model is applied to define the soils resistance for lateral stability analysis. The detailed study of on-bottom stability of the GRP covers is presented in Chapter 3.

### *1.3 Fishing activity loads*

North Sea has significant fishing activities along with the offshore oil & gas activities that have the possibility to cause damage to the pipeline. Several pipeline damage accidents caused by fishing activities have taken place in different parts of the world.

Trawling activity is of key importance to subsea pipelines and structures as fishing industries and offshore oil and gas are usually operating in the same regions. Subsea structures are key attraction to fish habitats. While fishermen are looking towards these fish habitats, the interaction between oil and gas and fishing industry is inevitable. Trenching of subsea pipelines minimizes the risk but it is not economically feasible in deep seas where fishing activities take place. Norwegian Petroleum Directorate (NPD) has given regulations that all the subsea installations on the Norwegian sector of the North Sea must be planned purposefully so that fishing activities remain unaffected. In general, fishing activities have the possibility to impose the following loads on the pipelines:

- a. Trawlboard impact: this is the impact load caused by the moving trawler on the pipeline
- b. Overpull: trawlboard attempts to overpull the pipeline by applying a moment along the centre of the pipeline.
- c. Friction: the movement of the trawl gear on the pipeline applies frictional load on the pipeline

GRP protection covers are used to protect the pipelines from these fishing activity loads. Therefore, GRP covers should be able to withstand these loads. The detailed study of the fishing activity loads on the GRP covers is presented in Chapter 4.

#### *1.4 Drop-object impact analysis*

Subsea pipelines and structures are vulnerable to the drop-objects from fishing activities, transportation barges, oil tankers and nearby platforms. The object dropped under the influence of gravity can cause severe damage to the subsea pipelines and structures. Therefore, a protection cover is necessary for subsea installations. Drop-objects apply impact loading to the subsea installations. The impact damage caused by the drop-objects is equal to the kinetic energy gained when undergoing freefall. When the drop-objects fall from their initial position, they accelerate until they achieve their terminal velocity. A drop-object has its maximum kinetic energy when it is moving with terminal velocity. The additional energy is dissipated in the form of heat and sound. When the drop-object strikes a subsea structure (in our case it is GRP cover) it delivers its impact energy to the structure. The structure absorbs the impact energy by undergoing deformation, heat and sound. The impact energy carried by various drop-objects and the absorption capacity of these impacts by the different GRP covers is of primary importance in studying drop object impact analysis. The detailed study of drop-objects on the GRP covers is presented in Chapter 5.

## *1.5 Objectives of this thesis*

The key objectives of the present study are:

- To calculate the hydrodynamic force coefficients of the three GRP covers (square, triangular and semi-circular) placed on the seabed using CFD simulations.
- To perform the on-bottom stability analysis of the three GRP cover geometries and compare with each other.
- To analyse the fishing activity loads on the three cover geometries and compare with each other.
- To calculate the drop-object impact energies of different offshore drop-objects and compare with the published results available in open literature.
- To calculate the drop-object impact-absorbing capacity of the three covers and compare with each other.

## *1.6 Outline of this thesis*

**Chapter 1:** Introduction

**Chapter 2:** Calculation of the hydrodynamic force coefficients of square, triangular and semi-circular GRP covers using CFD simulations

**Chapter 3:** On-bottom stability comparison of square, triangular and semi-circular GRP covers

**Chapter 4:** Fishing gear load bearing capacity comparison of square, triangular and semi-circular GRP covers using finite element method (FEM)

**Chapter 5:** Assessment of impact damage caused by drop-objects on square, triangular and semi-circular GRP covers using FEM.

**Chapter 6:** Conclusion, future research perspectives and references

(Intentionally left blank)

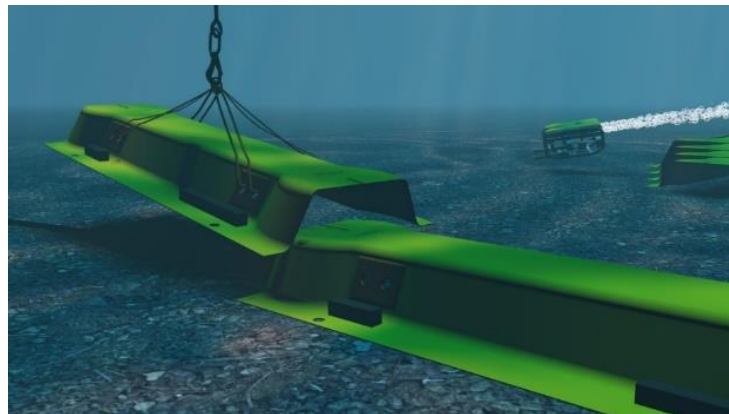


## Chapter 2

### Hydrodynamic force coefficients of GRP covers

#### 2.1 Introduction

The current induced and wave induced flows over the GRP cover are generally in the regimes of high Reynolds number ( $Re_D$ ) flow. The GRP covers are considered as bluff bodies. GRP covers under turbulent flow induce a complicated vortex system around themselves. The flow around GRP covers depends on  $Re_D$ , thickness of incoming boundary layer flow and the geometry of the structure. Analytical solutions for such hydrodynamic problems are not feasible. Therefore, numerical simulations or experiments are necessary to calculate the hydrodynamic forces on the GRP covers.



**Figure 2.1** Subsea GRP protection covers adapted from CSUB (2016)

CFD simulations is a good alternative to the experiments for obtaining the hydrodynamic forces due to the high expense of achieving high  $Re_D$  flows in laboratory testing. Recent advances in computing power have made CFD simulations being widely used in the industry and research purposes.

Reynolds-Averaged Navier-Stokes (RANS) modelling is still a preferred method compared to the Large Eddy Simulation (LES) or Direct Numerical Simulation (DNS) in the industry. This

is due to the low computational cost of RANS with reasonable engineering accuracy as compared to LES and DNS. In the present study, effects of boundary layer flow over three GRP covers are studied and the corresponding hydrodynamic force coefficients are calculated. RANS approach is applied to solve the flow field. A validation study of the boundary layer flow over structures is carried out by comparing the results with the published experimental data.

The hydrodynamic force coefficients calculated in this section are further used in Chapter 3 to perform on-bottom stability of the GRP covers.

### 2.1.1 Literature review

To the best of our knowledge, there is no publication on the boundary layer flow around square, triangular and semi-circular covers on the seabed at the  $Re_D = 1 \times 10^6$ . However, publications have been done for the flow inside a channel on the rib structures (long structures that can be approximated as a 2D geometry). The relevant publications are mentioned below:

Fujimoto et al. (1975) presented the pressure distribution around two-dimensional square structures subject to turbulent boundary layer flow with the various values of free stream velocity  $U_\infty$  and non-dimensional boundary layer thickness  $\delta/D$  (where  $\delta$  is the boundary layer thickness of the incoming flow and  $D$  is the height of the square structure). The measurements were performed inside a wind tunnel. The values of the  $Re_D$  range from  $3.41 \times 10^4$  to  $1.19 \times 10^5$ . In the wind tunnel experiments, long surface mounted structures were subjected to flow normal to the length. Their results showed that by increasing  $\delta/D$ ,  $C_D$  decreases.

Good & Joubert (1968) conducted the experiments on 2D vertical plates called fence in a wind tunnel. They reported that for  $\delta/D \geq 1.2$ ,  $C_D$  varies logarithmically with respect to  $\delta/D$  for high  $Re_D$  boundary layer flow.

Keshmiri (2012) performed a numerical sensitivity analysis of the 2D and 3D square cross-sections of structures in channel flow. RANS simulation with the  $k-\epsilon$  turbulence model was performed at the Reynolds number defined based on hydraulic diameter of the channel  $Re_{Dh} = 3.0 \times 10^4$ . The pressure distribution results for the 3D channel were in a good agreement with the equivalent experimental data and they showed that a 2D channel could be used to represent the centre line of 3D channel with satisfactory accuracy.

### 2.1.2 Overview of the study in this Chapter

Square, triangular and semi-circular geometries of GRP covers are considered for design optimization in this thesis. Thus, the hydrodynamic force coefficients of these three covers are necessary for computing the required forces. Hydrodynamic force coefficients of the GRP covers are calculated by performing CFD simulations. These coefficients are necessary to compute on-bottom stability of the GRP covers. The required data are not available in the open literature hence, the hydrodynamic force coefficients of the GRP covers are calculated in the present study.

$Re_D$  based on the cover height  $D$  ranged from  $1.19 \times 10^5 < Re_D < 1.00 \times 10^6$  for all simulations.  $C_D$  and  $C_L$  are required for on-bottom stability study of the GRP covers at a  $Re_D = 1.00 \times 10^6$ . No experimental or numerical published data of hydrodynamic force coefficients are available at this  $Re_D$ . Published experimental results of  $C_D$  were available at a  $Re_D = 1.19 \times 10^5$  for the square cover by Fujimoto et al. (1975). The numerical simulation setup used in the present study is validated by comparing the results with Fujimoto et al. (1975) at  $Re_D = 1.19 \times 10^5$ . The same numerical setup is further used to calculate the required hydrodynamic force coefficients at  $Re_D = 1.00 \times 10^6$  of all the three covers.

2D simulations are performed since the length of the GRP cover is considered significantly large as compared to the cross-section dimensions. The cover is considered normal to the flow direction.  $C_D$  and  $C_L$  were calculated for the three geometries by varying boundary layer thicknesses. Recirculation length is the distance between fluid separation point and the reattachment point as shown in the Figure 2.2.

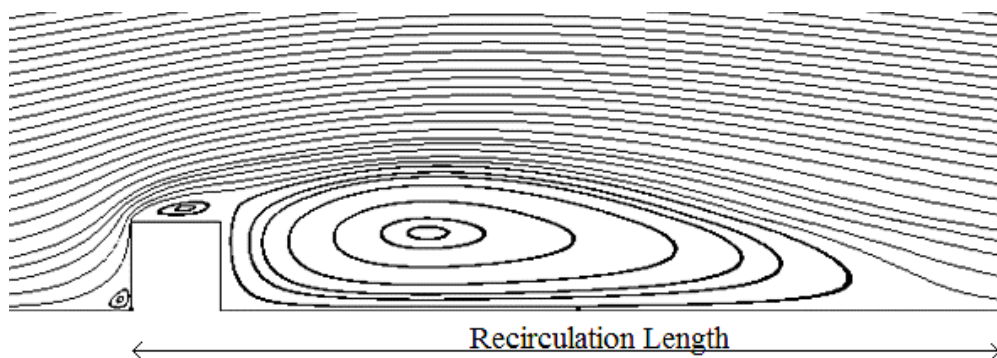
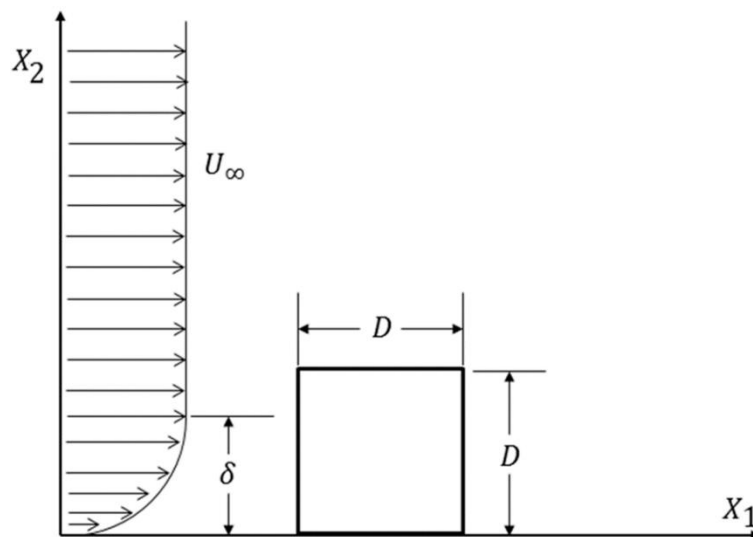


Figure 2.2 A typical flow around GRP cover taken from the present simulations

In the present study, 2D RANS equations with the standard  $k-\varepsilon$  turbulence model are adopted. The open source code OpenFOAM is used for all the numerical simulations, in combination with GMSH for mesh generation and ParaView and TecPlot360 for post-processing. Grid convergence studies are carried out for all the cases.

### 2.1.3 Nomenclature

Figure 2.3 shows a schematic illustration of a boundary layer flow over square GRP cover placed on the seabed. The coordinate system used in the present study is  $X_1$  and  $X_2$ . Horizontal coordinate is  $X_1$  and the vertical coordinate is  $X_2$  as shown in the Figure 2.3 below:



**Figure 2.3 Schematic illustration of a boundary layer flow over square GRP cover placed on the seabed**

The origin of the coordinate system  $(0, 0)$  is upstream on the seabed (bottom wall). The height of the GRP cover is  $D$  along  $X_2$ , the width is  $D$  along  $X_1$  and the length is normal to the  $X_1$ -  $X_2$  plane.

The velocity outside the boundary layer is  $U_\infty$  in the  $X_1$  direction. The free stream velocity is far from the cover where the changes along  $X_2$  are negligible and the presence of the cover does not influence the velocity. The boundary layer thickness  $\delta$  is the normal distance from the horizontal plane wall to where the velocity becomes equal to  $U_\infty$  (Cengel & Cimbala, 2006). Similar definitions can be seen for triangular GRP cover in Figure 2.4 and semi-circular GRP cover in Figure 2.5.

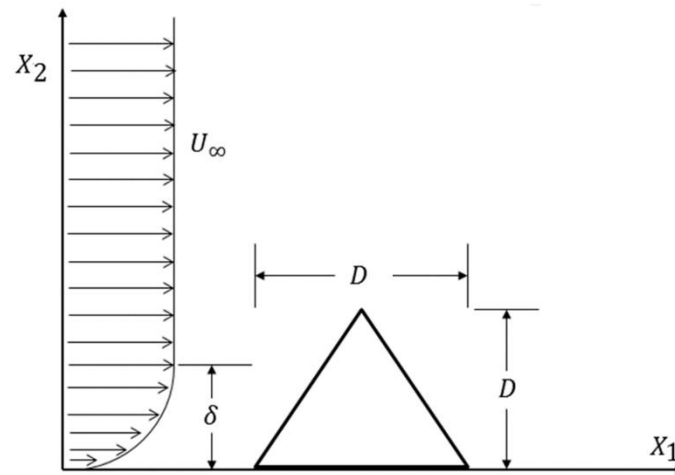


Figure 2.4 Schematic illustration of boundary layer flow over triangular GRP cover placed on the seabed

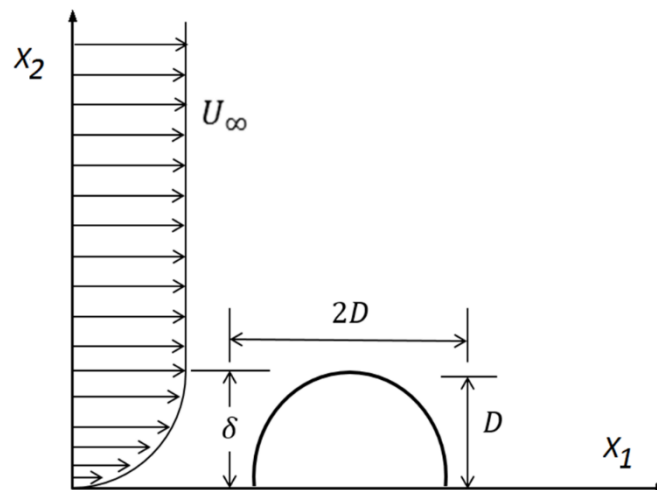


Figure 2.5 Schematic illustration of boundary layer flow over semi-circular GRP cover placed on the seabed

## 2.2 Basic theory of fluid flow

### 2.2.1 Flow physics

The flow around an aerofoil, plate or a cylinder suspended in fluid flow is different from the flow around GRP covers on the seabed. This is because a bluff body suspended in the fluid is subject to vortex shedding. Vortex shedding takes place for symmetrical flows when the flow is from both upper and lower side of the geometry as shown in Figure 2.6. Contrarily, a GRP cover attached on the seabed has flow from the upper side of the geometry only. Thus, instead

of vortex shedding, a large wake is formed downstream of the GRP cover. The large wake behind the GRP cover has a negligible variation with the time. Therefore, it is expected that a steady state solution can predict the flow field with high accuracy.

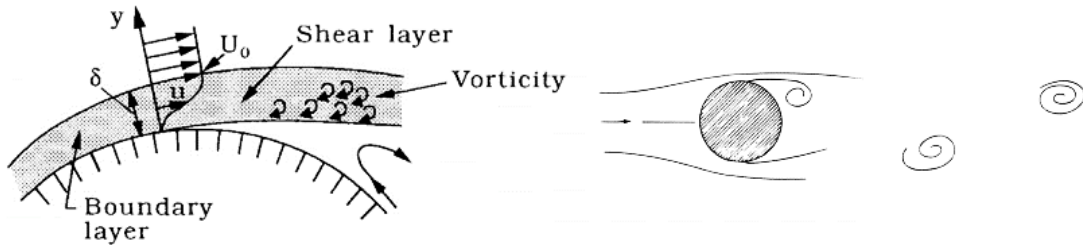


Figure 2.6 Vortex shedding taken from Sumer & Fredsøe (1997)

The flow characteristics of boundary layer flow over a GRP cover placed on the seabed are dependent on multiple parameters such as non-dimensional boundary layer thickness  $\delta/D$ , free stream turbulence intensity, profile of the boundary layer and the shape of GRP cover according to Adams & Johnston (1988).

Reynolds number based on the kinematic viscosity is defined in the Equation 1.5. It can also be defined with respect to fluid dynamic viscosity ( $\mu$ ) and the density ( $\rho$ ).

$$Re_D = \frac{\rho U_\infty D}{\mu} \quad (2.1)$$

The investigation range in the present study is  $1.19 \times 10^5 < Re_D < 1.00 \times 10^6$  which is considered high  $Re_D$  flow. The flow over square and triangular geometry covers is fully developed turbulent flow in this range of  $Re_D$  but for semi-circular geometry cover, the flow is in super critical flow regime according to Adams & Johnston (1988) and Cengel & Cimbala (2010). The fluid flow is incompressible in the present study. Incompressible flow regime is valid for Mach number  $Ma \leq 0.3$  where Mach number is the ratio between speed of flow and the speed of sound.

## 2.2.2 Turbulence modelling

The flow field is defined either as laminar or turbulent. Low values of  $Re_D$  refer to laminar flow while the high values of  $Re_D$  refer to turbulent flow. Laminar flow is streamlined while the turbulent flow is chaotic flow as shown in the Figure 2.7.

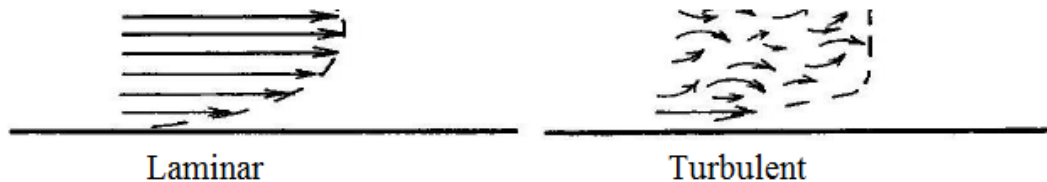


Figure 2.7 Laminar and turbulent flow taken from Versteeg & Malalasekera (2007)

The fluid flow is laminar below the critical  $Re_D$ . However, above the critical  $Re_D$ , the flow becomes turbulent. The value of critical Reynolds number changes depending upon the flow conditions and geometry of bluff body. Fully developed turbulent flow is considered in all the present simulations. The turbulent flow has small horizontal velocity fluctuations  $u'(t)$  around mean velocity  $U$  are shown in the Figure 2.8.

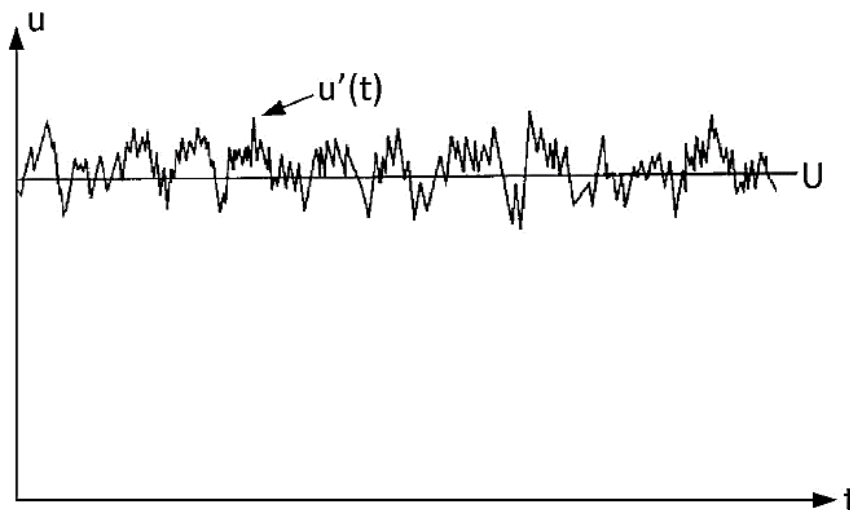


Figure 2.8 Turbulent instantaneous velocity variation with respect to time taken from Versteeg & Malalasekera (2007)

The horizontal velocity  $u(t)$  at a particular instance of time  $t$  can be expressed as following:

$$u(t) = u'(t) + u \quad (2.2)$$

In order to get a steady state solution, RANS equations are solved. In RANS, the velocity  $u$  and pressure  $p$  are expressed by their time-averaged values in turbulent flow. They always have a 3D spatial character even when the flow field is 2D. However, in the present study 3D component is negligibly small as compared to the other dimensions because the flow is along the cross-section of the GRP covers. The length of the cover is considered significantly larger as compared to the cross-sectional dimensions. This assumption is in accordance with Keshmiri (2012).

In the turbulent flow, turbulent eddies are in a wide range of length scales. The larger eddies have a characteristic length scale of the order of the effective length of the cross-section of the structure (which in our case is the height of the covers  $D$ ). The effective velocity of eddies is in order of  $U_\infty$ . The viscous effects in these eddies are negligible because they are dominated by the inertia effect. The smaller eddies have the tendency to follow the motion of the larger eddies. The kinetic energy is dissipated from large eddies to the subsequent smaller eddies according to the principle called energy cascade (Versteeg & Malalasekera, 2007). The energy cascade is shown in Figure 2.9.

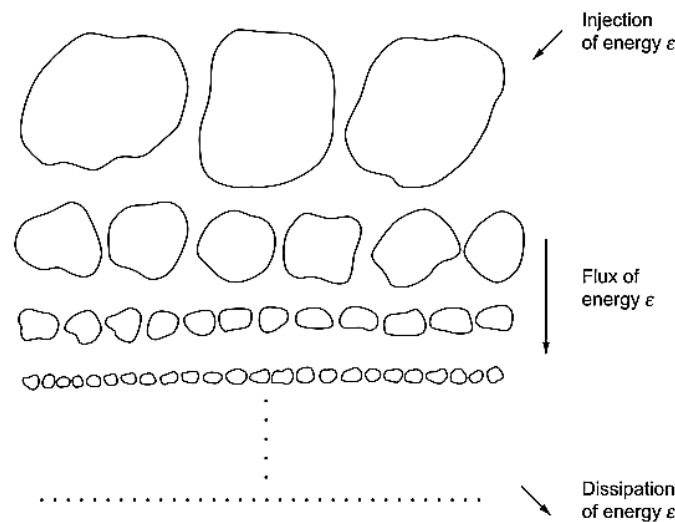


Figure 2.9 Energy cascade taken from Ecke (2005)

### 2.2.3 Turbulent boundary layer flow

In high  $Re_D$  flow the fluid begins with a laminar region and permutes into the turbulent flow. As the flow develops, it achieves a specific profile called log profile. It can be seen in the Figure 2.10, that the fluid flow on a flat plate starts laminar and turns into turbulent flow having eddies and circulations. The boundary layer is developed on the principle of no-slip condition. The



fluid layer adjacent to the plate is at zero velocity and increases to the free stream velocity in the  $X_2$  direction.

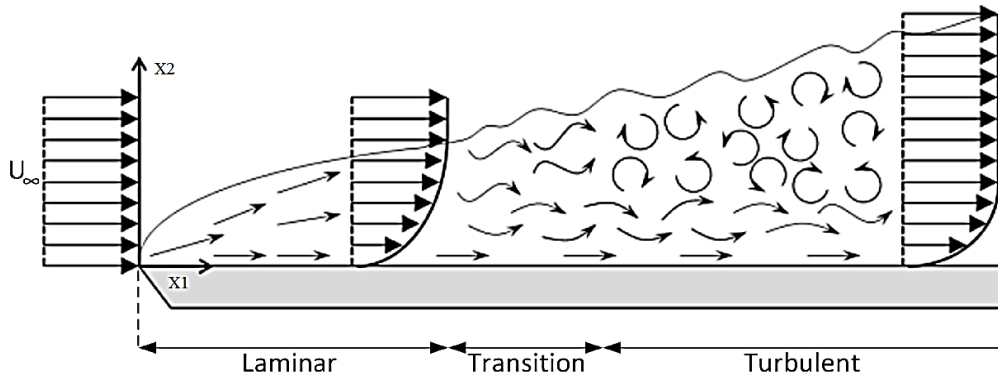


Figure 2.10 Boundary layer flow over a flat plate taken from Frei (2013)

Versteeg & Malalasekera (2007) has conducted analysis and measurements on the development of the boundary layer thickness. The turbulent boundary layer consists of different layers and each of the layer has its own properties. The properties of the different layers can be expressed by two non-dimensional parameters  $u^+$  and  $y^+$ . Where  $u^+$  is the non-dimensional velocity, which is the ratio of velocity and shear velocity while  $y^+$  is the non-dimensional vertical distance from the bottom wall.

$$u^+ = \frac{u}{u_t} \quad (2.3)$$

$$y^+ = \frac{yu_t}{\nu} \quad (2.4)$$

where  $u_t$  is the shear velocity, and  $y$  is the vertical distance varying normally from the wall. The layer nearest to the wall is called as viscous sublayer. In this layer viscous stresses dominates. It is also referred to as the laminar sublayer. The velocity profile follows a linear relationship in this layer. The viscous sublayer has a small thickness. The typical values are of the order of 1.0% of the boundary layer thickness or holds  $y^+ \leq 5$ . The velocity gradient in the viscous sublayer remains nearly constant and the flow velocity only depends on  $y^+$  within the layer.  $u^+$  follows a linear relationship with  $y^+$  within the viscous sublayer on a smooth wall as following:

$$u^+ = y^+ \quad (2.5)$$

Next to the viscous sublayer is the buffer layer. In this layer, the viscous as well as turbulent stresses are of key consideration. After viscous sublayer is the log-law layer (also called law of wall). In this layer the turbulent stresses dominate. The log-law layer has a region bound of  $30 < y^+ < 500$ . Where the shear stress changes gradually from the wall according to Versteeg & Malalasekera (2007). An expression for the non-dimensional velocity for smooth walls within this layer is as following:

$$u^+ = \frac{1}{k} \ln(Ey^+) \quad (2.6)$$

where  $k$  is the constant having value  $0.41$  and  $E$  is the log-law constant having value  $9.8$  in OpenFOAM for smooth walls. The Equation 2.6 is called as log-law. The different layers of the boundary layer flow discussed are shown in Figure 2.11.

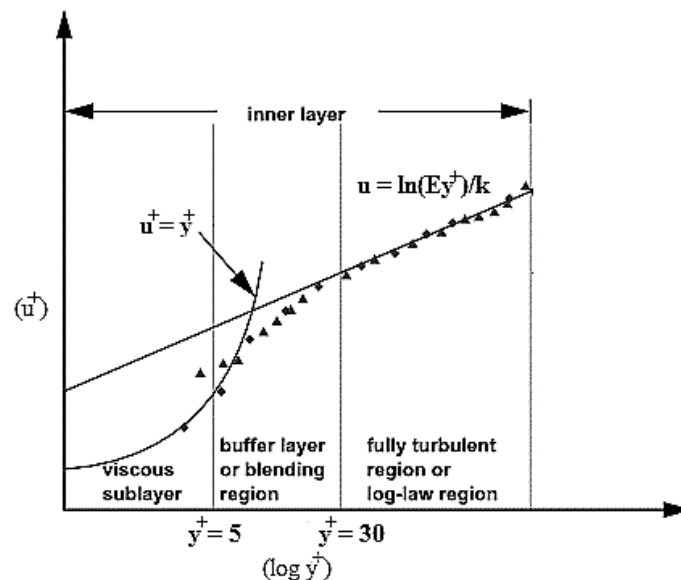


Figure 2.11 Boundary layer regions modified from Versteeg & Malalasekera (2007)

#### 2.2.4 Mass and momentum conservation

For any incompressible and isothermal fluid flow, the governing equations are continuity equation and momentum equation, which are also known as Navier-Stokes equations.

The mass remains constant with respect to time according to the continuity equation. In a close system, the mass can neither be created nor destroyed. According to Navier-Stokes equations, the surface and body forces balance the inertial forces acting on the fluid element (Cengel &

Cimbala, 2006). The Navier-Stokes equations for the conservation of mass and momentum can be expressed as tensors:

$$\frac{\partial u_i}{\partial x_i} = 0 \quad (2.7)$$

$$\frac{\partial u_i}{\partial t} + u_j \frac{\partial u_i}{\partial x_j} = -\frac{1}{\rho} \frac{\partial p}{\partial x_i} + \nu \frac{\partial^2 u_i}{\partial x_j^2} \quad (2.8)$$

where  $i, j = 1, 2$ ,  $u_i$  and  $u_j$  are the Cartesian velocity components,  $t$  is the time, and  $x_i$  and  $x_j$  are Cartesian direction components.

The influence of gravitational forces is negligible on the present fluid flow problem therefore; it is not included in the equations above.

### 2.2.5 Turbulence model

Turbulence is defined as fluctuations, both in space and time of velocity and pressure. The turbulent regime can be studied resolving all the flow details by Direct Numerical Simulations (DNS). The mesh used for DNS are sufficiently fine in order to resolve the smallest eddies where energy is dissipated which results in high computational costs. Thus, DNS is not used for industrial applications (Versteeg & Malalasekera, 2007).

Large Eddy Simulation (LES) models the small eddies in the flow but resolves the larger eddies. Unsteady Navier-Stokes equations are filtered for these large eddies before the computations start. LES is less computationally expensive than DNS but more expensive than RANS method.

RANS equations use average values of small fluctuating velocities to reduce the computational cost by taking a time average of the Navier-Stokes equations. The RANS equations are solved based on conservation of mass and momentum. The relations are given below:

$$\frac{\partial u_i}{\partial x_i} = 0 \quad (2.9)$$

$$\frac{\partial u_i}{\partial t} + u_j \frac{\partial u_i}{\partial x_j} = -\frac{1}{\rho} \frac{\partial p}{\partial x_i} + \nu \frac{\partial^2 u_i}{\partial x_j^2} - \overline{\frac{\partial u'_i u'_j}{\partial x_j}} \quad (2.10)$$

The expression of  $\overline{\frac{\partial u'_i u'_j}{\partial x_j}}$  is:

$$\overline{\frac{\partial u'_i u'_j}{\partial x_j}} = \nu_t \left( \frac{\partial u_i}{\partial x_j} + \frac{\partial u_j}{\partial x_i} \right) - \frac{2}{3\rho} k \delta_{ij} \quad (2.11)$$

where  $\delta_{ij}$  is Kronecker delta and the kinematic turbulence viscosity  $\nu_t$  is as following:

$$\nu_t = C_\mu \frac{k^2}{\varepsilon} \quad (2.12)$$

$$\mu_t = \nu_t \rho \quad (2.13)$$

where  $\mu_t$  is the dynamic turbulent viscosity. The k- $\varepsilon$  turbulence gives two equations for k and  $\varepsilon$  as following:

$$\frac{\partial k}{\partial t} + u_j \frac{\partial k}{\partial x_j} = \frac{\partial}{\partial x_j} \left( \frac{\nu_t}{\sigma_k} \frac{\partial k}{\partial x_j} \right) + \nu_t \left( \frac{\partial u_i}{\partial x_j} + \frac{\partial u_j}{\partial x_i} \right) \frac{\partial u_i}{\partial x_j} - \varepsilon \quad (2.14)$$

$$\frac{\partial \varepsilon}{\partial t} + u_j \frac{\partial \varepsilon}{\partial x_j} = \frac{\partial}{\partial x_j} \left( \frac{\nu_t}{\sigma_k} \frac{\partial \varepsilon}{\partial x_j} \right) + C_1 \frac{\varepsilon}{k} \nu_t \left( \frac{\partial u_i}{\partial x_j} + \frac{\partial u_j}{\partial x_i} \right) \frac{\partial u_i}{\partial x_j} - C_2 \frac{\varepsilon^2}{k} \quad (2.15)$$

where the coefficients are:  $C_1 = 1.44$ ,  $C_2 = 1.92$ ,  $C_\mu = 0.009$ ,  $\sigma_k = 1.0$  and  $\sigma_\varepsilon = 1.3$  (Launder & Spalding, 1974).

### 2.2.6 Lift and drag forces acting on the body

The problem taken in the present study consists of a cross-section of a 2D square, triangular and semi-circular cover immersed in a turbulent boundary layer. As the fluid moves over the solid body, shear forces are exerted parallel to the surface of the body and pressure forces act normal to the surface. The relations for drag and lift forces are given in Equations 1.1 & 1.2.

The shape of the body determines the velocity field and the forces upon it. Broadly, the bodies may be classified as being streamlined or bluff. In the case of a streamlined body, the fluid flow is aligned to the body and do not get chaotic. Examples of such bodies are aerofoils and submarines. A bluff body is characterized by blocking the fluid and the flow separates from the body instead of following its shape. Examples of bluff bodies are pipes, houses and buildings. Drag forces in the streamlined bodies are less in comparison to bluff bodies when subjected to incoming fluid flow. For the total drag of a bluff body, the shear force component is small

compared to the pressure component. Contrarily, for the total drag on streamlined bodies the shear force component is more significant. In the present study all the GRP covers are considered bluff bodies; hence, the pressure component is dominant.

Force coefficients are one way of expressing the total drag force and lift force. This method is intuitive since the coefficients can be applied to find the force for various dimensions of a structure with the same geometry subjected to similar flow conditions. The drag and lift coefficients are  $C_D$  and  $C_L$ , respectively. The expressions for  $C_D$  and lift coefficient  $C_L$  are given in Equation 1.3 & 1.4.

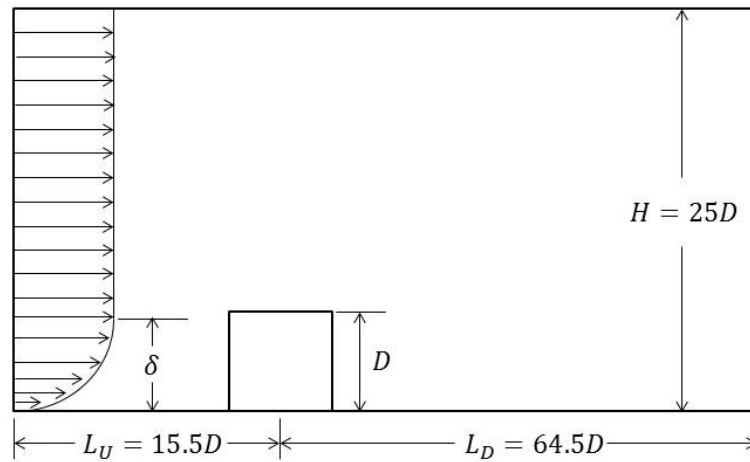
### 2.3 Mesh and boundary conditions

This section is about the numerical set-up incorporated in the present study. For all the simulations, same computational domain height and width is used.

#### 2.3.1 Domain

For every CFD problem, a computational domain is defined and the size of the computational domain is very important for the accuracy and computational costs for fluid flow problems. If the computational domain is made too small, it may influence the results especially the hydrodynamic quantities  $C_D$  and  $C_L$  on the structures. While if the domain is too large then unnecessary computational costs may result owing to the additional cells in the computational domain. For the optimal choice of a computational domain, a domain size that is tested on similar flow problems must be used, otherwise, a domain size convergence test must be performed. A domain size convergence test is a test in which various domain size parameters are changed to examine how much it affects the overall results of the problem. Some of the examples of such parameters are the distance from the inlet to the studied object  $L_U$ , the height of domain  $H$  and the distance from the studied object to the outlet  $L_D$  as shown in Figure 2.12.

Figures 2.12, 2.13 & 2.14 show the computational domains used for the square, triangular and semi-circular cross-sections, respectively. The unit of length shown for the domain size is  $D$  due to the decision of using a constant value of GRP cover height  $D$ . for all dimensioning purposes.



**Figure 2.12 Computational domain of square GRP cover**

Ong et al. (2010) carried out the numerical study of flow around circular cylinder close to a flat seabed at high  $Re_D$ , which is approximately similar to the present case. They presented physically sound numerical results; therefore, a similar approach can be used for the present study. Ong et al. (2010) used a domain that had  $L_U$  of  $10D$ . According to Ong et al. (2010) this distance is sufficiently long to avoid far-field effects on the upstream flow of the cylinder. Hence, it is presumed that in order to neglect far-field effects in the present study,  $L_U$  needs to be equal or longer than this value.  $L_U$  in the present study is set to be  $15.5D$  to ensure conservativeness.

$L_D$  is set to be  $64.5D$ . This is sufficient according to the numerical simulations reported by Ong et al. (2010) where it is reported that  $L_D = 20D$  can eliminate the far field effects on the structure.

Simulations conducted by Ong et al. (2010) reported that  $H$  may vary from  $8.5D$  to  $9.4D$  without having an effect on the flow around the cylinder and the flat seabed. The  $H$  is set to be  $25D$  in order to ensure conservativeness. In the wind tunnel experimental data reported by Fujimoto et al. (1975),  $H = 17D$  for similar flow conditions is used. For  $H$  a convergence study is also performed in Section 2.4.1 to validate  $H$ .

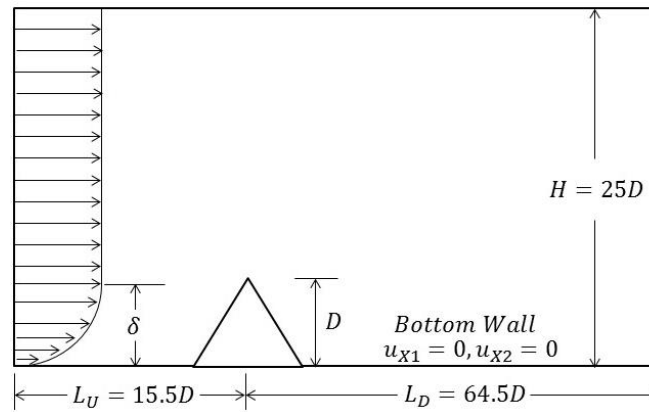


Figure 2.13 Computational domain of triangular GRP cover

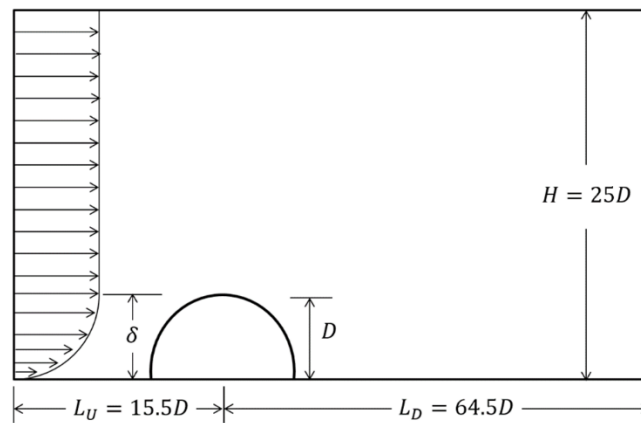


Figure 2.14 Computational domain of semi-circular GRP cover

### 2.3.2 Mesh set-up

A structured mesh in multiple blocks is the mesh set-up being used in the present study. It simplifies for the user to define mesh properties in each block. Creating a high-quality mesh is essential for reliable and consistent results.

Each cell has four measures of mesh quality that are; skewness, orthogonality, changes in size between neighbouring cells and aspect ratio. Deviation of the inner angle of the elements from  $90^\circ$  is the basis for the skewness for the quadrilateral element. While the basis for the orthogonality is that how close to some optimal angle are the angles between adjacent element edges, or adjacent element faces. For the quadrilateral element, this optimal angle is  $90^\circ$ . The change in the element size between the neighbouring sizes has to be smooth and generally taken to be less than a ratio of 1.2. The ratio obtained by dividing the length of the elements longest edge by the shortest edge is the aspect ratio.

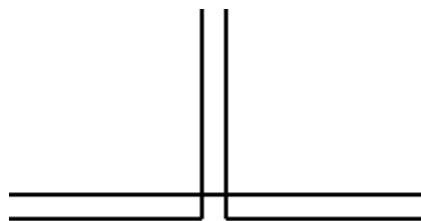
The ideal ratio for a quadrilateral element should be one, however OpenFOAM can handle reasonably larger aspect ratios. In this research study, for all the final mesh configurations used, the largest aspect ratio for any cell is kept lower than 50 for all the mesh. Table 2.1 illustrates mesh quality in terms of skewness. The spectrum ranging from 0 to 1.0 is taken to define the skewness going from value 0 which is ‘zero skewed cells’ to 1.0 which is critically skewed cells. There is usually a correlation between quality of elements in terms of skewness and orthogonal quality.

**Table 2.1 Skewness mesh metrics spectrum taken from Bakker (2006)**

<b>Excellent</b>	<b>Good</b>	<b>Acceptable</b>	<b>Poor</b>	<b>Sliver</b>	<b>Degenerate</b>
0-0.25	0.25-0.50	0.50-0.80	0.80-0.95	0.95-0.99	0.99-1.0

Skewness should not exceed 0.85 for quadrilateral and hexahedral elements. To ensure that the mesh in the present study is of excellent quality, the skewness is kept below 0.25 for all numerical simulations. This is defined as excellent quality in terms of skewness from Table 2.1.

In the present study, the software used for making the mesh is GMSH. A bottom-up mesh is applied in which the vertices, are first created and then connected with edges. Figures 2.15, 2.16 & 2.17 describe a block-topology used for square, triangular and semi-circular geometries. Block lines control the mesh entities like number of elements, progression and spacing. To optimize the analysis work, the cell count is to be kept low while keeping the same amount of precision. For this purpose, a fine mesh of good quality is applied at the areas of concern such as around the cross-section of the GRP cover. The progression of mesh close to the GRP cover and seabed allows good control to keep the non-dimensional number average  $y^+$  between 30 and 45. In the square cover, all the cells have zero skewness and ensure perfect orthogonal quality.



**Figure 2.15 Block topology of square geometry cover**



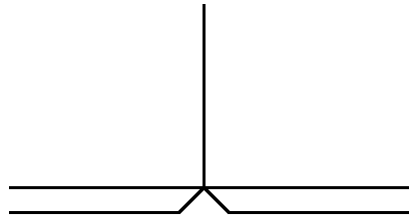


Figure 2.16 Block topology of triangular geometry cover

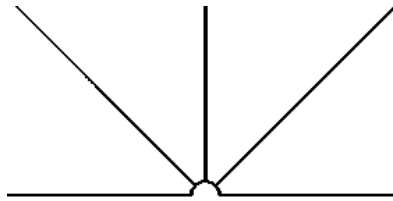


Figure 2.17 Block topology of semi-circular geometry cover

Instead of resolving the boundary layer, boundary layer flow is modelled by using the law of wall as described in Section 2.2.3. This is a more efficient way as fewer cells leads to less computational cost than fully resolving the boundary layer. The height of the first cell from the wall  $h_p$  becomes a relevant parameter if the law of wall is applied. Figure 2.18 illustrates the definition of  $h_p$  and shows the gradual growth rate after first cell.

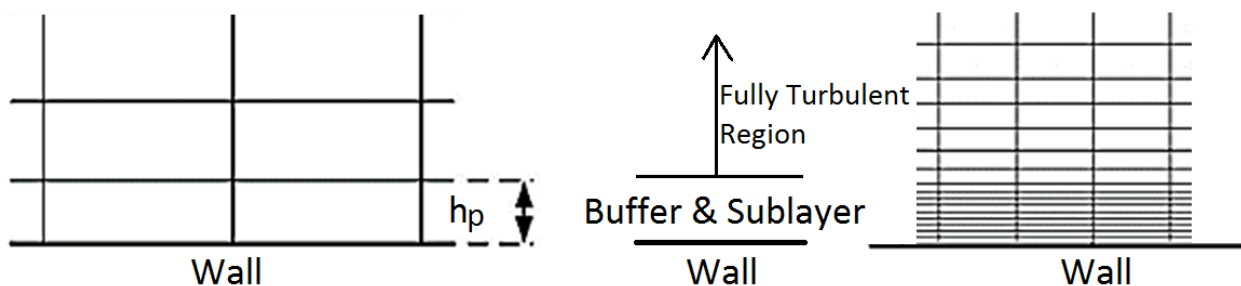
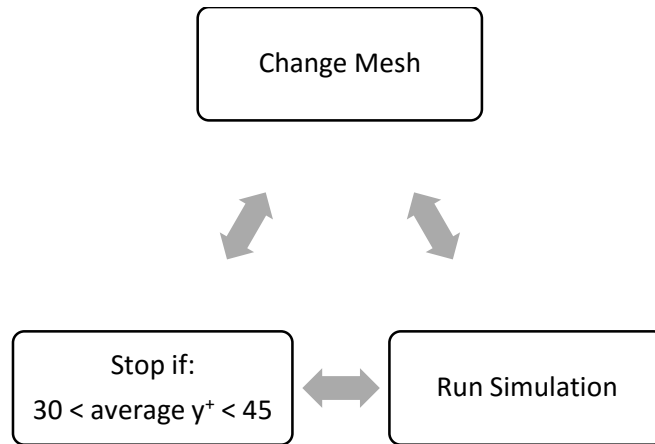


Figure 2.18 Law of wall approach and first node height

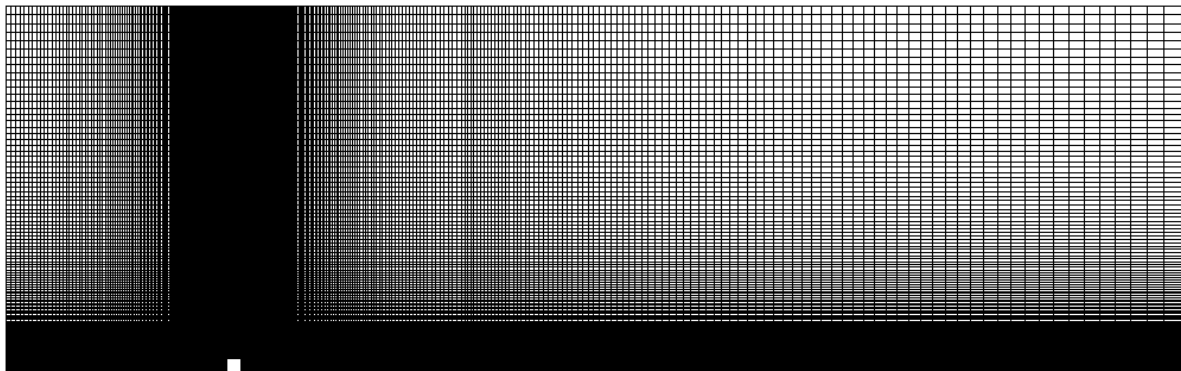
For  $y^+ < 10$ , the high  $Re_D$  RANS models give incorrect results according to Code-Saturne (2014). The first node height is kept greater than 30 in all the simulations. This is done iteratively according to the following algorithm:



**Figure 2.19 Average  $y^+$  convergence algorithm**

The recommended value of  $y^+$  for RANS code with  $k-\varepsilon$  model is close to 30 (Code-Saturne, 2014). Therefore, in the present study, the first node of numerical simulation is set to be close to this recommended value.

In order to resolve the boundary layer along the flat bottom surface, layers of square elements parallel to the flow direction are applied. Figure 2.20 illustrate the global mesh of the square GRP cover at  $\delta/D = 0.73$  and for  $Re_D = 1.19 \times 10^5$ . In the Figure 2.21, local mesh of the same case is shown. It can be observed that the mesh becomes finer closer to the GRP cover and gradually becomes coarser further away from the cover towards the boundaries of the computational domain. The mesh of triangular and semi-circular covers are shown in Figures 2.22 to 2.25 at  $\delta/D = 1.70$  and  $Re_D = 1.00 \times 10^6$  where a similar meshing scheme is adopted as discussed for the square cross-section.



**Figure 2.20 Global mesh of square geometry cover for  $\delta/D = 0.73$  and  $Re_D = 1.19 \times 10^5$**

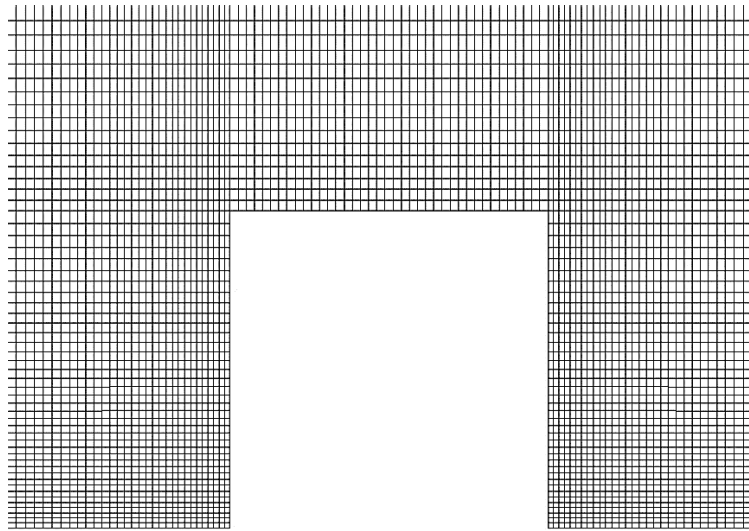


Figure 2.21 Local mesh of square geometry cover for  $\delta/D = 0.73$  and  $Re_D = 1.19 \times 10^5$

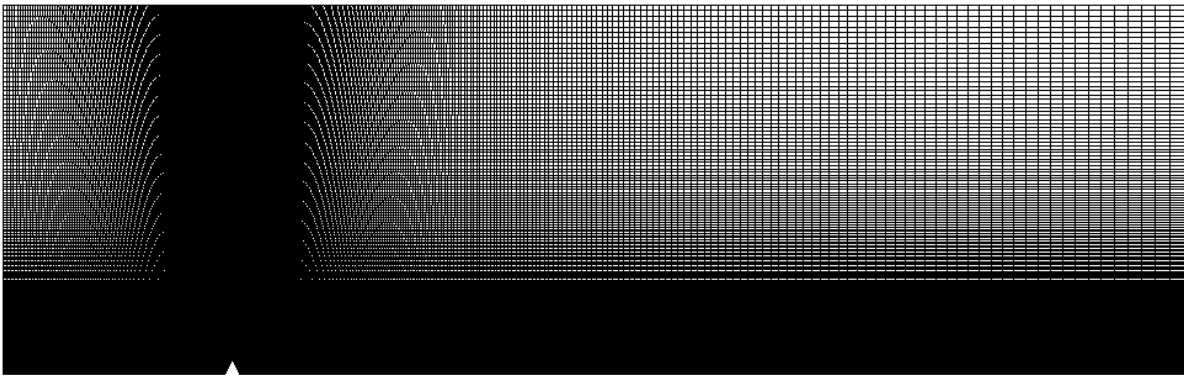


Figure 2.22 Global mesh of triangular geometry cover for  $\delta/D = 0.73$  and  $Re_D = 1.00 \times 10^6$

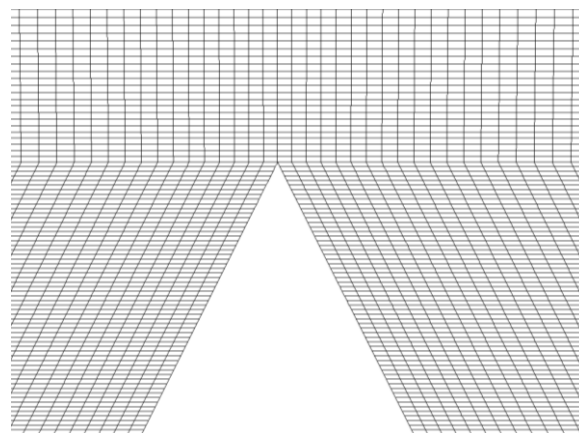


Figure 2.23 Local mesh of triangular geometry cover for  $\delta/D = 0.73$  and  $Re_D = 1.00 \times 10^6$

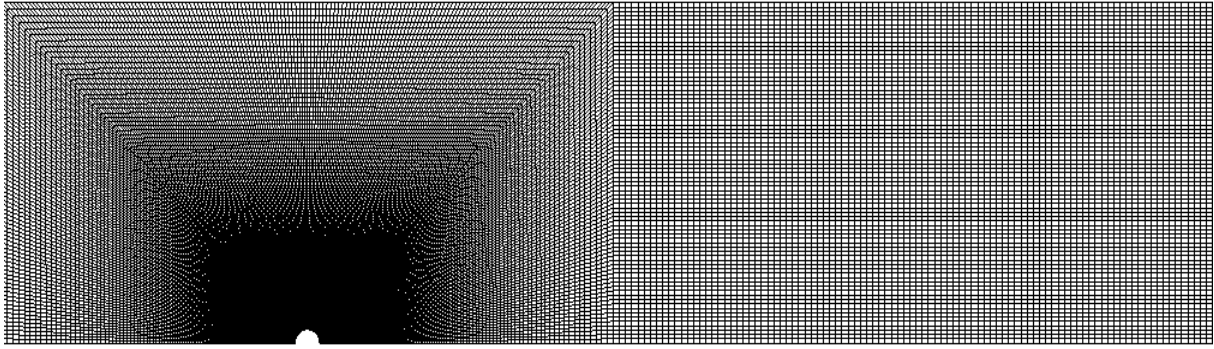


Figure 2.24 Global mesh of semi-circular geometry cover for  $\delta/D = 0.73$  and  $Re_D = 1.00 \times 10^6$

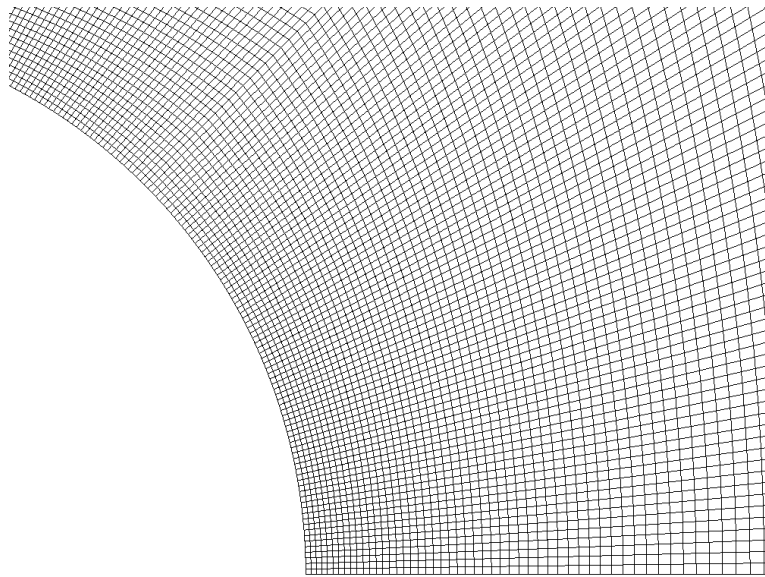


Figure 2.25 Local mesh of semi-circular geometry cover for  $\delta/D = 0.73$  and  $Re_D = 1.00 \times 10^6$

### 2.3.3 Boundary Conditions

In all CFD problems, the initial and boundary conditions are specified and they play a vital role in modelling the flow physics correctly. These includes the inlet, wall and the symmetry boundary conditions. An overview of these boundary conditions are illustrated in Figures 2.26, 2.27 & 2.28 for the three geometries being studied. The boundary conditions used on the covers are same as bottom wall.

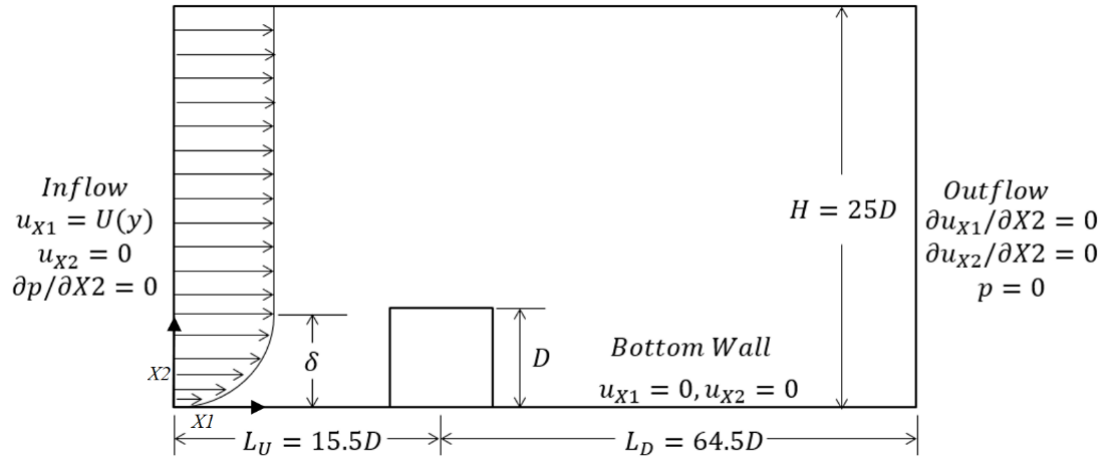


Figure 2.26 Boundary conditions, square GRP cover

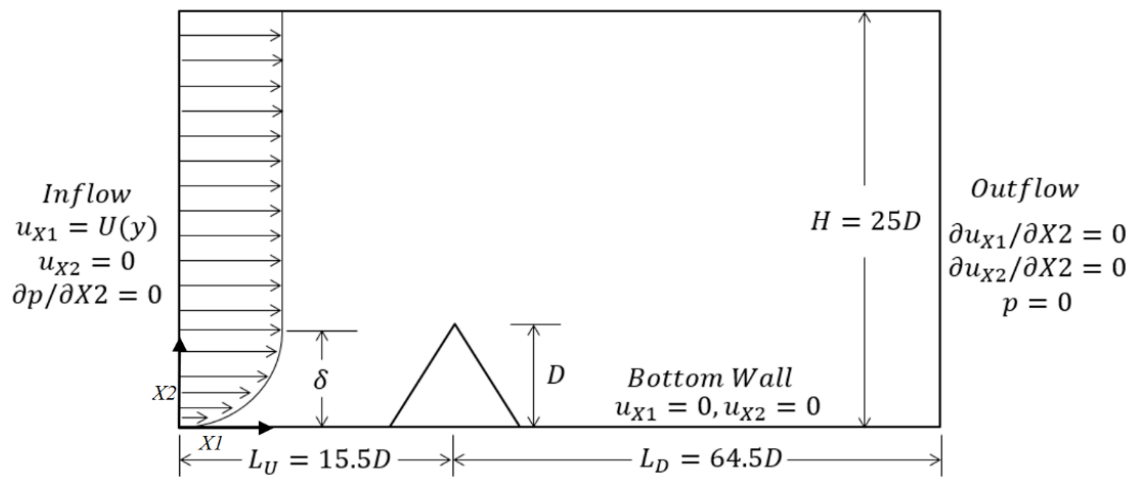


Figure 2.27 Boundary conditions, triangular GRP cover

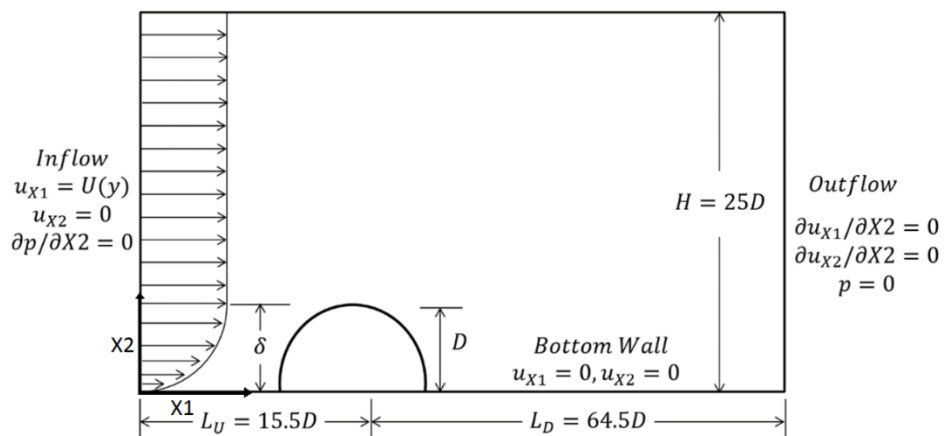


Figure 2.28 Boundary conditions, semi-circular GRP cover

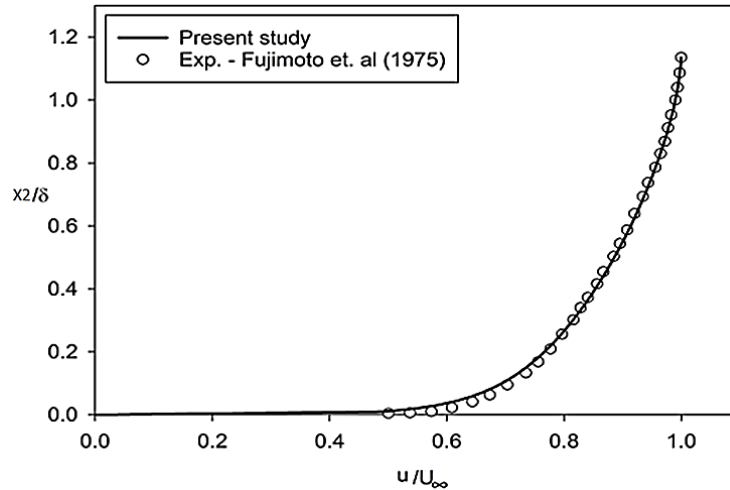
The inlet velocity is a log profile for the boundary layer. The value of the vertical velocity at this location is set to be zero. The velocity profile is adapted by curve fitting of the experimental boundary layer profile provided by Fujimoto et al. (1975). This is done to ensure similarity between the present numerical setup and Fujimoto et al. (1975) experimental setup in order to compare results. The same velocity profile is further used for all other simulations. At the inlet, the value of  $k$  and  $\varepsilon$  can be expressed as functions of  $X_2$  (Ong et al., 2010). Where  $X_2$  is the instantaneous height in the vertical direction as defined in the Section 2.1.3. The expressions are following:

$$K(X_2) = \max \left\{ C_\mu^{-\frac{1}{2}} \left( 1 - \frac{X_2}{\delta} \right) \left| 1 - \frac{X_2}{\delta} \right| \mu_t^2, 0.00001 U_\infty^2 \right\} \quad (2.16)$$

$$\varepsilon = \frac{C_\mu^{\frac{3}{4}} k(X_2)^{3/2}}{l} \quad (2.17)$$

$$l = \min \left\{ \kappa X_2 \left( 1 + 3.5 \frac{X_2}{\delta} \right)^{-1}, C_\mu \delta \right\} \quad (2.18)$$

where  $C_\mu$  is a turbulent-viscosity constant in the  $k$ - $\varepsilon$  turbulence model. In order to ensure that  $k(X_2)$  has some finite small value as  $X_2$  approach  $\delta$  and beyond, the term  $0.00001 U_\infty^2$  is specified in the expression. For all the numerical simulations along flat bottom surface and the GRP cover, a law of wall is used. The law of wall used for smooth seabed and the smooth GRP cover is shown in Equation 2.6. At the outlet boundary, the pressure is set to be zero. As the top wall is sufficiently far distant from the bottom and the structure, zero gradient boundary condition is used for the pressure. In addition, the horizontal velocity ( $u$ ) is equal to the free stream velocity and the vertical velocity ( $v$ ) is zero. On the flat bottom surface (seabed) and the wall of the GRP cover, a no-slip condition is applied (i.e.  $u = v = 0$ ).



**Figure 2.29 Fitted logarithmic boundary layer profile on experimental boundary layer from Fujimoto et al. (1975) at the upstream location**

### 2.3.4 Similarity parameters

In order to compare the CFD simulations results with the experimental values, dynamic similarity needs to be ensured. Several non-dimensional parameters must be identical in order to achieve dynamic similarity. This includes similarity of  $Re_D$  of the flow, boundary layer thickness and boundary layer profile. The  $Re_D$  and boundary layer thickness similarity are achieved by adjusting the viscosity and the geometry respectively. Boundary layer profile is calculated through logarithmic curve fitting to the experimental boundary layer profile by Fujimoto et al. (1975). The fitted boundary layer for numerical simulations on the experimental values is shown in Figure 2.29. The boundary layer location is at the upstream face of the GRP cover, as done by Fujimoto et al. (1975). Numerical simulation results can only be compared with the experiments if the flow characteristics are identical in both the cases. Figure 2.29 show that the present CFD simulation can reproduce the velocity profile reported by Fujimoto et al. (1975) under the same similarity parameters.

In order to validate the computational setup, a validation study is carried out. Since the experimental results were available only for the square geometry at  $Re_D = 1.19 \times 10^5$ ,  $5.12 \times 10^4$  and  $3.41 \times 10^4$  for  $\delta/D = 0.73$ ,  $1.7$  and  $2.55$  respectively, these values have only been compared with the experimental results. Similar conditions are further used to calculate the hydrodynamic force coefficients at  $Re_D = 1.00 \times 10^6$  for square, triangular and semi-circular GRP covers. Since no experimental results between the present simulation and experiments is available for the triangular and semi-circular geometry, the result comparison cannot be performed for these two geometries. The wall of the structure is set to be smooth and having no surface roughness for all the simulations conducted in the present study.

## 2.4 Numerical set-up validation study

The present numerical results are compared with the corresponding experimental data reported by Fujimoto et al. (1975). The validation study is done for the boundary layer flow over square cover at  $\delta/D = 0.73, 1.70$  and  $2.55$  at  $Re_D = 1.19 \times 10^5, 5.12 \times 10^4$  and  $3.41 \times 10^4$ , respectively.

### 2.4.1 Mesh and domain convergence

Mesh convergence study has to be performed when there is a need to affirm that the solution is sufficiently mesh independent. This is done by increasing the total amount of elements in the computational domain and quantifying its effect on the solution. A mesh convergence study also enables the analyser to decide the number of cells that are necessary to get the desired numerical accuracy of the results. Optimization in the number of cells is needed owing to the fact that fewer cells can result in large numerical errors and too many cells may result in a large computational cost. Typically, a mesh convergence test involves illustrating a course, medium and fine mesh, where the medium mesh should have shown sufficient converged solution with reasonable computational cost. Mostly the CFD analyst proceeds with results from the medium mesh owing to the optimal balance of numerical accuracy and computational cost. The mesh convergence study for the square GRP cover with  $\delta/D$  and  $Re_D$  same as the experiments by Fujimoto et al. (1975) is illustrated in Table 2.2, where  $x_R/D$  is the recirculation length also called as reattachment length is shown for each mesh.

A good mesh independence of the grid is observed in this study of mesh convergence as the increase in the amount of elements is having a small change in hydrodynamic quantities. The difference in  $x_R/D$  is 1.2%. The value of  $C_L$  differ with a relative difference of 5.0% between the coarsest and finest mesh for this case. The value of  $C_D$  differ with a relative difference of 6.8% between the coarsest and finest mesh for this case. While the difference of hydrodynamic quantities between the converged and the finest mesh is less than 2% among all the cases. This indicates that the grid has sufficient resolution. The fine mesh is used in order to ensure that there are sufficient amount of elements close to the structure and the flat bottom surface to capture accurate local flow details. It also ensures avoiding elements with high aspect ratios. A domain size convergence study is also carried out for different domain heights to ensure that the height of the domain does not influence the solution. The results are shown in Table 2.3.

The results with a symbol ‘\*’ are selected for further analysis and discussion.



**Table 2.2 Hydrodynamic quantities from grid convergence study for square cover at experimental parameters ( $\delta/D = 0.73, 1.70$  &  $2.55$  at  $Re_D = 1.19 \times 10^5, 5.12 \times 10^4$  &  $3.41 \times 10^4$ )**

Elements	$\delta/D$	$C_D$	$C_L$	$x_R/D$	$Re_D$
51126	0.73	1.03	0.72	13.12	$1.19 \times 10^5$
73676*	0.73	1.02	0.74	13.25	$1.19 \times 10^5$
95674	0.73	1.02	0.73	13.28	$1.19 \times 10^5$
44292	1.70	0.88	0.64	12.12	$5.12 \times 10^4$
66786*	1.70	0.83	0.62	12.06	$5.12 \times 10^4$
88902	1.70	0.82	0.63	12.03	$5.12 \times 10^4$
37124	2.55	0.76	0.59	11.96	$3.41 \times 10^4$
59864*	2.55	0.75	0.57	11.86	$3.41 \times 10^4$
81542	2.55	0.75	0.56	11.84	$3.41 \times 10^4$

**Notes:** The converged mesh is shown with symbol ‘\*’.

**Table 2.3 Hydrodynamic quantities from given domain height when  $\delta/D = 0.73$  and  $Re_D = 1.19 \times 10^5$**

Domain height $H$	$C_D$	$C_L$	$x_R/D$
20D	1.04	0.75	13.31
25D*	1.02	0.74	13.25
30D	1.01	0.73	13.22
35D	1.01	0.73	13.23

**Notes:** The converged domain height is shown with symbol ‘\*’.

When the domain height  $H$  is increased from  $25D$  to  $30D$  a relative difference of  $0.2\%$  for  $x_R/D$ ,  $1.4\%$  for  $C_L$  and  $0.9\%$  is for  $C_D$  is observed. While increasing  $x_R/D$  from  $30D$  to  $35D$ , negligible change is observed in the hydrodynamic quantities.  $H = 25D$  selected previously showed that no influence of the upper boundary condition is reflected on the hydrodynamic quantities. The domain height used for further analysis is marked with a symbol ‘\*’.

## 2.5 Results comparison with Fujimoto et al. (1975)

### 2.5.1 Force coefficients:

Experiments show the presence of small velocity and pressure fluctuations for boundary layer flow over two-dimensional long square cross-section according to Liu et al. (2008). Compared to the mean velocities and pressure, the fluctuations are negligibly small. Hence,  $C_D$  and  $C_L$  may be assumed to have negligible fluctuations.

The values of  $C_D$  in the present study are compared with the published experimental data from Fujimoto et al. (1975). The  $C_D$  values are tabulated in Table 2.4 for a square cover for various values of  $\delta/D$  and  $Re_D$ .

**Table 2.4 Hydrodynamic quantities for square cross-section compared to the equivalent values from experiments performed by Fujimoto et al. (1975)**

$\delta/D$	$C_D$ (Present Study)	$C_D$ (Fujimoto et al., 1975)	$Re_D$
0.73	1.02	0.96	$1.19 \times 10^5$
1.70	0.83	0.82	$5.12 \times 10^4$
2.55	0.75	0.75	$3.41 \times 10^4$

Table 2.4 shows a good agreement between numerical results and experimental data. The maximum relative change of  $C_D$  is found to be less than 5.8% for  $\delta/D = 0.73$ . The results listed in Table 2.4 are also compared graphically in Figure 2.30 to get a better result comparison understanding.

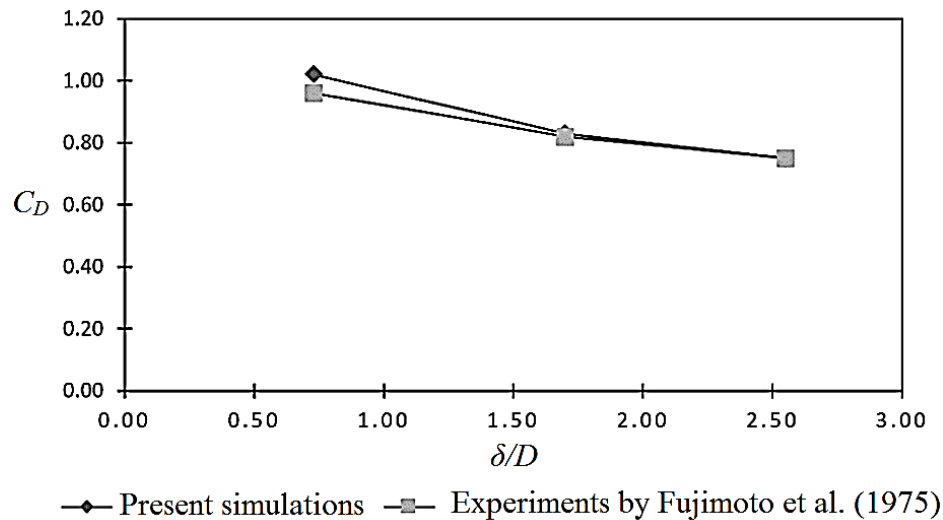


Figure 2.30 Comparison of  $C_D$  numerical and experimental results (Fujimoto et al., 1975) for  $\delta/D = 0.73$ , 1.70 & 2.55

It can be inferred that the results from the numerical study are in good agreement with the published experimental data (Fujimoto et al., 1975) in general. Hence, the method is believed to give accurate results for analysing boundary layer flow over the simplified GRP covers.

## 2.6 Results

In this section, hydrodynamic force coefficients, velocity profiles at different locations, velocity contours and streamlines of the flow around the three GRP covers are presented and discussed. Hydrodynamic force coefficients presented in this section are at  $Re_D = 1.00 \times 10^6$  for the three different boundary layer thickness ( $\delta/D = 0.73$ , 1.70 & 2.55). The results of hydrodynamic force coefficients for  $Re_D = 3.41 \times 10^4$ ,  $5.12 \times 10^4$  &  $1.19 \times 10^5$  used for result validation purpose with the experimental data by Fujimoto et al. (1975) have already been mentioned in Section 2.4. However, the results of velocity profiles at different locations, velocity contours and streamlines are presented and discussed for  $Re_D = 3.41 \times 10^4$ ,  $5.12 \times 10^4$  &  $1.19 \times 10^5$  and  $\delta/D = 0.73$ , 1.70 & 2.55 respectively.

### 2.6.1 Drag coefficient, lift coefficient and recirculation length

#### Square cover

Table 2.5 shows the mesh convergence study of square geometry at  $Re_D = 1.00 \times 10^6$ . The converged mesh is marked with a '\*' on top of the number of elements for corresponding

boundary layer thickness. It is obvious from the Table 2.5 that for the mesh finer than the converged mesh, the values of  $C_D$ ,  $C_L$  and  $x_R/D$  change negligibly small; hence, the results are mesh independent.

**Table 2.5  $C_D$ ,  $C_L$  and  $x_R/D$  of square geometry**

Elements	$\delta/D$	$C_D$	$C_L$	$x_R/D$	$Re_D$
67656	0.73	1.23	0.88	12.30	$1.00 \times 10^6$
87932*	0.73	1.17	0.84	12.45	$1.00 \times 10^6$
107712	0.73	1.16	0.82	12.50	$1.00 \times 10^6$
56466	1.70	0.99	0.83	11.15	$1.00 \times 10^6$
76922*	1.70	0.98	0.78	11.25	$1.00 \times 10^6$
96192	1.70	0.98	0.77	11.30	$1.00 \times 10^6$
51616	2.55	0.94	0.78	10.60	$1.00 \times 10^6$
71324*	2.55	0.91	0.74	10.80	$1.00 \times 10^6$
91132	2.55	0.90	0.72	10.85	$1.00 \times 10^6$

**Notes:** The converged mesh is shown with symbol ‘\*’.

It can also be observed that the values of  $C_D$  and  $C_L$  decreases as the  $\delta/D$  increases. The reason is that as for the first case ( $\delta/D = 0.73$ ), the boundary layer thickness is smaller than height of GRP cover, the top portion of the cover experiences maximum possible incoming fluid velocity in the domain i.e. free stream velocity. Therefore, the drag and lift forces are maximum. However, as the boundary layer thickness increases from the height of the GRP cover in the second case ( $\delta/D = 1.70$ ) and third case ( $\delta/D = 2.55$ ), the cover experience the incoming flow velocity lower than the free stream velocity. This is because the cover lies within the boundary layer flow and the lift and drag forces are smaller as compared to the first case. It is found that when the boundary layer thickness is larger, hydrodynamic forces experienced by the GRP cover will be smaller. A similar behaviour is observed for the  $x_R/D$ .

### Triangular cover

Table 2.6 shows the mesh convergence study as well as lift and drag coefficients and recirculation length for all the three cases of boundary layer thickness studied for triangular geometry. Meshes with the converged results are shown with a ‘\*’ on top of number of elements for each case.

**Table 2.6  $C_D$ ,  $C_L$  and  $x_R/D$  of triangular geometry**

Elements	$\delta/D$	$C_D$	$C_L$	$x_R/D$	$Re_D$
73783	0.73	0.94	0.21	10.15	$1.00 \times 10^6$
93455*	0.73	0.91	0.18	10.17	$1.00 \times 10^6$
123250	0.73	0.90	0.17	10.18	$1.00 \times 10^6$
65476	1.70	0.88	0.16	10.10	$1.00 \times 10^6$
83932*	1.70	0.86	0.13	10.14	$1.00 \times 10^6$
94356	1.70	0.85	0.13	10.16	$1.00 \times 10^6$
57882	2.55	0.81	0.15	10.03	$1.00 \times 10^6$
76782*	2.55	0.78	0.12	10.07	$1.00 \times 10^6$
88932	2.55	0.76	0.11	10.09	$1.00 \times 10^6$

**Notes:** The converged mesh is shown with symbol ‘\*’.

A similar trend for the variation of  $C_D$ ,  $C_L$  and  $x_R/D$  can be observed for the triangular shaped cover in Table 2.6 as for the square shaped cover in Table 2.5. It is interesting to note that the  $C_D$ ,  $C_L$  and  $x_R/D$  shows relatively little change with increase in  $\delta/D$  as compared to the square shaped cover. This is further explained in Section 2.6.4, where streamlines are discussed.

### Semi-circular cover

Table 2.7 shows the mesh convergence study as well as lift and drag coefficients and recirculation length for all the three cases of  $\delta/D$  studied for semi-circular geometry. The converged mesh is shown with a ‘\*’ on top of number of elements for each case.

**Table 2.7  $C_D$ ,  $C_L$  and  $x_R/D$  of semi-circular geometry**

Elements	$\delta/D$	$C_D$	$C_L$	$x_R/D$	$Re_D$
20018	0.73	0.24	0.85	3.42	$1.00 \times 10^6$
35622*	0.73	0.26	0.80	3.85	$1.00 \times 10^6$
45644	0.73	0.27	0.79	3.92	$1.00 \times 10^6$
18132	1.70	0.21	0.82	3.11	$1.00 \times 10^6$
32186*	1.70	0.23	0.76	3.15	$1.00 \times 10^6$
40190	1.70	0.24	0.76	3.17	$1.00 \times 10^6$
16734	2.55	0.16	0.75	2.55	$1.00 \times 10^6$
30286*	2.55	0.20	0.71	2.65	$1.00 \times 10^6$
38674	2.55	0.21	0.70	2.65	$1.00 \times 10^6$

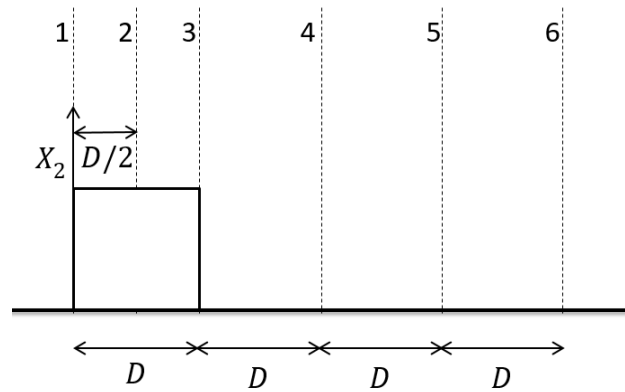
**Notes:** The converged mesh is shown with symbol ‘\*’.

$C_D$  and  $C_L$  and  $x_R/D$  for semi-circular geometry show exactly the same behaviour with the increase in  $\delta/D$  as it does for the square geometry.

## 2.6.2 Velocity profiles at different locations of the three GRP covers

### Square cover

The changes of the velocity profiles at different locations around the square GRP cover under three different incoming  $\delta/D$  are investigated. The dotted lines in Figure 2.31 show the six locations where velocity profiles are plotted for the square cover. See the numbering in Figure 2.31 for different locations where the velocity profiles are plotted.



**Figure 2.31** Locations of velocity profiles plotted on the square cover

Three velocity profiles are located on the GRP cover and the other three at consecutive distance of  $D$  downstream from the cover. The velocity profiles comparison for different  $Re_D$  at different downstream locations are shown in Figure 2.32 following the same numbering in chronological order as shown in Figure 2.31.

Figure 2.32 shows the velocity profiles at  $Re_D = 3.41 \times 10^4$ ,  $5.12 \times 10^4$  &  $1.19 \times 10^5$  for  $\delta/D = 0.73$ ,  $1.70$  &  $2.55$  respectively at six different locations shown in Figure 2.31. The velocity profiles for the three different  $\delta/D$  are close to each other for  $X_2/D < 1.5$  and deviates from each other within the range  $1.5 < X_2/D < 3$ . For  $X_2/D > 3$ , a relatively less deviation is observed as compared to the range  $1.5 < X_2/D < 3$ . The velocity profiles are reasonably closer to each other for different  $\delta/D$  because in the region around the cover, the initial velocity profile vanishes and rebuilds according to the shape of the cover. In some plots, few colour lines disappear. This is because of another line completely overlapping the disappeared line.

The first three locations are on the cover so that the profile starts at the point equal to the height of the cover i.e. 1. The velocity of fluid is zero on the cover and seabed for all the cases investigated in the present study. At location 1, the velocity of the fluid is zero at the cover and increases logarithmically. At locations 2 and 3 the fluid velocity is zero on the cover and becomes negative immediately close to the cover and develops into a logarithmic profile. The negative fluid velocity values are observed because of the recirculation of the fluid flow on the top of the cover. At locations 4, 5 & 6 the fluid velocity is zero at the seabed and immediately becomes negative for an increase in  $X_2/D$  and finally increases logarithmically. The negative values are observed because of the fluid recirculation at the downstream of the cover. It is also observed that within the range  $1.5 < X_2/D < 3$ , the velocity magnitude is greater than the free stream velocity and for  $X_2/D > 3$  the velocity starts reducing. These trends are further discussed in the Section 2.6.4.

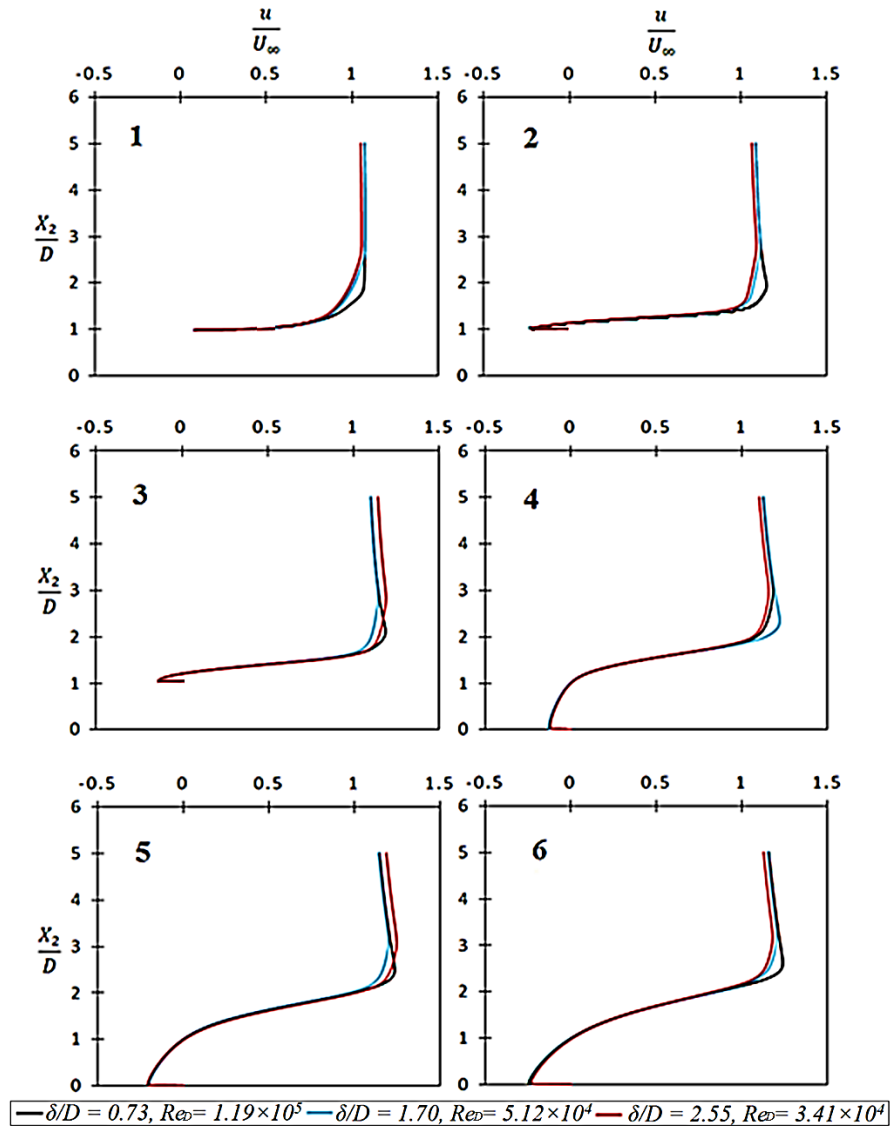


Figure 2.32 Velocity profiles on the square cover at different locations

Figure 2.33 shows the fluid velocity profiles at  $Re_D = 1.00 \times 10^6$  for  $\delta/D = 0.73, 1.70$  &  $2.55$  at six different locations shown in Figure 2.31 for the square cover. The fluid velocity profiles have a small difference to the ones observed in Figure 2.32; however, the extreme fluid velocity values are larger as compared to the Figure 2.32. For example, at location 6 in Figure 2.33, the minimum and the maximum values of fluid velocity ( $u/U_\infty$ ) for  $\delta/D = 0.73$  and  $Re_D = 1.00 \times 10^6$  are  $-0.45$  and  $1.3$  respectively. Contrarily, for  $\delta/D = 0.73$  and  $Re_D = 1.19 \times 10^5$ , the minimum and the maximum values of fluid velocity ( $u/U_\infty$ ) are  $-0.25$  and  $1.2$ .



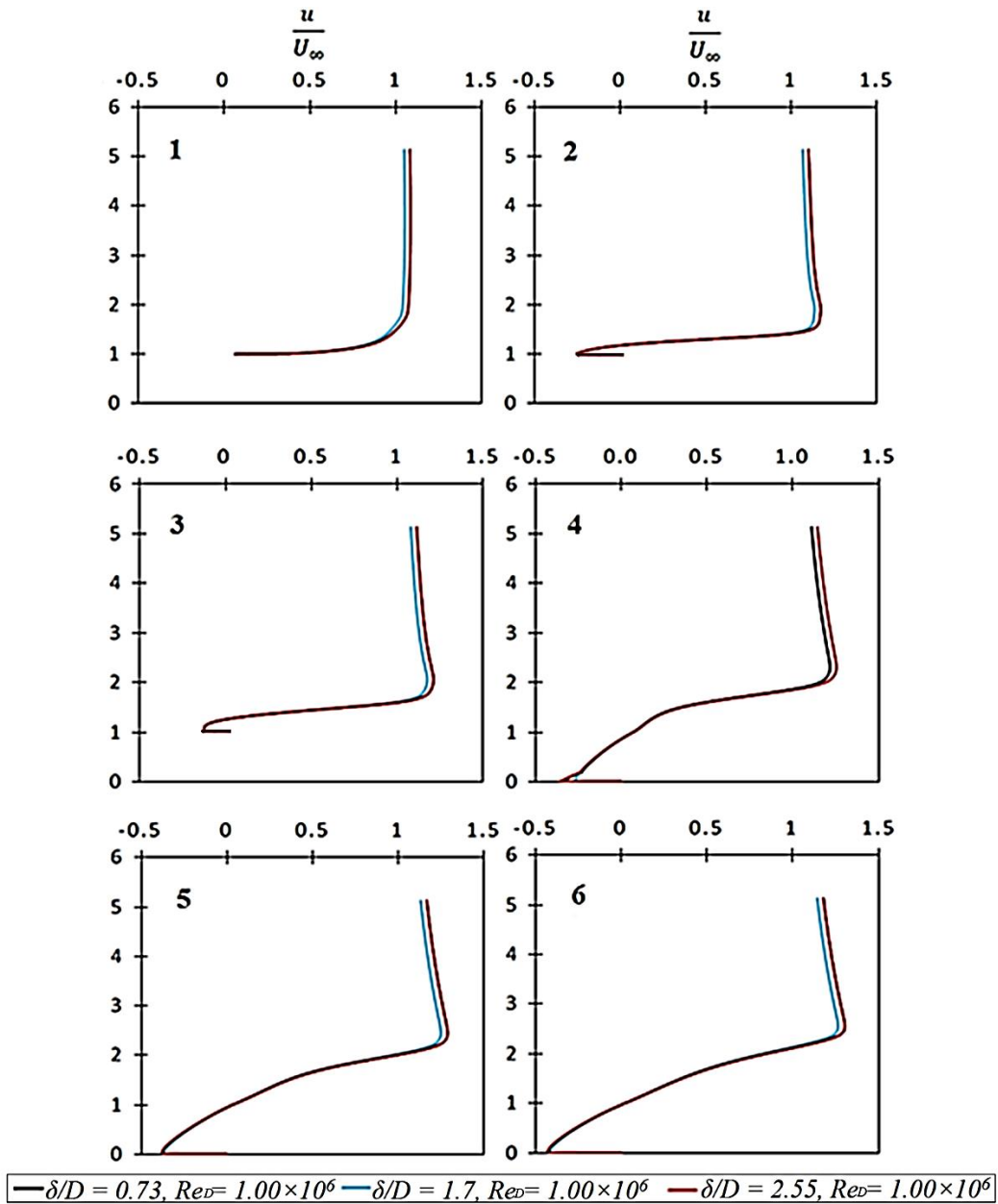


Figure 2.33 Velocity profiles on the square cover at different locations

### Triangular cover

Six location similar to the square cover are taken for the comparison of the velocity profiles around the incoming boundary layer flow at  $Re_D = 1.00 \times 10^6$  and  $\delta/D = 0.73, 1.70$  &  $2.55$  for the triangular cover. The dotted lines in Figure 2.34 show the locations where velocity profiles are plotted for triangular cover.

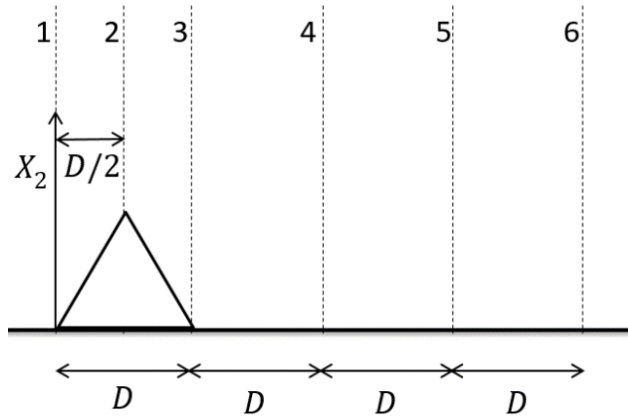


Figure 2.34 Locations of velocity profiles plotted on the triangular cover

The Figure 2.35 shows different velocity profiles at different locations of the cover. The velocity profiles for the three different  $\delta/D$  are close to each other at locations 1, 2 and 3 and deviates from each other at locations 4, 5 and 6. All the fluid velocity profiles begins at  $X_2/D=0$  except the location 2 that begins at  $X_2/D = 1$ . Contrary to the square cover, the fluid velocity profiles differ with each other in the range  $X_2/D < 1$  significantly at locations 4, 5 and 6. The location 6 also shows that the magnitude of fluid velocity is of the order  $-0.5$  for different boundary layer thickness. This reflects that the magnitude of the fluid velocity at that location ( $X_2/D \approx 0$ ) is half the magnitude of free stream velocity and moving opposite to the direction of free stream velocity.

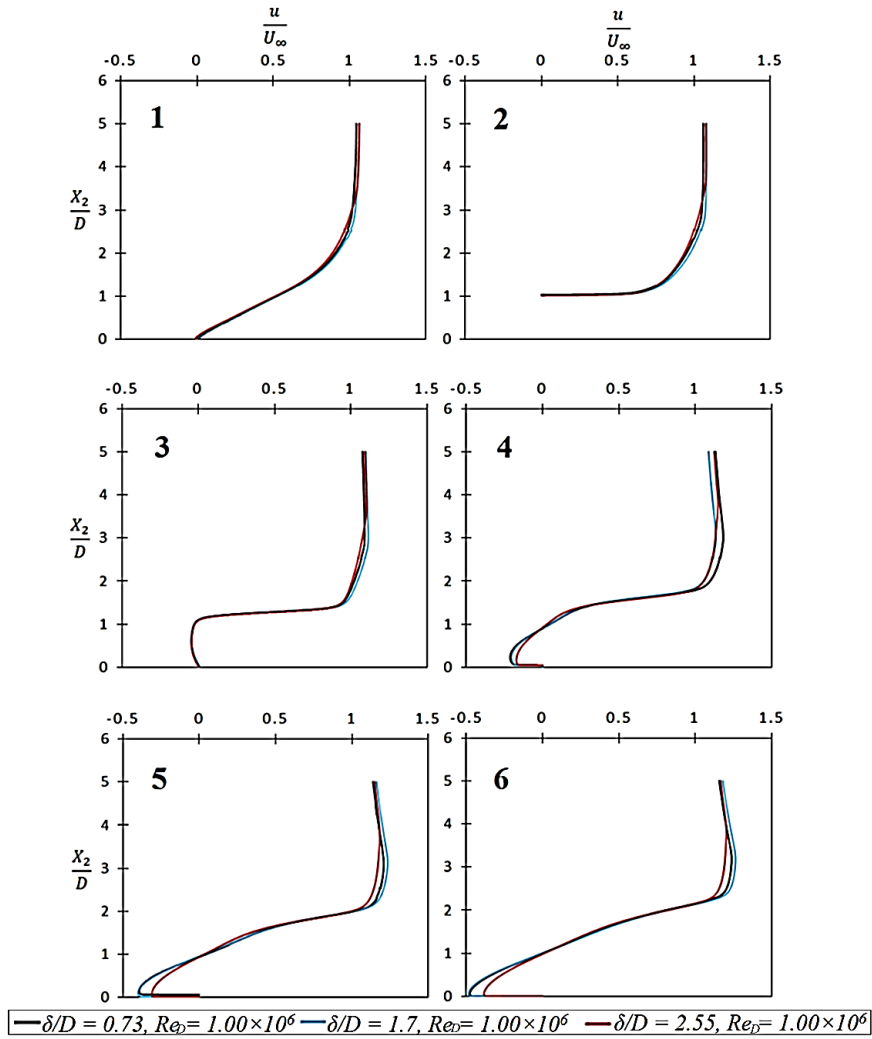


Figure 2.35 Velocity profiles on the triangular cover at different locations

### Semi-circular cover

The dotted lines in Figure 2.36 show the locations where velocity profiles are plotted for the semi-circular cover.

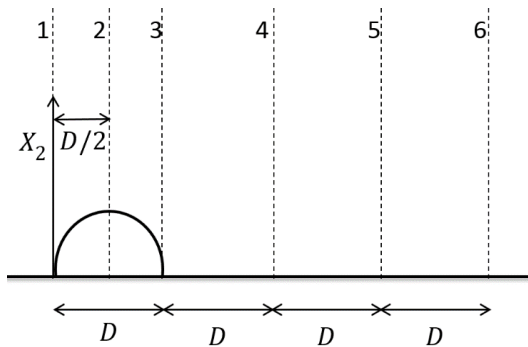


Figure 2.36 Locations of velocity profiles plotted on the semi-circular cover

The velocity profile plots for the semi-circular cover shown in Figure 2.37 are quite close to each other but not as close as those for square and triangular geometries. The reason might be that for the square and triangular geometries, the flow separation point remains same for different incoming flow conditions. However, for semi-circular cover, the flow-separation-point location changes under different incoming flow conditions. As discussed in Section 2.6.4, the velocity profiles on all three cover for the three different  $\delta/D$  are different. Hence, the flow separation points for the semi-circular cover are different for all the three discussed cases of  $\delta/D$ .

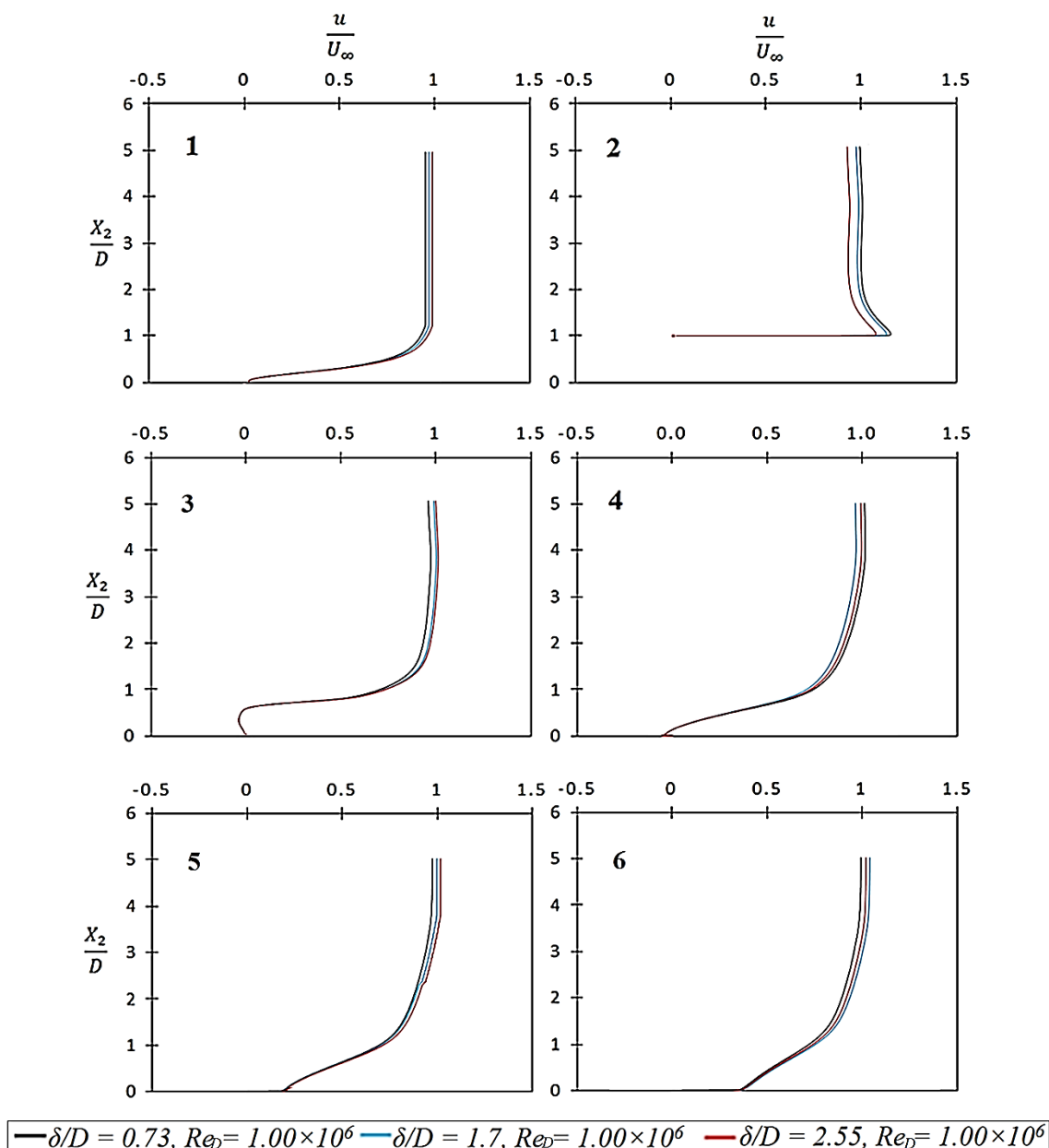


Figure 2.37 Velocity profiles on the semi-circular cover at different locations

### 2.6.3 Velocity contours

The velocity contour plots for the investigated case of flow over square, triangular and semi-circular covers are presented and discussed in this section. The red regions in the plots indicate free stream velocity. The green regions indicate the velocity profile thicknesses. The blue regions are the regions of negative velocity i.e. where recirculation of fluid takes place.

Figure 2.38 displays the velocity contour plots for square cover with the increasing  $\delta/D$  and decreasing  $Re_D$  from Figure a) to c). These plots portrait the effect of change of  $Re_D$  on the flow characteristics over the square cover. The interesting phenomenon here is the dark red region, just above the leading edge of geometry. This shows the velocity greater than the free stream velocity since the fluid streamlines come closer to each other. It must be noted that the incoming  $\delta/D$  increases, for all the three cases (a, b & c) displayed in Figures 2.38, as the flow comes closer to the cover and in the region just behind the cover it attains its highest value. The  $\delta/D$  have very small differences in the region just behind the cover for the three cases. There are two recirculation regions in the fluid domain. The larger one is downstream of the cover due to the flow separation. The size of this region decreases with the decrease in  $Re_D$ . The smaller one is upstream of the cover because of the reflection of fluid from the cover wall. The size of this recirculation region also decreases with the decrease in  $Re_D$ .

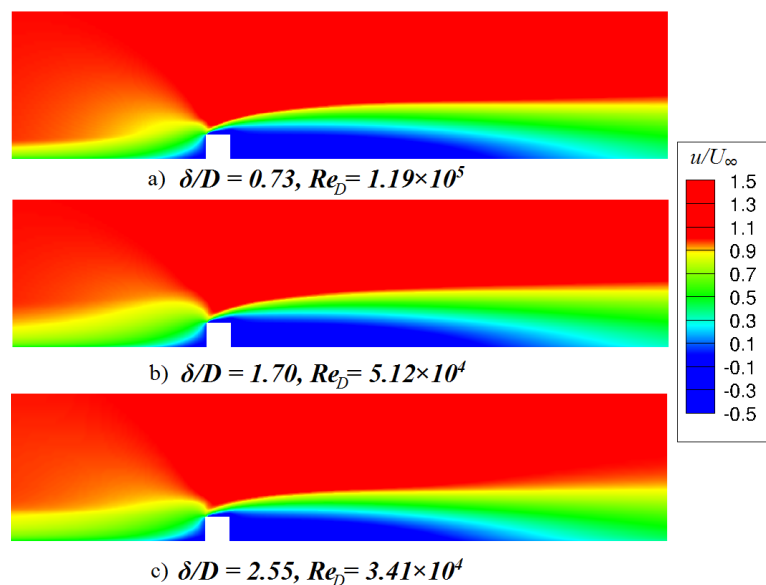


Figure 2.38 Velocity contours for the square cover a)  $\delta/D = 0.73, Re = 1.19 \times 10^5$  b)  $\delta/D = 1.70, Re = 5.12 \times 10^4$  c)  $\delta/D = 2.55, Re = 3.41 \times 10^4$

Figures 2.39 (from a to c) displays the velocity contour plots for square cover with increasing  $\delta/D$  and fixed  $Re_D$ . These plots show the effect of change of  $\delta/D$  on flow characteristics. Both the recirculation regions, upstream and downstream decreases with an increase in  $\delta/D$ . This is because the effective fluid velocity around the cover decreases with an increase in  $\delta/D$ .

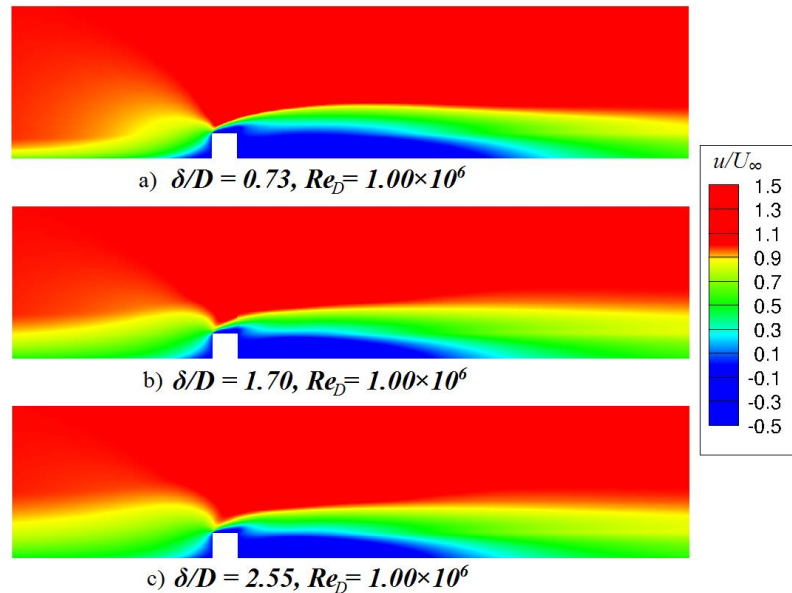
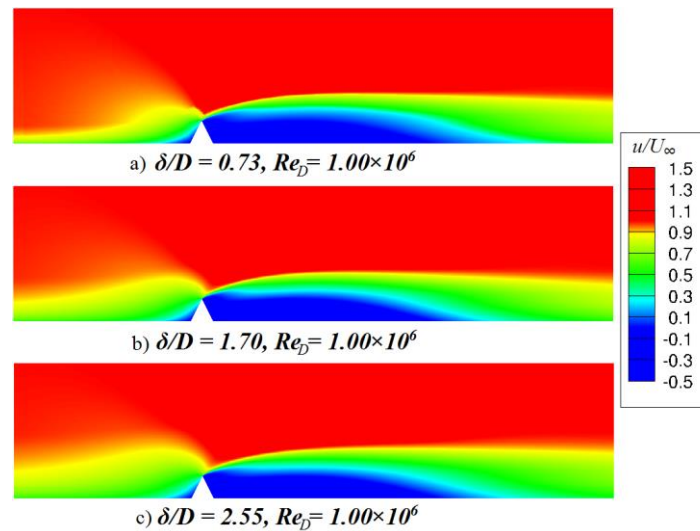


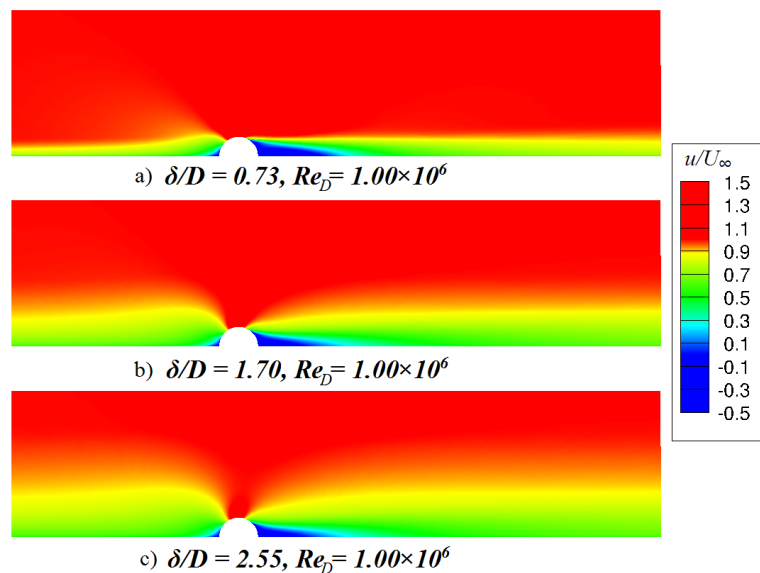
Figure 2.39 Velocity contours for the square cover a)  $\delta/D = 0.73, Re = 1.0 \times 10^6$  b)  $\delta/D = 1.70, Re = 1.0 \times 10^6$  c)  $\delta/D = 2.55, Re = 1.0 \times 10^6$

Figures 2.40 (from a to c) display the velocity contour plots for triangular cover for increasing  $\delta/D$ . The trend of velocity contours is the same as for the square cover. The triangular cover also has the velocity higher than the free stream velocity (shown as dark red region) just above the top edge of cover due to streamlines coming closer to each other. It is observed that the decrease in recirculation length is very small, with the increase in  $\delta/D$ , as compared to square cover. This is the reason for a small difference in the hydrodynamic force coefficients for the three cases of triangular cover discussed previously in Section 2.6.2.



**Figure 2.40** Velocity contours for the triangular cover a)  $\delta/D = 0.73, Re = 1.0 \times 10^6$  b)  $\delta/D = 1.70, Re = 1.0 \times 10^6$  c)  $\delta/D = 2.55, Re = 1.0 \times 10^6$

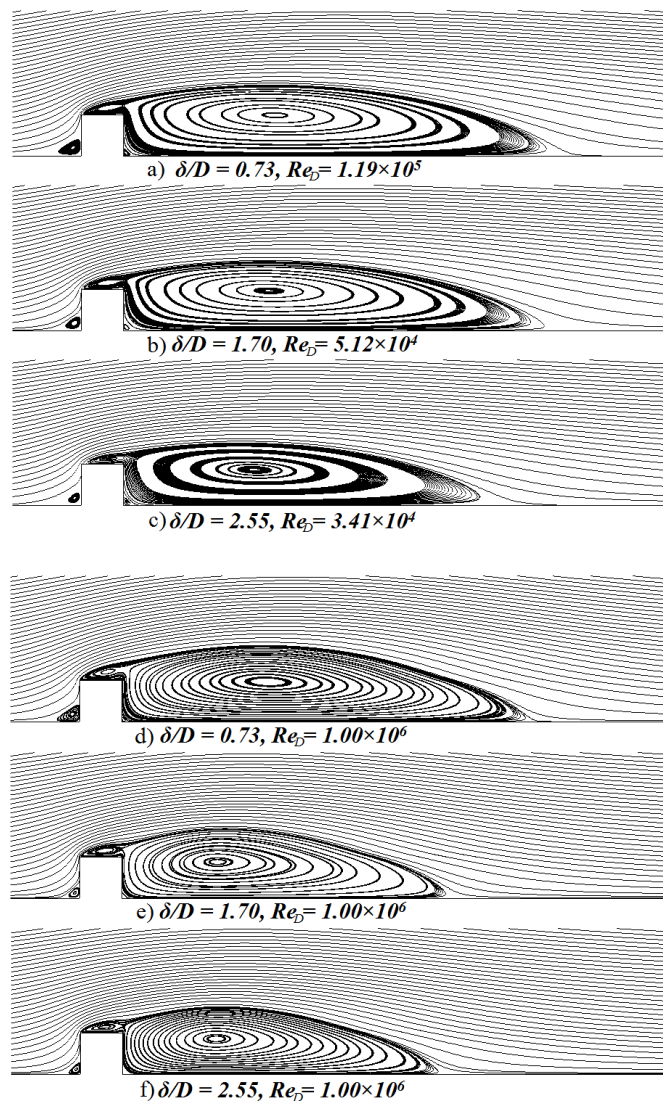
Figures 2.41 (from a to c) display the velocity contour plots for semi-circular cover with increasing  $\delta/D$ . The velocity contours for semi-circular cover show different trend as compared to the square and triangular cover. For the recirculation length downstream of the cover, the change is significant for different  $\delta/D$  as compared to the recirculation length ahead of the cover, which shows a very small difference.



**Figure 2.41** Velocity contours for the semi-circular cover a)  $\delta/D = 0.73, Re = 1.0 \times 10^6$  b)  $\delta/D = 1.70, Re = 1.0 \times 10^6$  c)  $\delta/D = 2.55, Re = 1.0 \times 10^6$

### 2.6.4 Streamlines

Figures 2.42 (a to f) displays the streamlines plots for six investigated cases of flow over square cover. The streamlines for square cover portrait the same results as displayed in Figure 2.39 and discussed in Section 2.6.2. The recirculation length decreases as  $\delta/D$  increases. An interesting fact to note here is that the flow separation point for each of the three cases is same i.e. at the upper initial corner edge. The negative values of velocity on the top surface of square cover observed in Section 2.6.2 are due to the small recirculation region present on the top of the geometry. A small recirculation of flow can be observed at the front wall of cover for all the six investigated cases. In the Figures 2.42 a) to e), as the  $\delta/D$  decreases, the size of recirculation region upstream of the cover increases.

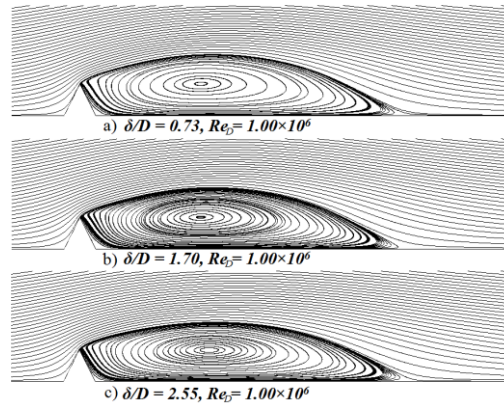


**Figure 2.42** Streamlines on the square cover a)  $\delta/D = 0.73, Re = 1.19 \times 10^5$  b)  $\delta/D = 1.70, Re = 5.12 \times 10^4$  c)  $\delta/D = 2.55, Re = 3.41 \times 10^4$  d)  $\delta/D = 0.73, Re = 1.0 \times 10^6$  e)  $\delta/D = 1.70, Re = 1.0 \times 10^6$  f)  $\delta/D = 2.55, Re = 1.0 \times 10^6$



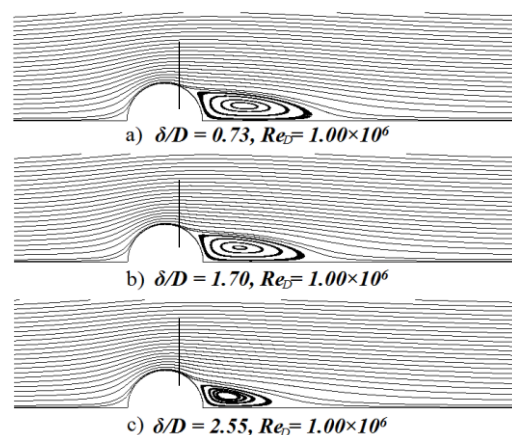
### Triangular cover

The triangular cover has the same flow separation point for all three cases of  $\delta/D$  just like square geometry as shown in Figure 2.43 but there is no recirculation region upstream of the cover in any of the three discussed cases. This is the reason why the recirculation length shows only minor reduction as  $\delta/D$  increases.



**Figure 2.43** Stream lines on the triangular cover a)  $\delta/D = 0.73, Re = 1.0 \times 10^6$  b)  $\delta/D = 1.70, Re = 1.0 \times 10^6$  c)  $\delta/D = 2.55, Re = 1.0 \times 10^6$

Contrary to the square and triangular geometry, the semi-circular geometry has different flow separation points for each of the three investigated cases. Straight vertical lines are drawn in each streamline plot respective to the point of flow separation for case 'a' ( $\delta/D = 0.73, Re = 1.0 \times 10^6$ ) in the Figure 2.44 to make it observable. Even though the difference in the flow separation is quite small, still it becomes the reason behind slightly different behaviour of flow across semi-circular cover as compared to the square and triangular covers.



**Figure 2.44** Stream lines on the semi-circular cover a)  $\delta/D = 0.73, Re = 1.0 \times 10^6$  b)  $\delta/D = 1.70, Re = 1.0 \times 10^6$  c)  $\delta/D = 2.55, Re = 1.0 \times 10^6$

## 2.7 Conclusion

CFD simulations of the boundary layer flow over three different GRP cover geometries on a flat seabed is performed. RANS method with the standard  $k-\varepsilon$  model at high  $Re_D$  is applied. Results from the present numerical simulations show a good agreement of  $C_D$  with the experimental results published by Fujimoto et al. (1975) for  $\delta/D = 0.73, 1.70$  &  $2.55$  at  $Re_D = 1.19 \times 10^5, 5.12 \times 10^4$  &  $3.41 \times 10^4$  respectively.

The study also showed that for the square and triangular geometry covers, the drag coefficient is higher as compared to the lift coefficient for all the three different cases studied. However, for the semi-circular GRP cover, the lift coefficient is higher as compared to the drag coefficient for all the different  $\delta/D$  studied. The drag coefficient of the square cover is largest and for semi-circular cover is the lowest among all the covers. This is because the square cover gives a large obstruction to the fluid flow while the semi-circular cover gives the least obstruction. The lift coefficient of the semi-circular cover is the largest among all the covers whereas it is the least, for triangular cover. This is because of the geometry of these covers.

The incoming velocity profiles at different locations, velocity contours and the streamlines of the incoming flow shows a strong agreement with each other. This shows that the numerical method used in the present study is capable of predicting hydrodynamic force coefficients with a reasonable accuracy for the GRP covers on flat seabed.

# Chapter 3

## On-bottom stability analysis

### 3.1 Introduction

On-bottom stability analysis is carried out to study the effects of hydrodynamic forces on subsea protection covers while they are placed on seabed. Subsea covers should be stable on the seabed when exposed to the hydrodynamic forces to achieve effective functionality. They should be designed to refrain floatation under the effect of buoyancy, waves and current. Stability of the subsea cover under the effect of buoyancy is termed as static stability, while the stability of the cover under waves and current action is termed as dynamic stability. The present study discusses the comparison of behaviour of the GRP cover geometries under different loading conditions. The static stability of the subsea cover is independent of the geometry parameters. This is discussed specifically in Section 3.2. Dynamic stability of the cover depends on the cover's geometry. On-bottom stability analysis is essential for subsea protection covers in order to ensure safe operations.

### 3.2 Static stability

Static stability is the vertical stability of the subsea cover under the effect of buoyancy. In order to achieve sufficient static stability, the weight of the cover should be greater than the buoyancy force. According to DNV-RP-F109 (2010), following criterion must be satisfied to ensure static stability of the protection cover:

$$\gamma_w \cdot \frac{B}{W+B} \leq 1.00 \quad (3.1)$$

where,

- $\gamma_w$  = Safety factor = 1.10 (DNV-RP-F109, 2010)
- $B$  = Buoyancy force
- $W$  = Submerged weight
- $W+B$  = Dry weight
- $V$  = Volume of displaced water

$$W+B=Mg \quad (3.2)$$

where,  $M$  = Mass of Cover  
 $g$  = Gravitational acceleration =  $10 \text{ ms}^{-2}$

Let,  $\rho_{grp}$  = Density of GRP =  $2000 \text{ Kg/m}^3$  (Assumed)

thus  $V_{cover}$  = Volume of Cover =  $\frac{M}{\rho_{grp}}$

and  $\rho_{sw}$  = Density of Salt Water =  $1025 \text{ Kg/m}^3$  (DNV-RP-F109, 2010)

$$B = V\rho_{sw}g \quad (3.3)$$

$$B = \frac{M}{\rho_{grp}}\rho_{sw}g \quad (3.4)$$

$$B = \frac{\rho_{sw}}{\rho_{grp}}Mg \quad (3.5)$$

Placing Equation (3.2) and Equation (3.5) in Equation (3.1)

$$\gamma_w \cdot \frac{\frac{\rho_{sw}}{\rho_{grp}}Mg}{Mg} \leq 1.00 \quad (3.6)$$

$$\gamma_w \cdot \frac{\rho_{sw}}{\rho_{grp}} \leq 1.00 \quad (3.7)$$

Equation 3.7 shows that the static stability criterion for a GRP cover according to DNV-RP-F109 (2010) is the ratio of seawater density and GRP material density. Here,  $\gamma_w$  can be expressed as the safety factor used in this criterion. Equation 3.7 is independent of the geometry parameters. Consequently, the static stability of a structure will remain independent of the cross-section provided that the material remains the same. The weight and volume of the GRP covers are calculated from the cad model shown in Appendix A. Following is the summary of static stability of the three GRP covers:

**Table 3.1 Summary of the results of static vertical stability**

Parameters	Square	Triangular	Semi-circular
Criterion ( $\gamma_w \frac{B}{W+B}$ )	0.56	0.56	0.56
Volume	0.78 m <sup>3</sup>	0.80 m <sup>3</sup>	0.66 m <sup>3</sup>
Buoyancy Force	7.8 kN	8.0 kN	6.6 kN
Weight	15.3 kN	15.7 kN	12.9 kN
Net Downward Force	7.5 kN	7.6 kN	6.3 kN

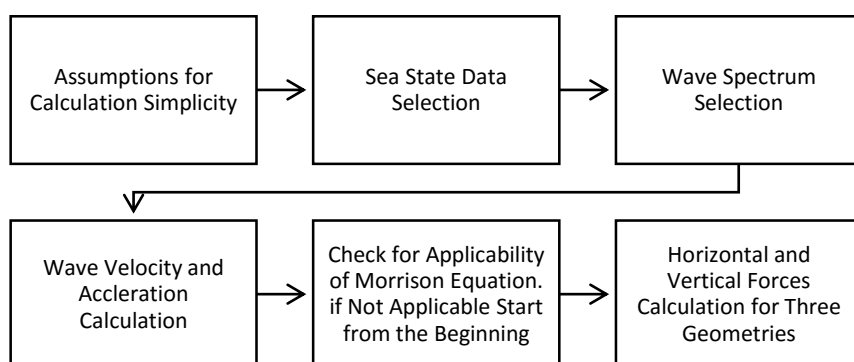
From the Table 3.1 it can be seen that DNV-RP-F109, (2010) criterion is fulfilled by the three covers. However, if the criterion is not satisfied, following measures can be taken:

- Use a denser material in the GRP matrix layout: A denser matrix material can help increasing the total weight without any extra material requirement. This solution has matrix availability and strength limitations.
- Couple concrete blocks with the GRP cover mud mats: Concrete blocks can be attached with the mud mats to increase weight however, this increases the cover cost and may introduce localised stress concentrations during transportation and installation at the coupling locations.
- ROV based submergence: ROV based submergence can serve as a cheap alternative. The instability situation for the protection cover is more likely to take place only during installation period, before the protection cover is rock dumped. ROV weight can be applied by placing it on the top of cover to get it stable until the cover is rock dumped.

### 3.3 Dynamic stability

The stability of the cover under the dynamic effect of waves and current is called dynamic stability. Dynamic stability incorporates both horizontal and vertical stability of the cover. Under the effect of waves and current, GRP cover has the possibility to move horizontally as well as vertically. In order to achieve dynamic stability the cover should be stable at its location. Horizontal stability of a GRP cover is ensured when the net horizontal force (drag force) is less than the frictional force between mud mats and seabed. Vertical stability of a GRP cover is ensured when the net vertical force (lift force + buoyancy force) is less than the weight of the cover.

In order to calculate horizontal and vertical forces, horizontal and vertical velocities are required. These velocities are calculated based on a particular wave spectrum. In the North Sea, Jonswap spectrum is widely accepted and is used in the present study. The horizontal and vertical forces are calculated by the following algorithm:



**Figure 3.1 The horizontal and vertical forces calculation scheme**

#### 3.3.1 Assumptions

Following are the assumptions made for the calculation of horizontal and vertical forces:

- Morrison equations and Froude-Kriloff theory are applicable because structure height is small as compared to the wavelength.
- It is assumed that the installation period is less than 12 months since subsea installation of cover is a short duration operation. After installation, the protection cover is rock dumped to ensure sufficient stability. It can be assumed that the dynamic loads are only significant before the cover is rock dumped.

According to DNV-RP-F109 (2010), for the design of 12 months' operation, the most severe condition of the following two must be used:

- The seasonal 10-year return condition for waves combined with the seasonal 1-year return condition for seasonal current.
- The seasonal 1-year return condition for waves combined with the seasonal 10-year return condition for current.

Generally, 10-year return condition for waves with 1-year return current dominates for relatively smaller water depth as compared to 1-year return condition for waves and 10-year return condition for current. Wave action dominates for smaller water depths and current action dominates for larger water depth.

### 3.3.2 Sea State

A general sea state is taken from Ghebregiorghis (2014) for the present study.




**Table 3.2 Sea state data for 1-year and 10-year return conditions**

Parameter	1-Year Return condition	10-Year Return Condition
Significant Wave Height $H_s$	<i>10.3 m</i>	<i>12.6 m</i>
Peak Period $T_p$	<i>13.2 s</i>	<i>14.7 s</i>
Current Velocity $V_c$	<i>0.36 m/s</i>	<i>0.51 m/s</i>
Water Depth $D$	<i>104 m</i>	<i>104 m</i>

### 3.3.3 Hydrodynamic force coefficients

Added mass is taken from DNV-RP-H103 (2011). Drag and lift coefficients are taken from Chapter 2. The highest values of the drag and lift coefficients among all the simulations are selected to ensure conservativeness. Selected hydrodynamic force coefficients used in the calculation are tabulated in Table 3.3.

**Table 3.3 Hydrodynamic force coefficients for the geometries**

Shape	Added Mass	Drag Coefficient	Lift Coefficient
Square 	1.51	1.17	0.84
Triangular 	0.75	0.91	0.18
Semi-circular 	1.0	0.26	0.8

### 3.3.4 Wave Velocity and Acceleration

The following relation checks the applicability of Jonswap spectrum:

$$3.6 < \frac{T_p}{\sqrt{H_s}} < 5 \quad (3.8)$$

$T_p$  = Peak wave period

$H_s$  = Significant wave height

If Jonswap spectrum is applicable, the time period is calculated as following DNV-RP-H103 (2011):

$$T = T_p (0.6673 + 0.05037 \gamma - 0.00623 \gamma^2 + 0.0003341 \gamma^3) \quad (3.9)$$

$T$  = Time period

$\gamma$  = Peak enhancement factor

According to DNV-RP-H103 (2011),  $\gamma$  can be calculated as:

$$\gamma = \exp \left( 5.57 - \frac{1.15 T_p}{\sqrt{H_s}} \right) \quad (3.10)$$

The dispersion relation specifies a function between the wave number corresponding to a particular frequency and the water depth. It is stated as following:



$$\omega^2 = gk \tanh(kd) \quad (3.11)$$

$k$  = Wavenumber (in radians per metre)

$\omega$  = Angular frequency (in radians per second)

$d$  = Water depth

$g$  = Acceleration due to gravity

The wave number  $k$  is calculated from the dispersion relation iteratively and is further used to calculate horizontal and vertical wave velocity.

According to DNV-RP-C205 (2010) horizontal wave velocity is expressed as following:

$$u = \omega a \frac{\cosh k(D+d)}{\sinh kd} \cos(\theta) \quad (3.12)$$

$u$  = Horizontal wave velocity

$a$  = Wave amplitude =  $0.9 H_s \times 1.1$  (according to DNV-RP-C205 (2010))

$\theta$  = Phase angle

$D$  = Height of the GRP cover

For maximum horizontal wave velocity (i.e.  $\cos(\theta) = 1$ ),

$$u = \omega a \frac{\cosh k(D+d)}{\sinh kd} \quad (3.13)$$

Similarly, maximum vertical wave velocity  $v$  is:

$$v = \omega a \frac{\sinh k(D+d)}{\sinh kd} \quad (3.14)$$

Maximum horizontal wave acceleration  $a_u$  is as following:

$$a_u = \omega^2 a \frac{\cosh k(D+d)}{\sinh kd} \quad (3.15)$$

Maximum vertical wave acceleration  $a_v$  is as following:

$$a_v = \omega^2 a \frac{\sinh k(D+d)}{\sinh kd} \quad (3.16)$$

Following is the summary of horizontal and vertical wave velocities and accelerations: The detailed calculation can be seen in the Appendix B.

**Table 3.4 Summary of wave results for 1-year and 10-year return conditions**

Parameter	1-Year Return Condition	10 Year-Return Condition
$u$	$0.180 \text{ m/s}$	$0.450 \text{ m/s}$
$v$	$0.007 \text{ m/s}$	$0.015 \text{ m/s}$
$a_u$	$0.110 \text{ m/s}^2$	$0.260 \text{ m/s}^2$
$a_v$	$0.005 \text{ m/s}^2$	$0.008 \text{ m/s}^2$

### 3.3.5 Morrison equation applicability

Morrison equation is applicable if  $D/\lambda < 0.2$  and  $H_s/\lambda < 0.14$  (non-breaking waves), where  $D$  is the height of GRP cover and  $\lambda$  is the wavelength as following (DNV-RP-H103, 2013):

$$\lambda = \frac{gT^2}{2\pi} \quad (3.17)$$

Morrison equation is found applicable according to this criterion. Detailed calculation is shown in the Appendix B.

### 3.3.6 Vertical force

According to DNV-RP-H103 (2011), the vertical force is expressed as following:

$$F_v = 0.5 \cdot \rho \cdot C_l \cdot A \cdot (u + v_c) \cdot |u + v_c| \quad (3.18)$$




$F_v$  = Vertical force

$\rho$  = Density of water




$C_l$  = Lift coefficient

$v_c$  = Current velocity

**Table 3.5 Summary of the vertical forces for 10-year waves with 1-year return current**

Shape	Vertical Force
Square 	2.8 kN
Triangular 	0.5 kN
Semi-circular 	2.7 kN

**Table 3.6 Summary of vertical forces for 1-year waves with 10-year return current**

Shape	Vertical Force
Square 	2.4 kN
Triangular 	0.4 kN
Semi-circular 	1.9 kN

The results in Tables 3.5 & 3.6 show that the 10-year wave with 1-year return current is the design governing sea state. It is also observed that triangular cover has the least vertical force from the ocean current and waves.

### 3.3.7 Horizontal force

According to DNV-RP-H103 (2013), the horizontal force is as following:

$$F_h = \rho V (1 + C_a) a_u + 0.5 \rho C_d A (u + v_c) |u + v_c| \quad (3.19)$$




$F_h$  = Horizontal force

$V$  = Added mass volume (computed from the cad model)

$C_a$  = Added mass coefficient




$C_d$  = Drag coefficient

**Table 3.7 Summary of horizontal forces for 10-year waves and 1-year return current**

Shape	Horizontal Force
Square 	11.4 kN
Triangular 	7.7 kN
Semi-circular 	6.2 kN

The square geometry cover is subject to the highest lateral force while triangular and semi-circular geometries have approximately 20% and 35% reduction in exposed lateral forces respectively.

**Table 3.8 Summary of horizontal forces for 1-year waves and 10-year return current**

Shape	Horizontal Force
Square 	10.2 kN
Triangular 	6.4 kN
Semi-circular 	5.5 kN




The results tabulated in Table 3.8 are less in magnitude than the results tabulated in Table 3.7. This shows that all the different GRP covers experience larger lateral forces in the 10-year wave combined with the seasonal 1-year return condition for current. Therefore, results

summarized in the Table 3.7 are the design governing results. It can be observed that for both conditions, the trends of lateral force are same for all covers. For example, square cover has the highest lateral force for both the return conditions. Thus, the trend of lateral forces for both conditions are consistent for a particular geometry cover. The semi-circular cover has the least lateral force because it has the lowest value of the drag coefficient.

The lateral forces calculated in this section are compared with the frictional forces to check the lateral stability. Frictional forces are calculated for the normalized frictional angle and wet weight of the cover called utilization ( $U$ ).

Utilization	$= U$	$= F_H / F_f^*$ (non-dimensional)
Normalized friction force	$= F_f^*$	$= \mu_s N / \mu_s$ (normalized friction coefficient)
Friction force	$= F_f$	$= \mu_s N$
Coefficient of static friction	$= \mu_s$	$= f \tan \varphi$
Net downward force	$= N$	$= F_{Net}$ (Table 3.1)
Friction angel	$= \varphi$	
Surface roughness (GRP to sand)	$= f$	

**Table 3.9 Summary of maximum utilization of horizontal force against frictional force**

Shape	Utilization
Square 	1.46
Triangular 	1.01
Semi-circular 	0.98

The results show that semi-circular geometry cover is the most robust against waves and current action due to the least utilization while square geometry cover has the highest utilization. It is interesting to note that the semi-circular geometry cover has relatively less lateral loads as compared to the triangular geometry cover but the utilization is almost the same.

This is because of the less downward force of semi-circular cover as compared to the triangular cover.

Results have exhibited that the square geometry cover is subject to highest utilization that makes it worst against hydrodynamic loads while the semi-circular geometry cover appears to be the best in this regard.

### *3.4 Conclusion*

For the on-bottom stability analysis of three GRP covers, triangular cover experiences the least vertical forces followed by the semi-circular cover. For the lateral forces (horizontal forces), semi-circular cover is the most stable cover among all the covers followed by triangular cover. Square cover comes out to be the least stable cover among all the three covers studied.

# Chapter 4

## Fishing activity loads

### 4.1 Introduction

GRP protection covers are used to protect pipelines from the fishing activities. Available data Ellinas (1990) indicated that about one in ten of reported pipeline incidents are due to fishing activities. The critical elements of a typical fishing gear are shown in Figure 4.1:

- (a) Trawl board
- (b) Clump weight
- (c) Sweep line
- (d) Warp line
- (e) Trawl net

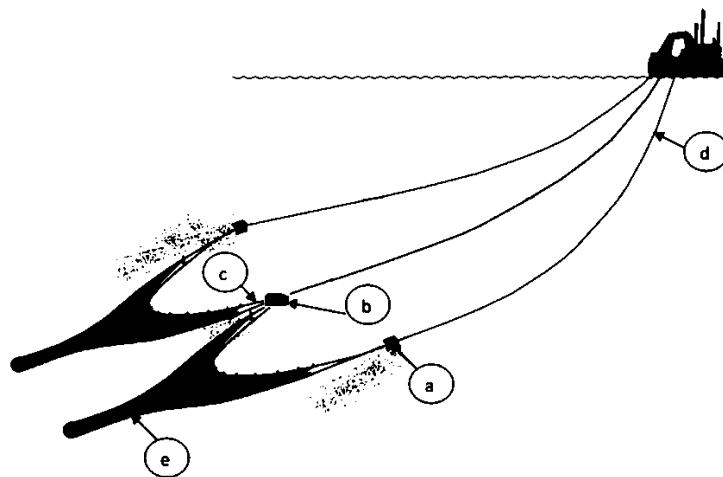


Figure 4.1 A typical fishing gear (figure developed for this thesis)

NORSOK U-002 (1998) standard has specified three different design governing load cases for the protection covers. They are as following:

- Trawl-net friction
- Trawl-board overpull
- Trawl-board impact

Since the three geometries under study have no hook up locations as shown in the Appendix A, they are considered snag free.

#### 4.1.1 Trawl-net friction

Trawl-net imparts frictional loads on the GRP cover while trawling at the surface of the protection cover. NORSOK U-002 (1998) standard states that the protection cover should be able to bear  $400\text{ kN}$  of frictional force.

#### 4.1.2 Trawl-board overpull

Trawl-board overpull is the load in which trawl-board attempts to overpull the cover since the action of force from the trawl-board forms a moment along the opposite mud mat. The schematic is shown in Figure 4.2 below:

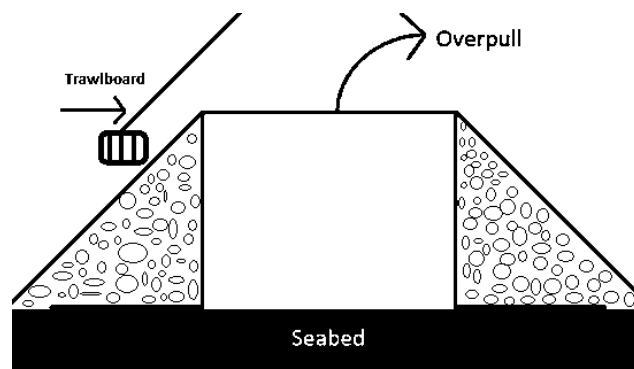


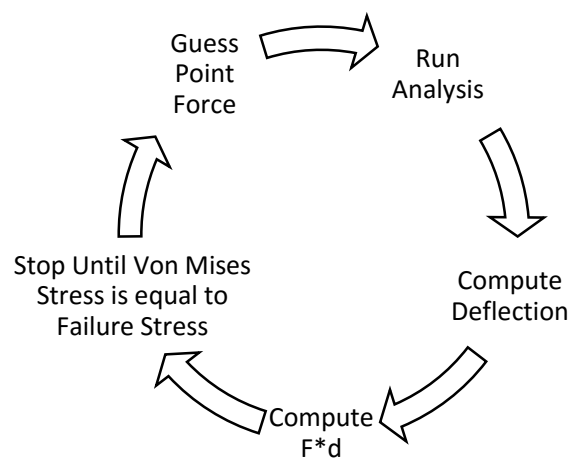
Figure 4.2 Schematic, trawlboard overpull (figure developed for this thesis)



According to NORSOK U-002 (1998), protection cover should have bearing capacity of  $300kN$  force from the trawlboard. Since the protection cover is rock dumped at both sides, the trawlboard gets in contact with rock-berm. From the rock-berm, the overpull load is transferred to the GRP material. This helps distributing the force on a larger area on to the GRP wall. It is assumed that the friction angle between rocks in the rock-berm is  $42^{\circ}$  (NAVFAC, 1986). The equivalent area on the GRP is calculated based on this friction angle.

### 4.1.3 Trawlboard impact

When trawlboard hits the cover, it applies impact loading. This can be modelled in ANSYS in two different ways. By using Explicit Dynamics, trawlboard impact can be modelled by specifying trawlboard geometry and impact velocity. The NORSOK U-002 (1998) standard has specified that subsea covers should be able to absorb an impact energy of  $13 kJ$ . The second method is to model this impact energy by taking a product of force and displacement. The maximum force and corresponding displacement defines the maximum impact absorption energy of the cover when the material is near to the failure criterion. The result optimization can be carried out iteratively through the following iteration scheme:



**Figure 4.3 Impact convergence algorithm**

Since the subsea pipeline protection covers are rock dumped, they do not have impact loading. Even in the case of trawlboard impact on the rock-berm, due to the distribution of load by the rock-berm, the impact loading becomes the same as trawlboard overpull. Hence, the trawlboard impact has not been analysed. However, trawlboard impact loading is of significance in metallic protection covers for subsea templates that are not rock dumped.

## 4.2 Theory of the GRP material

Glass reinforced plastics (GRP) materials can be analysed by three different ways: the micro-scale, meso-scale and macro-scale approaches. These three methods have their own particular areas of applicability. The micro-scale methodology offers the most comprehensive information describing the details in the microstructure of GRP material. This means the size, geometry and location of the fibres within the GRP layer. The micro-scale approach can be used to calculate mechanical properties of the material. The meso-scale methodology is used to analyse stresses and strains. In this technique, the GRP material is regarded as different layers with specified material properties. In the macro-scale method, GRP material is considered as one uniform layer of material with given material properties.

### 4.2.1 Orthotropic material

On a microscopic level, GRP material has different properties at any particular location and is a heterogeneous material. Heterogeneous properties of a material are challenging to analyse because of the different properties at different locations in the material. On average, heterogeneous materials can be approximated with orthotropic homogeneous materials. Moreover, GRP materials are direction dependent. They have different properties parallel to the fibres as compared to the transverse direction. Thus, they act as orthotropic materials with 3D material properties.

### 4.2.2 Cartesian coordinate system

In the Cartesian coordinate system, there are three planes, plane 12, plane 13, and plane 23. They have the directions  $X_1$ ,  $X_2$  and  $X_3$ . Each plane has three stresses,  $\sigma_{ij}$  where  $i$  and  $j$  are the Einstein index. ' $i$ ' corresponds to the direction normal to the plane while ' $j$ ' corresponds to the direction of the stress. An overview of the coordinate system in a 3D stress state is shown in Figure 4.4.

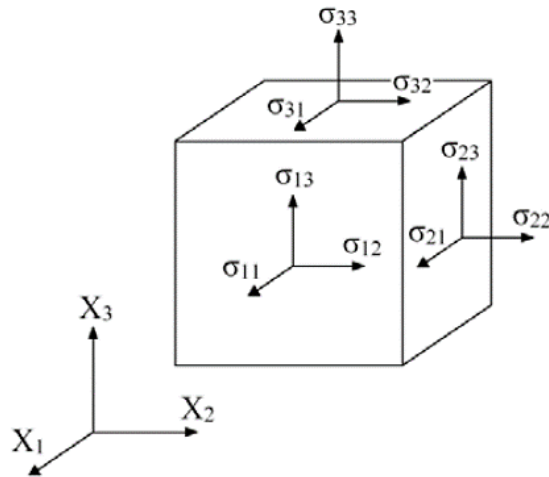


Figure 4.4 Stress components in three directions

### 4.2.3 Stress

The stress is a physical quantity defined as the force acting per unit area on the plane passing the point. The SI units of stress are  $Nm^{-2}$  or commonly used units are  $MPa$  (Barbero, 2008). A 3D stress state is shown in the matrix notation as following:

$$[\sigma] = \begin{bmatrix} \sigma_{11} & \sigma_{12} & \sigma_{13} \\ \sigma_{12} & \sigma_{22} & \sigma_{23} \\ \sigma_{13} & \sigma_{23} & \sigma_{33} \end{bmatrix} = \begin{bmatrix} \sigma_1 & \tau_{12} & \tau_{31} \\ \tau_{12} & \sigma_2 & \tau_{23} \\ \tau_{31} & \tau_{23} & \sigma_3 \end{bmatrix} \quad (4.1)$$

where,

$\sigma_{ij}$  = Stress

$\tau_{ij}$  = Shear stress

### 4.2.4 Strain

There are two types of strains being used in mechanics of solids, engineering strain and true strain. Engineering strain is defined as the ratio of change in length to the original length of the material. True strain is defined as the ratio of instantaneous change in length to the

instantaneous gauge length. When the material is elongated, the strain is regarded as positive, and in compression, it is negative. The strain tensor is shown below (Barbero, 2008):

$$[\varepsilon] = \begin{bmatrix} \varepsilon_{11} & \varepsilon_{12} & \varepsilon_{13} \\ \varepsilon_{12} & \varepsilon_{22} & \varepsilon_{23} \\ \varepsilon_{13} & \varepsilon_{23} & \varepsilon_{33} \end{bmatrix} = \begin{bmatrix} \varepsilon_1 & \gamma_{12} & \gamma_{31} \\ \gamma_{12} & \varepsilon_2 & \gamma_{23} \\ \gamma_{31} & \gamma_{23} & \varepsilon_3 \end{bmatrix} \quad (4.2)$$

where,

$$\varepsilon_{ij} = \text{Strain}$$

$$\gamma_{ij} = \text{Shear strain}$$

#### 4.2.5 Hooke's law

The material mechanics follows Hooke's Law. Within the elastic limit, Hooke's law states that the stress is directly proportional to the strain. In the simplest form, Hooke's law is defined as following for the unidirectional stress of an isotropic material (Chawla, 1987).

$$\sigma = \varepsilon \cdot E \quad (4.3)$$

where  $E$  is the elastic modulus. Hooke's law is relatively more complex for an orthotropic material. For the 3D state, nine constants that need to be described in order to define stress or strain state. A compliance matrix defines the relationship between the strain and stress and is shown as following (Barbero, 2008):

$$\begin{Bmatrix} \varepsilon_1 \\ \varepsilon_2 \\ \varepsilon_3 \\ \gamma_{23} \\ \gamma_{31} \\ \gamma_{12} \end{Bmatrix} = \begin{bmatrix} S_{11} & S_{12} & S_{13} & 0 & 0 & 0 \\ S_{12} & S_{22} & S_{23} & 0 & 0 & 0 \\ S_{13} & S_{23} & S_{33} & 0 & 0 & 0 \\ 0 & 0 & 0 & S_{44} & 0 & 0 \\ 0 & 0 & 0 & 0 & S_{55} & 0 \\ 0 & 0 & 0 & 0 & 0 & S_{66} \end{bmatrix} \begin{Bmatrix} \sigma_1 \\ \sigma_2 \\ \sigma_3 \\ \tau_{23} \\ \tau_{31} \\ \tau_{12} \end{Bmatrix} \quad (4.4)$$

where  $S_{ij}$  is the constant and  $[S]$  is the compliance matrix. The inverted matrix of  $[S]^{-1}$  = the stiffness matrix  $[C]$  and is stated as:

$$\begin{Bmatrix} \sigma_1 \\ \sigma_2 \\ \sigma_3 \\ \tau_{23} \\ \tau_{31} \\ \tau_{12} \end{Bmatrix} = \begin{bmatrix} C_{11} & C_{12} & C_{13} & 0 & 0 & 0 \\ C_{12} & C_{22} & C_{23} & 0 & 0 & 0 \\ C_{13} & C_{23} & C_{33} & 0 & 0 & 0 \\ 0 & 0 & 0 & C_{44} & 0 & 0 \\ 0 & 0 & 0 & 0 & C_{55} & 0 \\ 0 & 0 & 0 & 0 & 0 & C_{66} \end{bmatrix} \begin{Bmatrix} \varepsilon_1 \\ \varepsilon_2 \\ \varepsilon_3 \\ \gamma_{23} \\ \gamma_{31} \\ \gamma_{12} \end{Bmatrix} \quad (4.5)$$

where  $C_{ij}$  are the constants and  $[C]$  is the stiffness matrix.

#### 4.2.6 Engineering constants

The orthotropic material properties are defined by the nine material parameters. They are the elastic modulus in the three direction  $E_1, E_2, E_3$ , The poison ratio in the three planes  $\nu_{12}, \nu_{13}, \nu_{23}$  and the shear modulus in the three planes  $G_{12}, G_{13}, G_{23}$ . The elastic modulus  $E$  and Poisson's ratio  $\nu$  are measured from the tensile testing and the shear modulus  $G$  is measured from shear testing (Chawla, 1987).

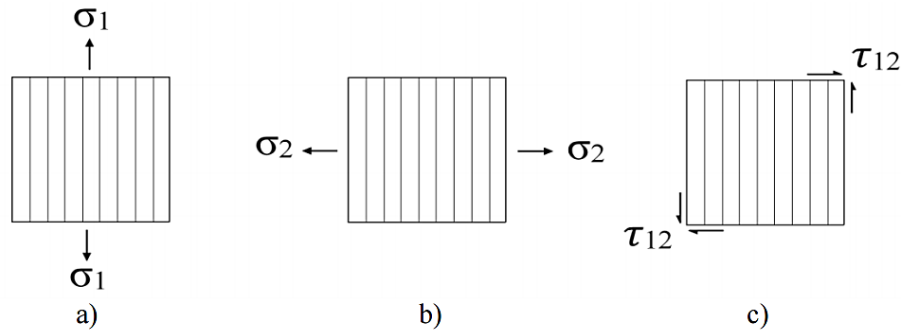


Figure 4.5 Simple stress states used for engineering parameters (Gibson, 1994)

The engineering parameters are defined using simple states of stress and are defined based on the Hooke's Law. For a uniaxial tensile test with an applied stress  $\sigma_1$  along the fibre direction as shown in Figure 4.3(a), all other stresses are assumed to be zero as observed experimentally (Gibson, 1994). For this stress state, following relations can be deduced:

$$\varepsilon_1 = \frac{\sigma_1}{E_1} \quad (4.6)$$

$$\varepsilon_2 = -\nu_{21}\varepsilon_1 = -\nu_{21} \frac{\sigma_1}{E_1} \quad (4.7)$$

$$\varepsilon_3 = -\nu_{13}\varepsilon_1 = -\nu_{13}\frac{\sigma_1}{E_1} \quad (4.8)$$

$$\gamma_{12} = \gamma_{23} = \gamma_{13} = 0 \quad (4.9)$$

For a similar test with a stress  $\sigma_2$  acting normal to the fibre direction as shown in Figure 4.3(b) and all other stresses are assumed zero as observed experimentally (Gibson, 1994). For this stress state, following relations can be deduced:

$$\varepsilon_2 = \frac{\sigma_2}{E_2} \quad (4.10)$$

$$\varepsilon_1 = -\nu_{21}\varepsilon_2 = -\nu_{21}\frac{\sigma_2}{E_2} \quad (4.11)$$

$$\varepsilon_3 = -\nu_{23}\varepsilon_1 = -\nu_{23}\frac{\sigma_2}{E_2} \quad (4.12)$$

$$\gamma_{12} = \gamma_{23} = \gamma_{13} = 0 \quad (4.13)$$

For a pure shear test, where  $\tau_{12}$  is applied as shown in the Figure 4.3(c). All other stresses are assumed zero as observed experimentally. For this stress state, following relations can be deduced (Gibson, 1994):

$$\gamma_{12} = \frac{\tau_{12}}{G_{12}} \quad (4.14)$$

$$\varepsilon_1 = \varepsilon_2 = \varepsilon_3 = \gamma_{13} = \gamma_{23} = 0 \quad (4.15)$$

Based on the Equations 4.6 to 4.15 the compliance matrix  $[S]$  can be expressed as Equation 4.16. The compliance matrix  $[S]$  describes the relationship between stress and strain for a general orthotropic material.

$$[S] = \begin{bmatrix} \frac{1}{E_1} & -\frac{\nu_{21}}{E_2} & -\frac{\nu_{31}}{E_3} & 0 & 0 & 0 \\ -\frac{\nu_{12}}{E_1} & \frac{1}{E_2} & -\frac{\nu_{31}}{E_3} & 0 & 0 & 0 \\ -\frac{\nu_{31}}{E_1} & -\frac{\nu_{23}}{E_2} & \frac{1}{E_3} & 0 & 0 & 0 \\ 0 & 0 & 0 & \frac{1}{G_{23}} & 0 & 0 \\ 0 & 0 & 0 & 0 & \frac{1}{G_{31}} & 0 \\ 0 & 0 & 0 & 0 & 0 & \frac{1}{G_{12}} \end{bmatrix} \quad (4.16)$$

$$\sigma = [S]^{-1}\varepsilon \quad (4.17)$$

$$\sigma = [C]\varepsilon \quad (4.18)$$

where,

$$[C] = \begin{bmatrix} \frac{1 - \nu_{23}\nu_{32}}{E_2E_3\Delta} & \frac{\nu_{12} + \nu_{32}\nu_{13}}{E_1E_3\Delta} & \frac{\nu_{13} + \nu_{12}\nu_{23}}{E_1E_2\Delta} & 0 & 0 & 0 \\ \frac{\nu_{12} + \nu_{32}\nu_{13}}{E_1E_3\Delta} & \frac{1 - \nu_{13}\nu_{31}}{E_1E_3\Delta} & \frac{\nu_{23} + \nu_{21}\nu_{13}}{E_1E_2\Delta} & 0 & 0 & 0 \\ \frac{\nu_{13} + \nu_{12}\nu_{23}}{E_1E_2\Delta} & \frac{\nu_{23} + \nu_{21}\nu_{13}}{E_1E_2\Delta} & \frac{1 - \nu_{12}\nu_{21}}{E_1E_2\Delta} & 0 & 0 & 0 \\ 0 & 0 & 0 & G_{23} & 0 & 0 \\ 0 & 0 & 0 & 0 & G_{31} & 0 \\ 0 & 0 & 0 & 0 & 0 & G_{12} \end{bmatrix} \quad (4.19)$$

and

$$\Delta = \frac{1 - \nu_{12}\nu_{21} - \nu_{23}\nu_{32} - \nu_{31}\nu_{13} - 2\nu_{21}\nu_{32}\nu_{13}}{E_1E_3E_3} \quad (4.20)$$

### 4.3 Finite element analysis

According to DNV-OS-C501 (2010), the selection of finite elements package shall be based on:

- Analysis option required
- Software availability
- Validated software for intended analysis
- Necessary model size

ANSYS Mechanical fulfils the requirements listed above and it is used for GRP modelling in the present study.

#### 4.4 Material model

GRP covers are specified with the following orthotropic material properties; see Table 4.1.

**Table 4.1 Orthotropic material properties**

Parameters		CSM	Uniaxial ply
Density ( $kg/m^3$ )		1460	2000
Young's Modulus	$E1$ (MPa)	15000	40000
	$E2$ (MPa)	15000	7000
	$E3$ (MPa)	1	700
Poisson's ratio	$V12$	0.3	0.3
	$V13$	0	0.3
	$V23$	0	0.3
Shear Modulus	$G12$ (MPa)	4000	4000
	$G31$ (MPa)	1	4000
	$G23$ (MPa)	1	4000
Strain Limits	Tension	$eXt$	0.014
		$yet$	0.014
	Compression	$eZt$	0.019
		$eYc$	0.019
Shear	$eSxy$	0.01	
Stress Limits	Tension	$Xt$ (MPa)	210
		$Yt$ (MPa)	210
		$Zt$ (MPa)	1000
	Compression	$Xc$ (MPa)	280
		$Yc$ (MPa)	280
		$Zc$ (MPa)	1000
	Shear	$Sxy$ (MPa)	50
		$Sxz$ (MPa)	50
		$Syz$ (MPa)	50



The directions  $X$ ,  $Y$  and  $Z$  are 1, 2 and 3 respectively defined in the present study. Poisson ratio and shear modulus along  $XY$  and  $XZ$  plane is assumed slightly less than the  $XZ$  plane based on the general judgement about GRP material. Similarly, the Young's modulus in  $Y$  and  $Z$  direction is also kept less than as it is in  $X$  direction to have realistic material properties of a common GRP material. General material properties are used in this study. These values are based on the previous experience with GRP and engineering judgement.

Conclusively, composite materials can have very specific directional properties. Therefore, material tests are required in order to get orthotropic GRP material properties.

#### 4.5 Failure criterion

An arbitrary failure criterion is defined since the scope of this document is to differentiate the behaviours of different geometries. Individual fibre failure in GRP is considered negligible, as it will not cause the total collapse. The material model selected in the present study does not permit fibre level failure criterion. Therefore, maximum equivalent stress against a selected number serves as the failure criterion. The geometry optimization study between different GRP cover geometries is independent of the failure criterion because a relative study is carried out between the three cover geometries.

It was necessary to mention the failure criterion to help better understand the GRP behaviour and follow conventional design method along with the comparative study. Secondly, impact-bearing capacity is calculated based on the defined failure criterion.

Failure criterion adopted for the present study:

$$\text{Max Equivalent Stress} < 300 \text{ MPa}$$

Max equivalent stress is the Von Mises stress.

## 4.6 Load and resistance factors

Load and resistance factors are taken from DNV-OS-C501 (2013) and DNV-OS-H205 (2014). Similar to the failure criterion, the load factors do not influence the results underway in this study. This is because the load factors are same for all covers since it is assumed that the material, manufacturing process and manufacturer are the same for all the three geometries. Load factors changes for different fibre reinforcements, shape complexity, material, manufacturing process or a different supplier.

**Table 4.2 Load and resistance factors**

<b>Factor</b>	<b>Symbol</b>	<b>Value</b>	<b>Reference</b>
Combined load effect and Resistance Factor	$\gamma_{FM}$	1.7	(DNV-OS-C501, 2013) <sup>1)</sup> Sec 8 2.3.5
Resistance model factor	$\gamma_{RD}$	1.0	(DNV-OS-C501, 2013) Sec 6 4.2.1
Load model factor	$\gamma_{Sd}$	1.0	(DNV-OS-C501, 2013) <sup>2)</sup> Sec9 12.3.2
System factor	$\gamma_S$	1.0	(DNV-OS-C501, 2013) <sup>3)</sup> Sec 8 4.1.2
Partial factor for fatigue	$\gamma_{FAT}$	Not governing	(DNV-OS-C501, 2013) Sec 8.1.1
Consequence factor	$\gamma_c$	1.3	(DNV-OS-H205, 2014) Table 5.1
Load factor	$\gamma_F$	1.4	(DNV-OS-H205, 2014) Sec 5.1.2.3

**Notes:**

1. Safety class high, brittle properties
2. FEM used within constrains
3. Failure of one cover is independent of the system failure

$\gamma_{FM}$  is the partial load and resistance factor defined as  $\gamma_{FM} = \gamma_F \times \gamma_M$ . It is selected against different reliabilities. For the subsea cover, it is assumed that safety class is high and the coefficient of variation  $COV < 10\%$ . Where,  $COV$  is defined as the fraction of composite material that may have different material properties as compared to the set material properties. Most of the GRP manufacturers comply with  $COV < 10\%$ . The hand layup process of

manufacturing GRP with skilled labour has  $COV < 10\%$ . The vacuum infusion moulding process has  $COV < 5\%$ .

$\gamma_{RD}$  is the resistance model factor that can be set equal to  $1.0$  if the test results of material properties are reliable. It is assumed that the material properties are well defined by material tests thus  $\gamma_{RD} = 1.0$

$\gamma_{sd}$  is the load-model factor, which accounts for uncertainties of the structural analysis method being used to accurately describe and quantify the response of the structure. As the FEM, analysis is used within constraints then  $\gamma_{sd}$  can be set equal to  $1.0$ .

$\gamma_S$  is the system factor, which accounts for the uncertainty associated with assigning similar safety factors to the entire system. Depending on how the components are connected to form a system, the target probability of failure for individual components may need to be lower than the target probability of failure of the entire system.

For example, in the case of a pipeline system, the failure of one pipe component (i.e. plain pipe or end connector) is equivalent to the failure of the entire system. This is a series system. Consequently, the target safety of individual components should be higher than the target safety of the entire system in order to achieve the overall target safety. In order to consider this system-effect, a system-effect factor  $\gamma_S$  shall be introduced according to DNV-OS-C501 (2013). Since subsea cover is assumed as one unit without hatches or other accessories,  $\gamma_S = 1.0$ .

$\gamma_{FAT}$  is the partial factor for fatigue that is neglected since subsea cover is subject to negligible cyclic loading.  $\gamma_F$  is the load factor that accounts for unbalance or trim in the load since load cannot be uniformly distributed in all cases.

#### **4.6.1 Summary of load factors (resistance and load)**

Combined load and resistance factors are shown in the Table 4.3.

**Table 4.3 Load and resistance factors**

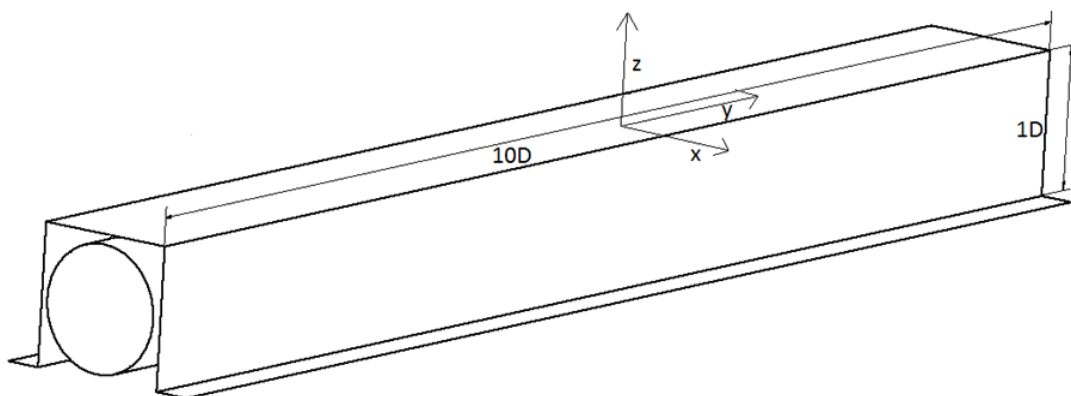
Load Case	Load Factor Considered	Value			Resistance Factor	Value		
		R	T	C		R	T	C
Trawlboard Friction	$\gamma_F^* \gamma_{sd}$	1.4	1.4	1.4	$\gamma_{FM}^* \gamma_{RD}^* \gamma_S / \gamma_F$	1.2	1.2	1.2
Trawlboard Overpull	$\gamma_F^* \gamma_{sd}$	1.4	1.4	1.4	$\gamma_{FM}^* \gamma_{RD}^* \gamma_S / \gamma_F$	1.2	1.2	1.2
Trawlboard Impact	$\gamma_F^* \gamma_{sd}$	1.4	1.4	1.4	$\gamma_{FM}^* \gamma_{RD}^* \gamma_S / \gamma_F$	1.2	1.2	1.2

**Notes:**

1. R= square cover
2. T= triangular cover
3. C= semi-circular cover

**4.6.2 Geometry of the GRP covers**

All the GRP cover geometries are defined by a variable  $D$ , where  $D$  is the height of the GRP cover (i.e square, triangular and semi-circular). Defining the dimensions with a variable helps in result comparison. For the fishing gear loads  $D = 1m$  is assumed which determines that the GRP cover is  $1m$  in height and  $10m$  in length. The cover geometries can be seen in the Figures 4.6 to 4.8. These geometries are further used in Chapter 5 for the drop-object impact analysis.

**Figure 4.6 The geometry of the square GRP cover**

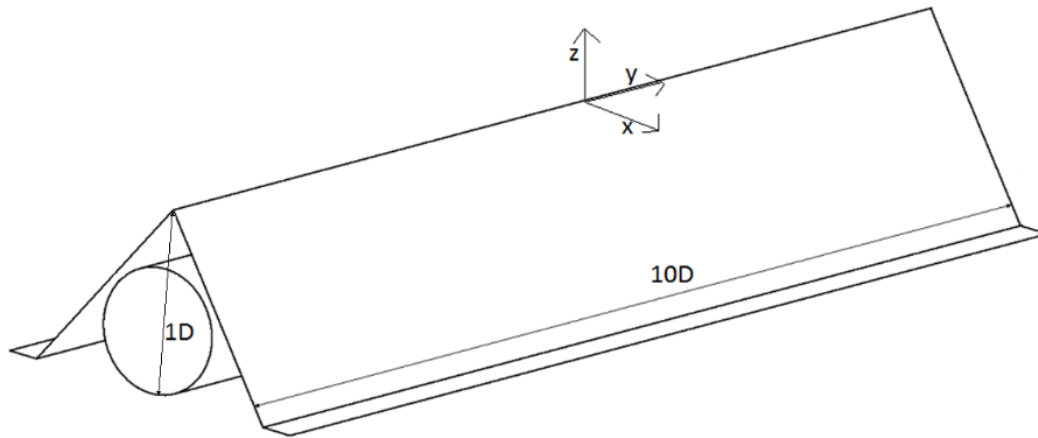


Figure 4.7 The geometry of the triangular GRP cover

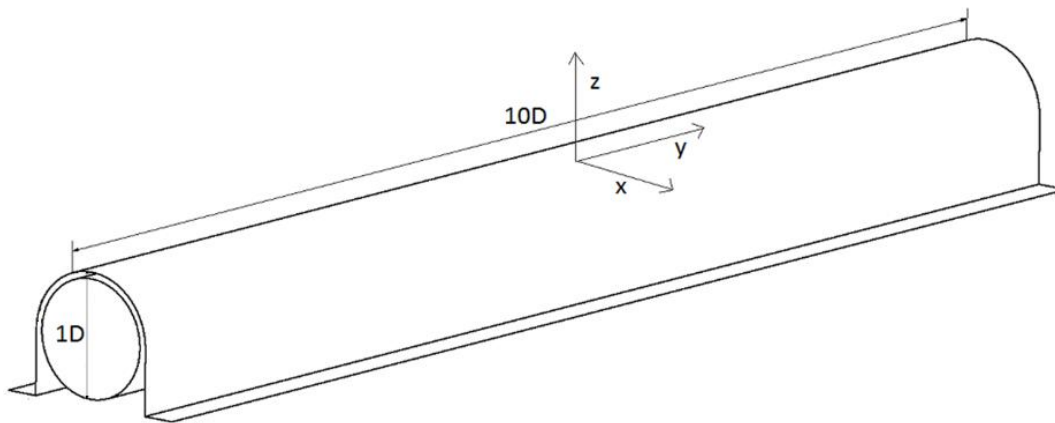
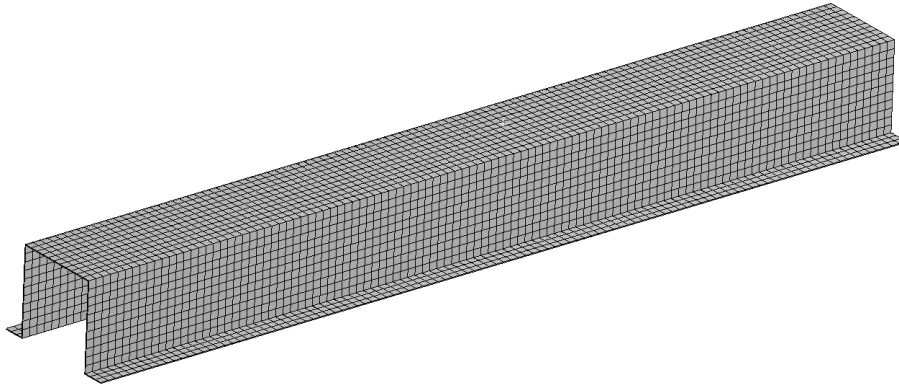


Figure 4.8 The geometry of the semi-circular GRP cover

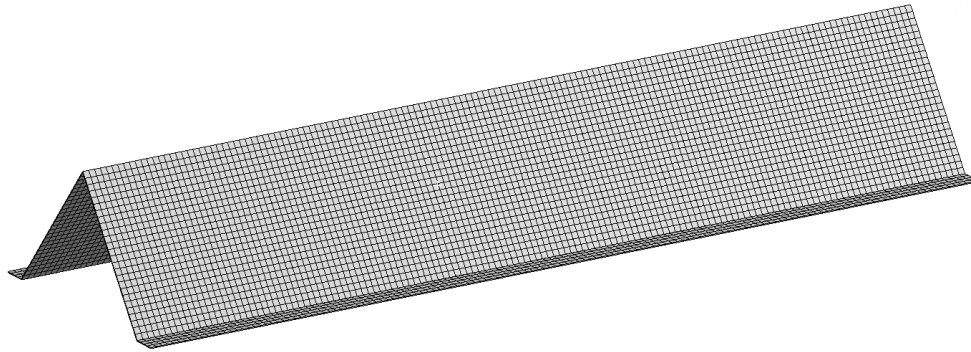
### 4.6.3 Mesh

ANSYS meshing tool is used to generate the mesh on the square, triangular and semi-circular covers. A uniform hex mesh is generated on the surface of these geometries and swept along the thickness. All covers are meshed using ANSYS SHELL181 elements. This is a first order element in which both multiple layers and anisotropy can be included. ANSYS adaptive mesh tool is used to carry grid independent study. The converged mesh is shown in Figure 4.9. Square cover gives the grid independent results for 6789 number of nodes and 6731 number of elements.



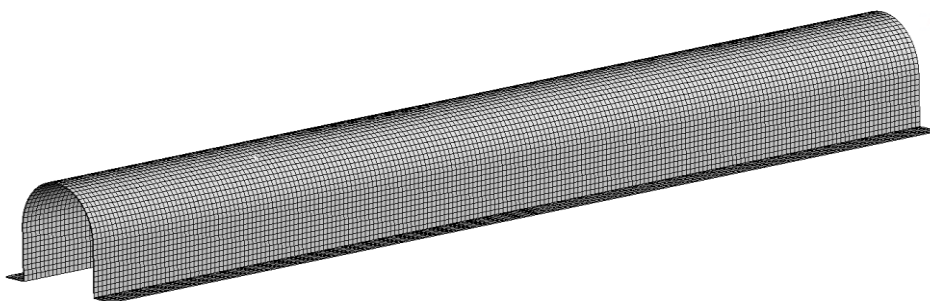
**Figure 4.9** The mesh used on square cover

Triangular cover gives the grid independent results for 8639 number of nodes and 8511 number of elements. The mesh is shown in Figure 4.10



**Figure 4.10** The mesh used on triangular cover

Semi-circular cover gives the grid independent results for 9977 number of nodes and 9712 number of elements. The mesh is shown in Figure 4.11



**Figure 4.11** The mesh used on semi-circular cover

## 4.7 Trawlnet friction loading

The trawlnet applies frictional force on the subsea cover while trawling as shown in the Figure 4.12. Trawlnet friction is modelled in ANSYS Mechanical and compared for the three covers in the present study. It is modelled as an in-plane force applied in the direction of trawlnet displacement.

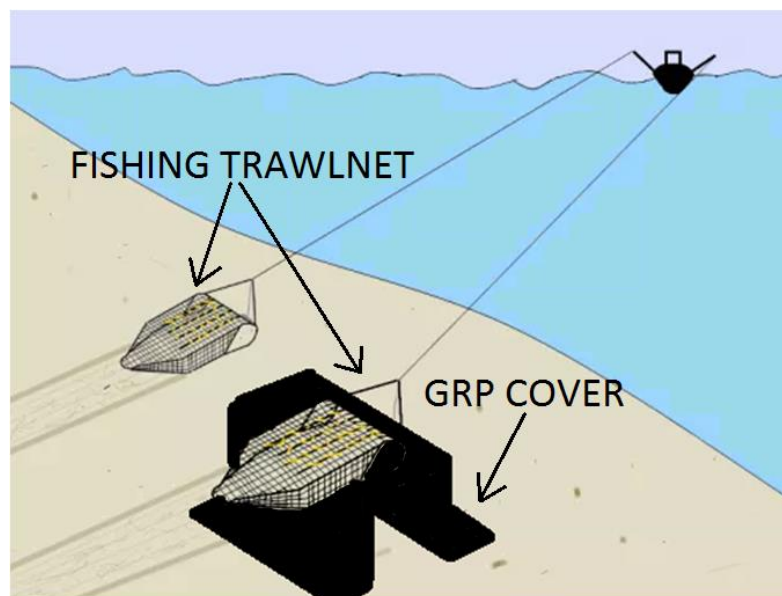
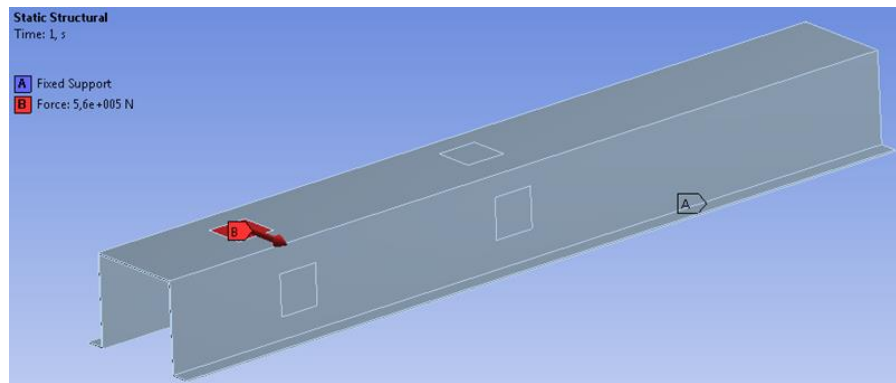


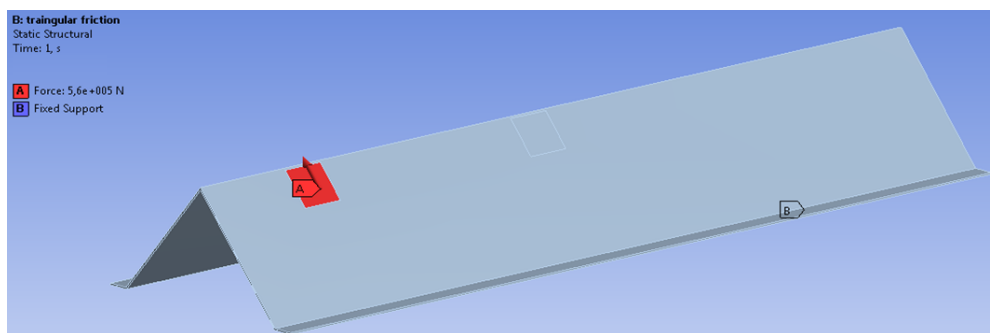
Figure 4.12 A typical trawlnet friction over GRP cover (figure developed for this thesis)

### 4.7.1 Loading and constraint for trawlnet friction loading

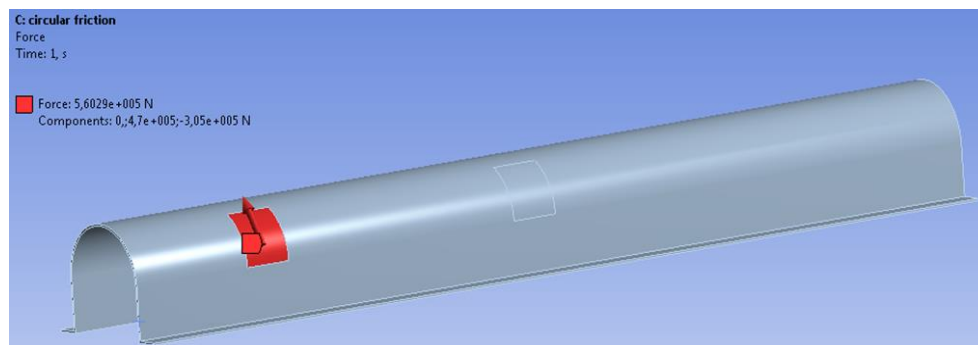
The trawlnet friction force taken from NORSOK U-002 (1998) is multiplied by the load factor listed in Table 4.3 ( $400 \text{ kN} \times 1.4 = 560 \text{ kN}$ ) and applied as an in-plane load in ANSYS Mechanical as shown in the Figure 4.13. In-plane force replicates frictional effect at the applied location. Frictional load is applied at different locations and the most critical location are displayed while the remaining results are shown in Appendix C. Force is applied on an area of  $0.5 \text{ m} \times 0.5 \text{ m}$  to model trawling friction area while the mudmat is applied with a fixed constraint. The load and constraint shown in the Figures 4.13 to 4.15 are the loading cases that gives the highest stress in the respective GRP covers.



**Figure 4.13** Load and constraint for trawlnet friction loading on square cover



**Figure 4.14** Load and constraint for trawlnet friction loading on triangular cover



**Figure 4.15** Load and constraint for trawlnet friction loading on semi-circular cover

The in-plane force gives displacement to each node in a particular direction within the plane. This is possible for planar geometries like square and triangular cover geometries. However, it is not possible for the semi-circular geometry cover. For the semi-circular geometry cover, in-plane force is approximated as a tangential force which may slightly differ from the exact in-plane results.



## 4.7.2 Results of trawlnet friction loading

The results giving highest equivalent stress are shown in Figures 4.16 to 4.18. In the Figure 4.16, the maximum stress is on the vertical walls close to the mud mats. In reality, the stress concentration will be at the hinge location between the vertical wall and the mudmat. The minor offset of the stress location is because that the mudmat has fixed constraint.

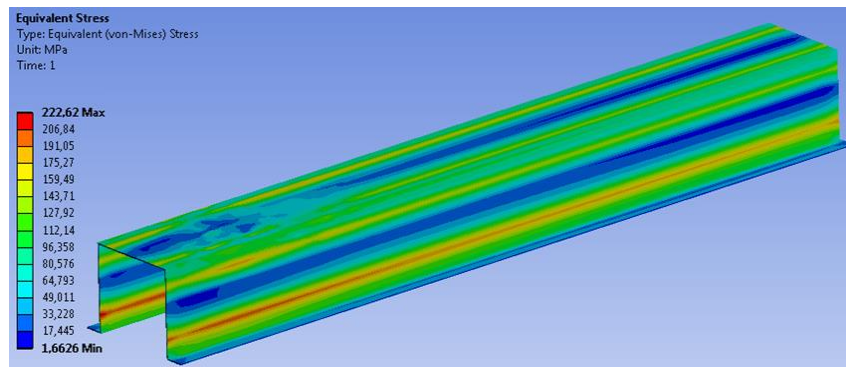


Figure 4.16 Equivalent stress for trawlnet friction loading on square cover

Triangular cover has much lower stress for the frictional load as compared to square and semi-circular covers because of the sliding effect in the geometry. Due to this effect, stress is relatively lower than square and semi-circular cover geometries. This makes triangular geometry suitable for frictional loads.

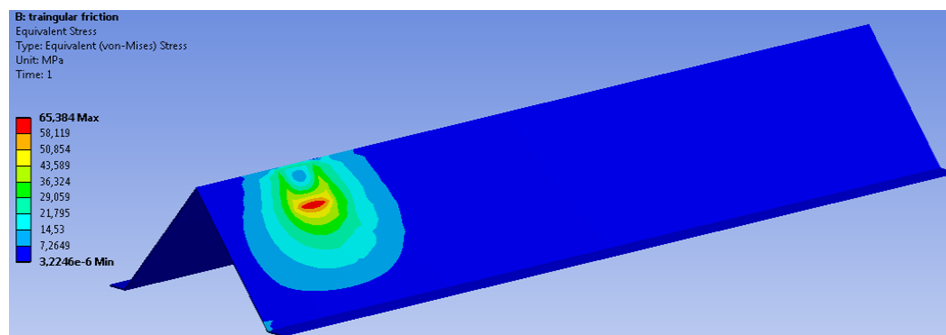


Figure 4.17 Equivalent stress for trawlnet friction loading on triangular cover

The maximum stress shown in the colour code bar is very high as compared to the stress shown in the probes in Figure 4.18. It can be seen in the Figure 4.18 that negligible area on the geometry has yellow or red colour. The stress in this region is less than  $100\text{ MPa}$ .

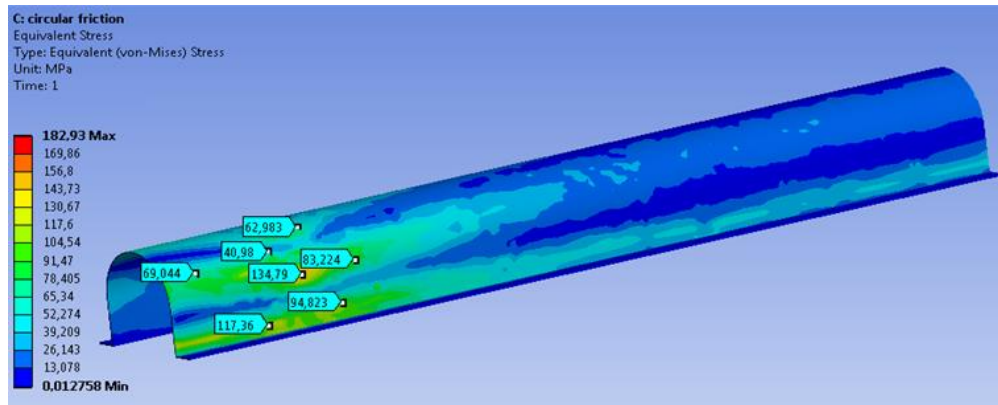





Figure 4.18 Equivalent stress, trawl net friction loading on semi-circular cover

### 4.7.3 Results discussion of trawl net friction loading

To understand the material efficiency and geometry comparison, a non-dimensional study is carried out. Non-dimensional comparison gives a better illustration of the results. Stress of each cross-section is normalized by the maximum stress in all the cross-sections. Similarly, volume of each cross-section is normalized by the maximum volume in all the cross-sections. Normalized stress and volume are added together to get the combined results. The lowest value of this combine results depicts the best cover among the investigated cover geometries.

Triangular cover has the minimal effect from the trawlboard friction force and contrarily it is the least material efficient cover. Semi-circular cover appears to be the best trade-off between stress and material volume. The corresponding stress is reasonably below failure criterion and has  $18\%$  less material volume to triangular cover.

**Table 4.4 Summary of equivalent stress for trawl net friction loading**

Shape	Max Equivalent Stress (S)	Material Volume (V)	Normalized Results $(\frac{S}{S_{max}} + \frac{V}{V_{max}})$
Square 	222 MPa	0.78 m <sup>3</sup>	1.98
Triangular 	65 MPa	0.80 m <sup>3</sup>	1.29
Semi-circular 	100 MPa	0.66 m <sup>3</sup>	1.28

**Notes:**

1.  $S_{max}$  is the maximum stress among all the cross-sections i.e. 222 MPa
2.  $V_{max}$  is the maximum volume among all cross-sections i.e. 0.8 m<sup>3</sup>

The results listed in Table 4.4 show the geometry behaviour of GRP cover against frictional loads from fishing activities. Besides the force bearing capacity and the material consumption, other factors have their own importance as well. Manufacturability is one of the prime GRP cover geometry selection criterion. Thus, the selection of the cover geometries is not just restricted to the load bearing capacity or less material consumption for manufacturing alone, it also depends on many other considerations as well.

Although the methodology is simple, it is a useful tool as a first approximation to understand the behaviour of trawlboard friction on subsea protection cover geometries.

#### 4.8 Trawlboard overpull loading

The trawlboard overpull is modelled in ANSYS Mechanical for the three cover geometries as an applied force normal to the plane with a fixed mud mat. These applied loads and constraints create an overpull effect on the GRP cover.

#### 4.8.1 Loading and constraint of trawlboard overpull loading

Trawlboard overpull load value taken from NORSOK U-002 (1998) is multiplied by load factor mentioned in the Table 4.3 ( $300 \text{ kN} \times 1.4 = 420 \text{ kN}$ ) and applied normal to the side walls as shown in the Figures 4.20 to 4.22. Overpull load is applied at different locations of the cover and locations giving the severest results are shown. Remaining results are shown in Appendix C. Overpull load is applied on an area of  $0.96 \text{ m} \times 0.96 \text{ m}$  (refer to Figure 4.19) to model trawling overpull area. The mud mat is applied with a fixed constraint.

It is assumed that trawlboard has an area of  $0.5 \text{ m} \times 0.5 \text{ m}$ , which is the minimum area among commonly used trawlboards according to Trawlworks, Inc (2015). The friction angle between the rocks and GRP is assumed to be  $42^\circ$ .

It is assumed that rock-berm thickness is  $0.25 \text{ m}$  at the location where trawlboard hits rock-berm. Using trigonometry with friction angle of  $42^\circ$ , area on the GRP is calculated. The overpull area on GRP where the force will act comes out to be  $0.96 \text{ m} \times 0.96 \text{ m}$ .

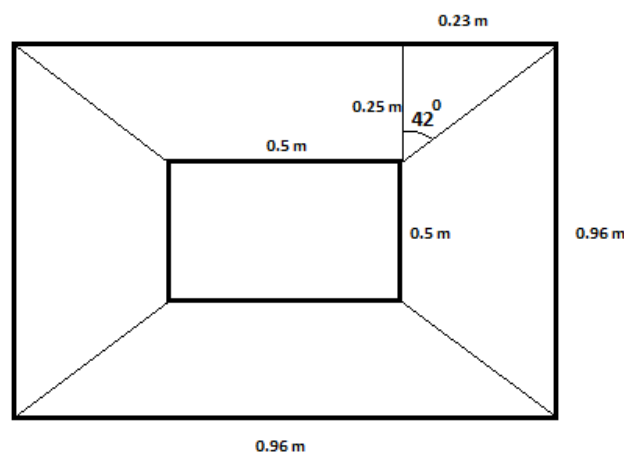


Figure 4.19 Load distribution of trawlboard overpull on a GRP cover

The load from the trawlboard is applied as a force normal to the plane. The area on the plane is taken as equivalent area under the force through the rock-berm. For square cover, the force from the trawlboard overpull is shown as B in the Figure 4.20.

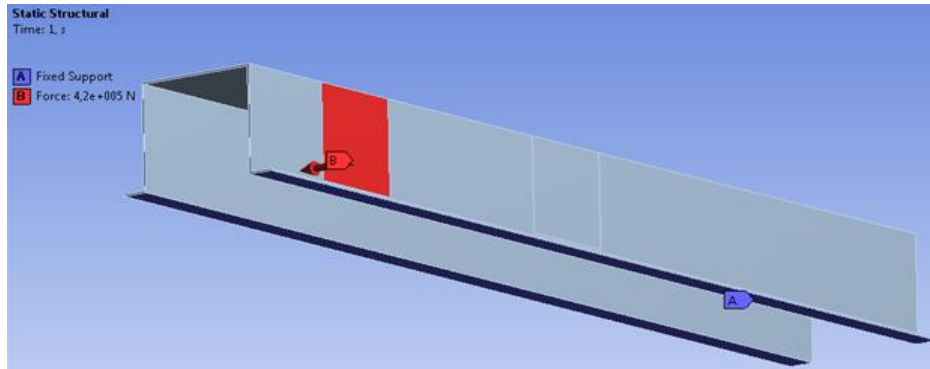


Figure 4.20 Load and constraint of trawlboard overpull on a square cover

For triangular cover, the force from the trawlboard overpull is shown as B in the Figure 4.21.

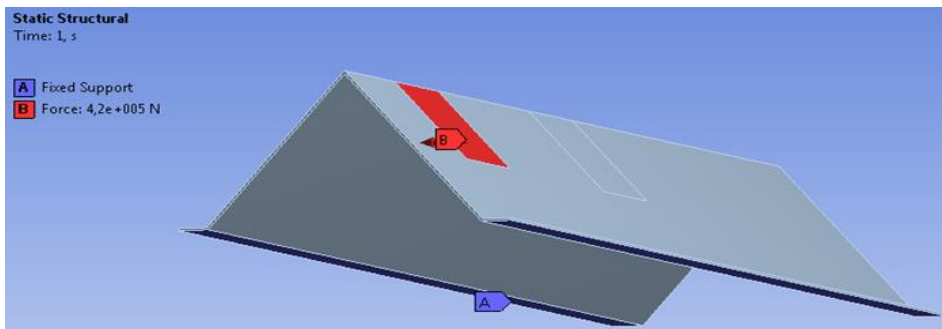


Figure 4.21 Load and constraint of trawlboard overpull on triangular cover

For semi-circular cover, the force from the trawlboard overpull is as shown in Figure 4.22.

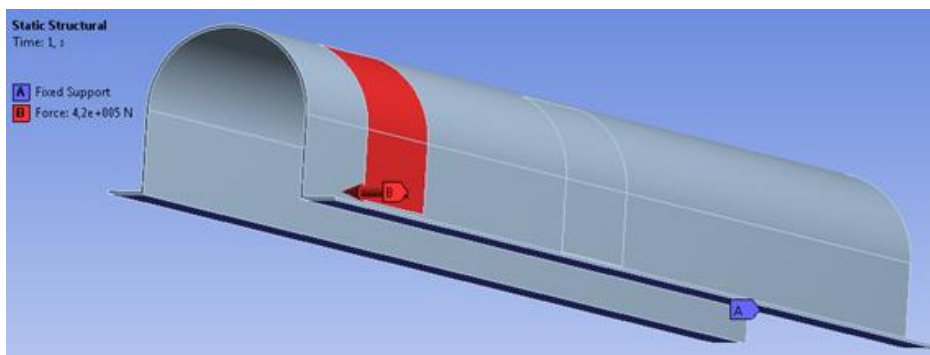


Figure 4.22 Load and constraint of trawlboard overpull on a semi-circular cover

#### 4.8.2 Results, trawlboard overpull

The results giving the highest equivalent stress are shown in Figures 4.23 to 4.25. For the square cover, stress concentration lies in the centre of the loading area where a large magnitude of stress is observed. Large stress exists only on the location where the force is applied. There are stresses at other locations close to hinges as well but have smaller magnitudes. The results are not symmetrical because of the orthotropic material properties of the GRP material.

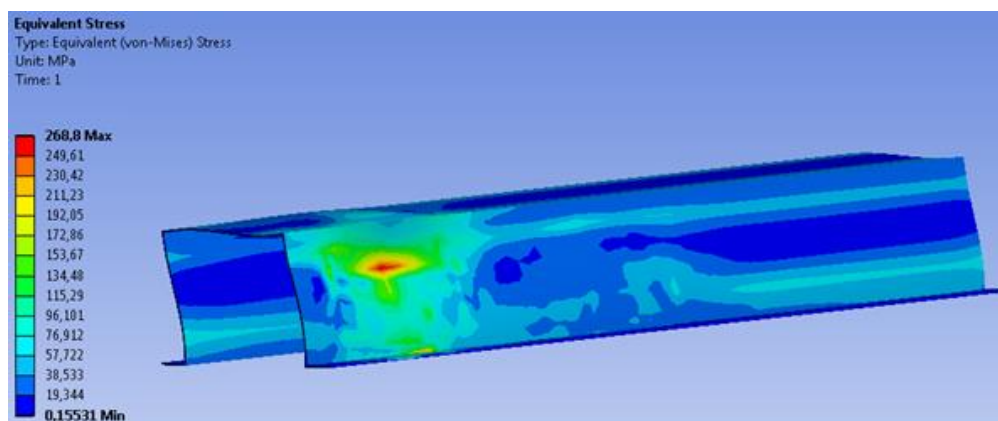


Figure 4.23 Equivalent stress for trawlboard overpull on square cover

The triangular cross-section has the stress, much higher than the square cross-section based on the reason that the face width is larger than that of the square cross-section as shown in Figure 4.24. Horizontal stiffeners can be used on the triangular cover to minimize the stress concentration. It is a common practice in GRP material to use stiffeners. Stiffeners help distributing the stress over a larger area.

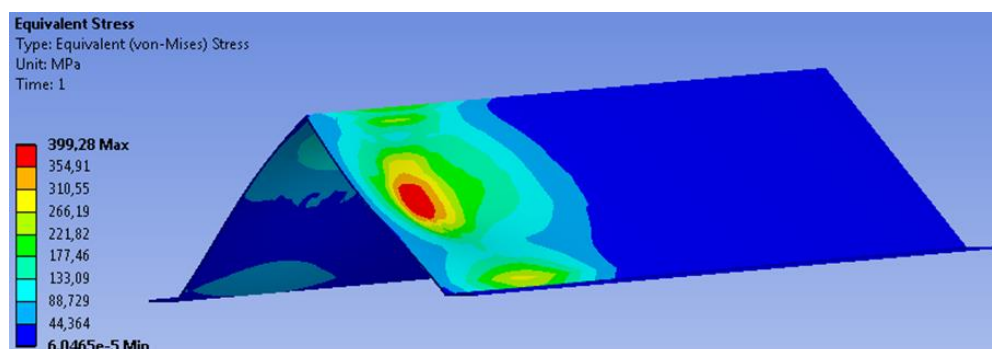


Figure 4.24 Equivalent stress of trawlboard overpull on triangular cover

Figure 4.25 shows the stress concentration on the semi-circular cover. It is observed that insignificant area has yellow region. The stress concentrations in this region is neglected. The maximum equivalent stress in the semi-circular cover for trawlboard overpull is  $160\text{ MPa}$ .

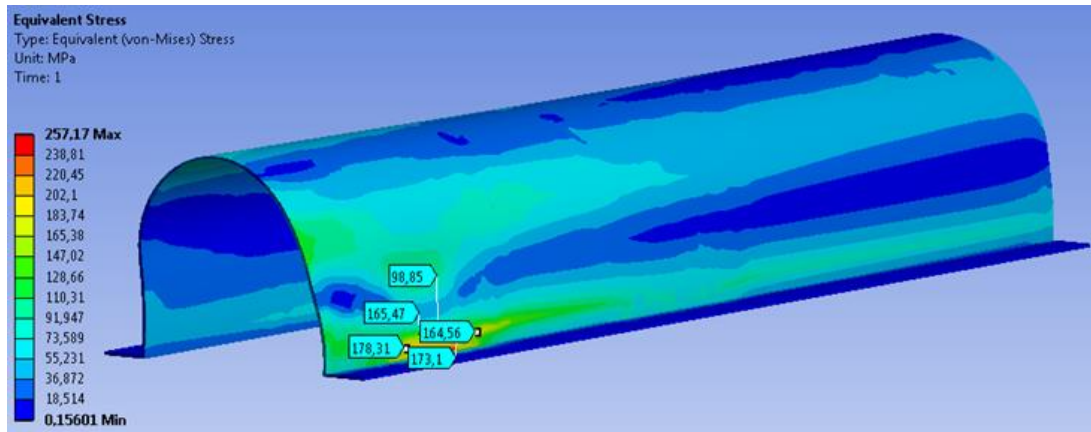





Figure 4.25 Equivalent stress of trawlboard overpull on semi-circular cover

### 4.8.3 Results discussion of trawlboard overpull loading

Semi-circular cover is the most efficient cover for trawlboard overpull loads among the three geometries analysed. Trawlboard overpull is the most severe loading condition among all fishing gear loads. In most of the cases, trawlboard overpull is the design governing loading condition. Semi-circular cover gives the best performance in bearing trawlboard overpull load based on the results summarized in Table 4.5. Therefore, it is recommended that the semi-circular cover must be employed in the fishing activity dominant areas.

**Table 4.5 Summary of equivalent stress for trawl net overpull**

Shape	Max Equivalent Stress (S)	Material Volume (V)	Normalized Results $(\frac{S}{S_{max}} + \frac{V}{V_{max}})$
Square 	269 MPa	0.78 m <sup>3</sup>	1.65
Triangular 	399 MPa	0.80 m <sup>3</sup>	2
Semi-circular 	160 MPa	0.66 m <sup>3</sup>	1.22

**Notes:**

1.  $S_{max}$  is the maximum stress among all the cross-sections i.e. 399 MPa
2.  $V_{max}$  is the maximum volume among all cross-sections i.e. 0.8 m<sup>3</sup>

#### 4.9 Conclusion

Square, triangular and semi-circular GRP covers are analysed for the fishing gear loads. Among the fishing activity loads, trawlboard friction and overpull loads are considered in the present study. For the trawlboard friction load, semi-circular cover has the highest load bearing capacity followed by triangular cover. Square cover has the least load bearing capacity for this load condition. For the trawlboard overpull load semi-circular cover has the highest load bearing capacity followed by square cover. Triangular cover has the least load bearing capacity for this loading. Therefore, it is concluded that the semi-circular cover is the most efficient GRP cover in bearing fishing activity loads.



## Chapter 5

### Assessment of impact damage caused by drop-objects on glass reinforced plastic (GRP) covers

#### 5.1 Introduction

Due to the ever-increasing utilization of energy globally, offshore exploration has become a domain of immense interest and is augmenting at a pace that is beyond measure. Setting up an offshore platform is not a plain-sailing task and is susceptible to critical accidents such as heavy object descent into the sea. As a result, such mishaps are the foremost reason of momentous damage to the underwater pipeline networks and risers. Not only this, the ruptured subsea pipelines and risers might give rise to containment failure and leakage of hydrocarbon into the seawater, a massive environmental hazard and threat. Data from report on offshore pipeline catastrophes of the UK Health and Safety Executive PARLOC:2001 (HSE, 2003) and the PRC, International American Gas Association (IAGA) (1999, 2000) specified that about 47% of pipeline failures were caused by external impact. Drop-objects from fishing and offshore oil and gas activities possess potential threat to the pipelines (Muhlbauer, 2004). The offshore industries are operating quantitative risk assessment (QRA) in official safety assessments to mitigate risks and upsurge protection in offshore assets.

GRP subsea protection covers are used to protect offshore oil and gas pipelines from the drop-objects. Impact energies of different offshore drop-objects are calculated. This analysis is carried out by subjectively selecting various offshore drop-objects such as offshore equipment and fishing gear. Square, triangular and semi-circular geometries are the most commonly used geometries for the design of a GRP cover. Drop-object impact absorption capacity of these geometries are calculated by performing finite element analysis. The drop-object impact absorption capacity of the three geometries are computed and compared with each other. GRP covers are used because of their light weight and low cost. To our knowledge, there is no available published literature on the drop-object impact-bearing capacity of different protection cover geometries. This chapter will cover two parts:

- Impact energy calculation of different subjectively selected offshore drop-objects
- Comparison of drop-object impact-bearing capacity of GRP covers with square, triangular and semi-circular geometries

Drop-object is any object that has the potential to cause subsea equipment damage or failure by falling from its previous static position under its own weight. The object could either be a machinery component, broken part of equipment, a loose mechanical part of machinery or in some cases a part of big cargo being transported. For example, Shell UK Exploration and Production operates five concrete gravity structures in North Sea. During the 33 years of platform life, 4 drop-objects incidents were reported. One incident was falling of *21.9 tonnes* heavy crane assembly from the deck (Wimpey Laboratories, 1989).

Out of a large possible list of drop-objects, several are subjectively selected.

## 5.2 *Impact energy*

When a mass falls under the influence of gravitational force, it accelerates until it reaches its terminal velocity and hits some other matter. In order for that matter to remain in equilibrium, it has to absorb the energy carried by that object. The energy absorbed by the matter is called impact energy (Institution of Mechanical Engineers, 1998). The impact energy is equal to the kinetic energy of the falling mass:

$$I = \frac{mv^2}{2} \quad (5.1)$$

where,

- $I$  is the total impact energy
- $m$  is the mass of the dropped object
- $v$  is the velocity of the dropped object

For the calculation of the falling velocity of the objects, the drop-objects are considered free fall i.e., the drop objects at their terminal velocities. It should be noted that dynamic objects which hit under the influence of some initial driving force are not considered as drop-objects e.g. remotely operated vehicles (ROV) and autonomous under water vehicles (AUV).

### 5.2.1 **Terminal velocity**

Falling velocity of the drop-object achieves the terminal velocity when the drag force on the drop-object by seawater is equal to the hydrodynamic weight of the falling object. The terminal velocity is defined as the maximum attainable velocity by a body of specific mass and shape,

falling through a fluid of specific density according to Cengel & Cimbala (2010). All calculations in this chapter are carried out at the terminal velocity of different drop-objects.

To calculate the terminal velocity, the following relation is used based on the definition by Cengel and Cimbala (2010).

$$mg - b = \frac{\rho C_D A v^2}{2} \quad (5.2)$$

$$v = \sqrt{\frac{2(mg-b)}{\rho C_D A}} \quad (5.3)$$

where,

$v$  is the terminal velocity of the drop-object

$m$  is the mass of the drop-object

$b$  is the buoyancy force experienced by the drop-object

$C_D$  is the drag coefficient of the drop-object

$A$  is the projected area of the drop-object

$\rho$  is the density of sea water =  $1025 \text{ kg/m}^3$

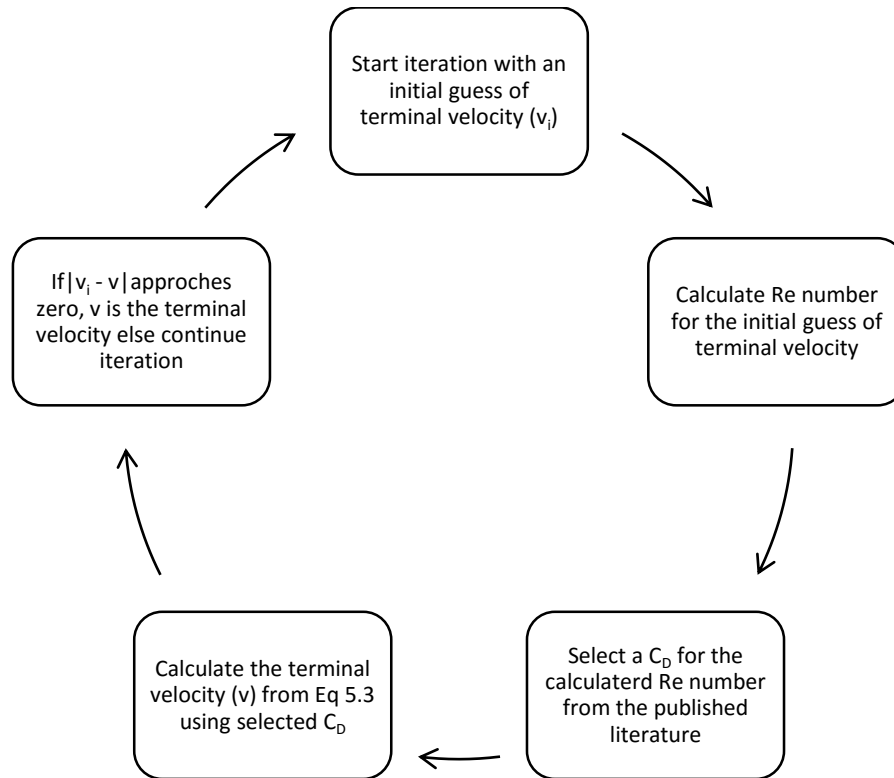
$g$  is the gravitational acceleration =  $9.81 \text{ m/s}^2$

### 5.2.2 Selection of drag coefficient

In order to calculate the terminal velocity, the drag coefficient of each drop-object was necessary. The geometries of the offshore drop-objects, are complex in shape and require experiments or CFD simulations to calculate drag coefficients (Liu et al., 2011). Since there are no available data of drag coefficients for offshore equipment in open literature, drag coefficients approximation with known geometries is used.

Drag coefficients of standard geometries such as spherical and cubical shapes were available at different Reynold numbers rages. The drag coefficients of the selected drop-objects were approximated by comparing the drop-object geometry with the standard geometries. A conservative approach was adopted in comparison to cover up the possible short comings in the approximation of drag coefficient. Although the actual drag coefficients of the equipment may differ from the approximated value, this will help getting a general picture of the impact energies. Secondly, the geometries of the offshore equipment varies from one supplier to another. Thus, a generalized shape will give a better understanding of the overall behaviour of a particular drop-object. A detailed study is required to get better understanding about the drop-

objects but the present study will be able to serve as a first engineering judgement for the subsea cover designer. To select the drag coefficient from the published data, Reynolds number is required. Further drag coefficient is required to calculate terminal velocity. However, Reynolds number is a function of shape and velocity of the object. Consequently, in order to have a converged solution for drag coefficient, an iterative approach is used.



**Figure 5.1 Terminal velocity calculation algorithm**

Figure 5.1 shows an engineering approach to determine the terminal velocity. An initial guess is made for the terminal velocity. Then the Reynolds number is calculated for the guessed terminal velocity. For the calculated Reynolds number, drag coefficient is selected from the Sadraey (2009). Finally, for the selected drag coefficient, terminal velocity is calculated and compared with the initial guess. This process is repeated until the terminal velocity is converged.

### 5.2.3 Calculation of impact energies

The calculation of impact energy of drop-objects requires the identification of masses and volumes of selected drop-objects. These numbers are selected by going through the catalogues

of equipment by various suppliers and taking an average number. Consider the following example:

It is observed that the mass of tree panels varies from 2000 kg to 2400 kg in different catalogues. 2200 kg is the mean mass and thus used as a reasonable approximation for the calculation purpose. The volume of the tree panel is approximately 1 m<sup>3</sup>. The shorter face dimensions are 2m × 1m which is taken as the impact face. The geometry is approximated with the cube to select the drag coefficient.

Mass = 2200 kg

Weight = 22 kN

Volume = 1 m<sup>3</sup>

Impact Area = 2 m<sup>2</sup>

Buoyancy Force = Sea water density x Volume x Gravitational Acceleration = 10 kN

#### 5.2.4 Converged solution

Initial guess of terminal velocity = 3.34 m/s

Reynolds number =  $7.95 \times 10^6$

Drag coefficient = 1.05

$$\text{Terminal velocity} = v = \sqrt{\frac{2(mg-b)}{\rho C_d A}} = 3.34 \text{ m/s}$$

The calculated terminal velocity is equal to the initial guess made for the terminal velocity. Thus, the terminal velocity has converged and can be further used to calculate impact energy.

$$\text{Impact energy} = \frac{mv^2}{2} = 12 \text{ kJ}$$

In the similar methodology, impact energies of the selected offshore drop-objects are summarized in Table 5.2 (shown in the end of Section 5.2.5). The impact energies of the drop objects range from 4 kJ for a small tool to 2700 kJ for a large offshore module.

### 5.2.5 Discussion

According to NORSOK U-002 (1998), protection covers should have the capability of absorbing  $20\text{ kJ}$  impact energy for drop-objects having diameter of  $0.5\text{ m}$  and  $5\text{ kJ}$  impact energy for drop-objects with diameter  $0.1\text{ m}$  (see Table 5.1).

The drop-objects impact energies from the fishing activities listed in Table 5.2 are less than  $20\text{ kJ}$ , which is in accordance with NORSOK U-002 (1998). On the other hand, the most probable drop-objects considered from oil and gas activities have impact energy less than  $20\text{ kJ}$  while the others have higher than  $20\text{ kJ}$ . Trawlboard has a diameter of approximately  $0.5\text{ m}$  and its calculated impact energy is  $10\text{ kJ}$  (see Table 5.2) which is within the limiting criterion of NORSOK U-002 (1998). To get a picture of the drop-object impact energies, approximated shapes are considered. The results summarized in Table 5.2 have also been compared with the online available results by DROPS (2010). The difference between impact energy for the present study and DROPS (2010) is less than  $20\%$  for all the compared objects. This difference is considered acceptable because no accurate data of drop objects mass and drag coefficient was available and a subjective study is carried out. Secondly, the difference of impact energy among the compared results also exist due to the large variation of geometries and masses of these offshore equipment from one supplier to another. The offshore equipment data in the present study is generated by averaging masses and dimensions of the selected drop equipment available in different catalogues from different suppliers. The hydrodynamic force coefficients have also been approximated from the published results. The purpose of this study is to get an idea of the impact energies carried by the offshore drop-objects and this study satisfies the need.

Although no experimental validation is available, the simple technique and the results comparable to DROPS members (2010) and NORSOK U-002 (1998) gives a scientific validation of the present study.

**Table 5.1 Drop-object impact energy taken from (NORSOK U-002, 1998)**

<b>Impact energy</b>	<b>Impact area</b>	<b>Object diameter</b>
<i>20 kJ</i>	<i>Point load</i>	<i>0.5 m</i>
<i>5 kJ</i>	<i>Point load</i>	<i>0.1 m</i>

Table 5.2 Impact energy carried by drop-objects

Oil & Gas Activities											
Object	Mass (kg)	Weight (kN)	Volume (m <sup>3</sup> )	Buoyancy Force (kN)	Drag Coefficient	Impact Area (m <sup>2</sup> )	Reynolds Number x 10 <sup>6</sup>	Converged Terminal Velocity (m/s)	Present Study Impact Energy (kJ)	DROPS (2010) Impact Energy (kJ)	Percentage Difference (Present Study and DROPS (2010))
Subsea Tree	45000	441	8	80.4	1.05	6	508.2	11	2722	2880	5
Spool Tree	12000	118	5	50.2	0.8	3	210	10	600	650	8
Tubing Hanger	2500	25	1	10.0	0.7	1	25.2	6	45	45	0
Umbilical Reeler	10000	98	3	30.1	0.47	2	89.6	8	320	326	2
Tree Panel	2500	22	1	10.0	1.05	2	50.4	6	45	49	8
Glycol Tank	3600	35	1	10.0	0.7	1	34.3	6	64	65	2
Air Compressor	8000	59	2	20.1	0.8	1	34.3	7	196	192	2
Holding Tank	2500	58	2	20.1	0.8	1	17.5	5	31	36	14
Surge Tank	25000	245	5	50.2	0.6	3	170.1	9	1012	860	18
Gravel Infuser	1800	18	1	10.0	0.8	1	17.5	6	32	36	11
Protection Frame	3000	29	1	10.0	0.7	1	25.2	6	54	45	20
9,1/2"Drill Collar	3500	34	0.6	6.0	0.5	0.2	6.86	6	62	63	2
Small Tools	150	1	0.08	0.8	0.3	0.1	3.43	7	4	NA	NA
Fishing Activities											
Trawl Board	5000	49	3	30.1	2.2	3	8.4	2	10	NA	NA
Trawlnet Loaded	1500	15	1	10.0	0.5	1	11.2	4	12	NA	NA
Trawling Rope Coil	1000	10	0.5	5.0	0.5	1	11.2	4	8	NA	NA
Net Spreader Beam	5000	49	3	30.1	2.2	3	8.4	2	10	NA	NA
Shrimp Pass grid	4000	39	3	30.1	1.2	3	8.4	2	8	NA	NA

Notes: NA in the table is placed for data not available

### 5.3 Impact absorption capacity

The geometries, material model, failure criterion and mesh mentioned for the square, triangular and semi-circular covers in Chapter 4 are used for the calculation of impact-bearing capacity of drop-objects. Details of the geometries of these covers can be seen in Appendix A.

#### 5.3.1 Drop-object impact modelling

The square, triangular and semi-circular cover geometries are analysed for the maximum impact-bearing capacity in ANSYS Mechanical. Force is applied in vertically downward direction incrementally at different nodes on each geometry and the deformation is recorded until failure is reached. The product of force and deformation at the location just before the failure gives the maximum impact absorption capacity.

Fixed boundary condition is used on the mud mat of GRP cover as the cover is rock dumped on mud mats. The force is applied in vertical downward direction to model the force from drop-object.

#### 5.3.2 Results discussion

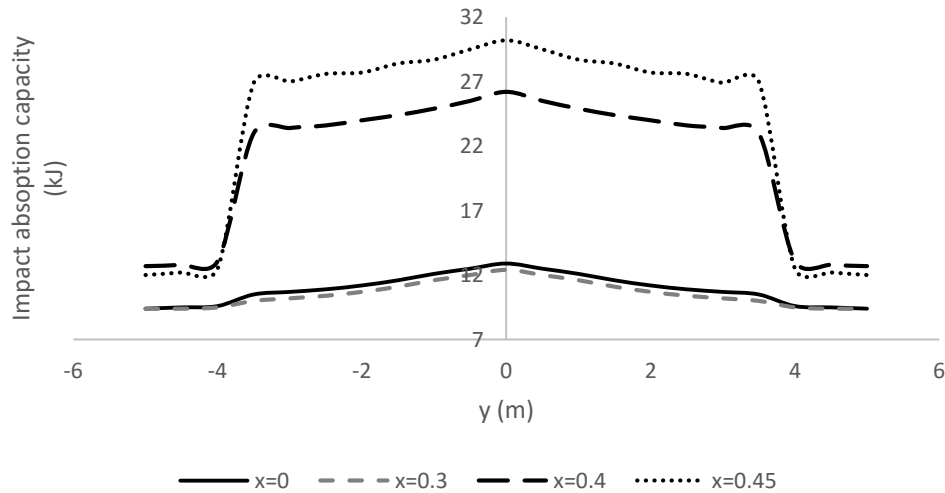
Impact absorption capacity of the three cover geometries are different at different locations. It is observed that the impact absorption capacity is greater near the sidewalls and less in the centre. This is because the sidewalls also contribute in absorbing the impact load. The impact absorption capacity is also less on the open ends.

#### 5.3.3 Square cover

Impact absorption capacity is significantly different at different locations on the square cover. The geometry of the square GRP cover can be seen in Appendix A where  $x$  is the distance along the length of the cover and  $y$  is the distance along the width of the cover. Figure 5.2 shows graphically, the results of impact absorption capacity for different values of  $x$ . The cover is symmetric; therefore, the results are symmetric along  $y$ -axis. It is observed that the impact absorption capacity remains close to  $11kJ$  in the centre of the face while on the outer edges it



is  $28 \text{ kJ}$  because of the reinforcement from the vertical walls. The significant difference between the impact absorption capacities for the different values of  $x$  is because the GRP material undergoes bending for  $x \leq 0.3$ . Contrarily, the GRP material undergoes compression for  $x \geq 0.3$ . The compressive loading for  $x \geq 0.3$  is because of the large influence of the vertical wall as compared to  $x \leq 0.3$ .



**Figure 5.2 Impact absorption capacity of square GRP cover at different locations**

### 5.3.4 Triangular geometry

Impact absorption capacity does not vary significantly at different locations on the triangular geometry. The geometry of the triangular GRP cover can be seen in Appendix A. The nomenclature used for triangular cover is similar to the square cover. Figure 5.3 shows the results of impact absorption capacity for different values of  $x$ . The impact absorption capacity at the centre of the cover is greater than the ends. Close to the ends of the cover there is a significant fall in the impact absorption capacity. Similarly, the impact absorption capacity of the triangular cover decreases as we move along the width of the cover ( $x$ -axis). This shows that the triangular GRP cover can bear maximum impact loads close to its pointed edge ( $x = 0, y = 0$ ). Unlike the square cover, the impact absorption capacity of the triangular cover does not change significantly along  $x$ -axis because of no reinforcement present from the side walls as in the case of square cover.

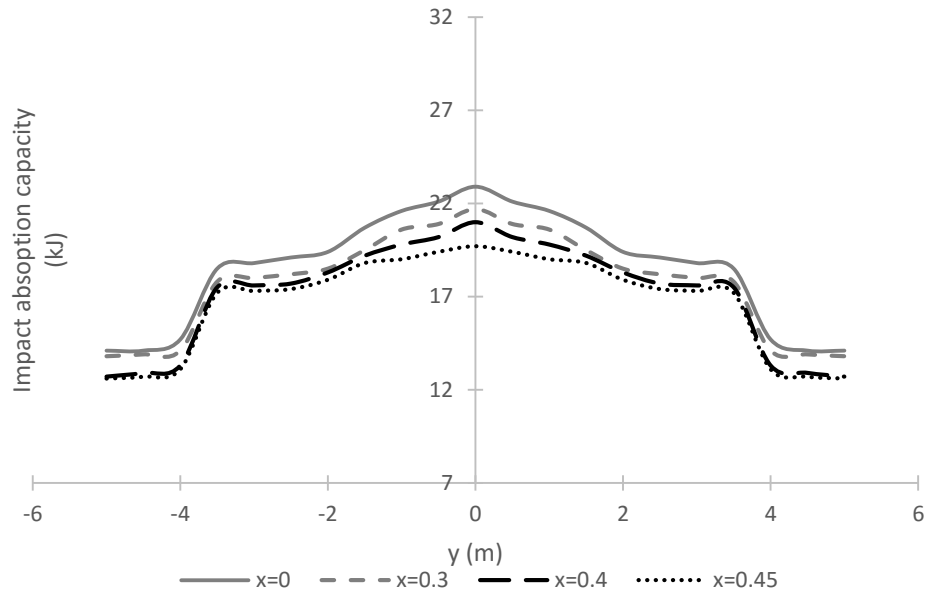
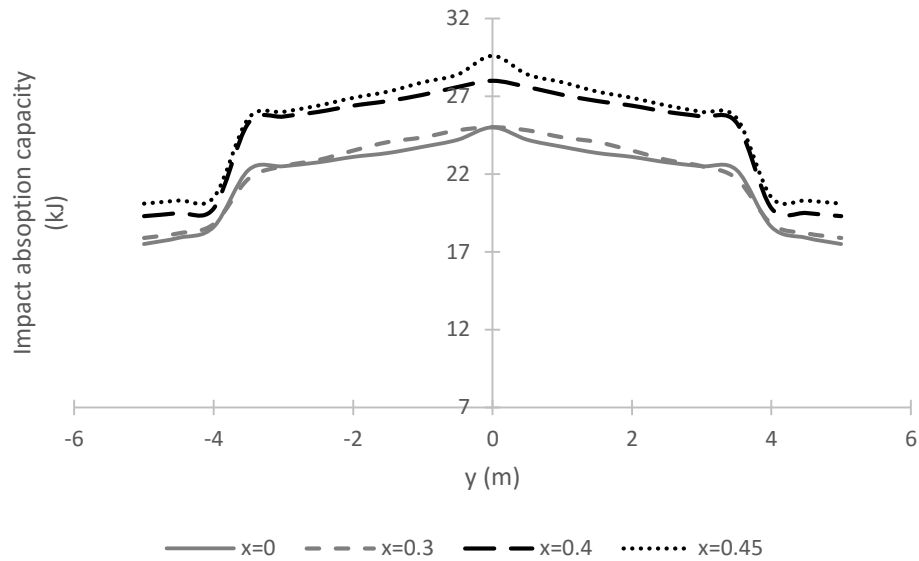


Figure 5.3 Impact absorption capacity of triangular GRP cover at different locations

### 5.3.5 Semi-circular geometry

Impact absorption capacity does not vary significantly at different locations on the semi-circular geometry. The geometry of the semi-circular GRP cover can be seen in Figures 4.8. The nomenclature used for semi-circular cover is similar to the square cover. Figure 5.4 shows the results for impact absorption capacity. A similar trend is observed for the semi-circular geometry as of triangular geometry in impact absorption capacity. However, the variation in the impact absorption capacity along the width of the cover (y-axis) is very small. Semi-circular GRP cover dominates square and triangular covers in impact absorption capacity. ANSYS simulation results at the key locations for all the three covers are shown in Appendix D.

For square and semi-circular geometries, impact absorption capacity increases along positive or negative x-axis. The reason observed is that the side walls contribute in absorbing the impact load. Triangular geometry shows opposite behaviour i.e. impact absorption capacity decreases along positive or negative x-axis. Whereas, along positive or negative y-axis, closer to the open ends of GRP cover, impact absorption capability decreases for all the covers.



**Figure 5.4 Impact absorption capacity of semi-circular GRP cover at different locations**

## 5.4 Conclusion

Drop-object impact loads are a major hazard for subsea pipelines and GRP covers are a tentative solution to this hazard. The behaviour of drop-objects impact load is different on different GRP cover geometries. The present study shows that among the square, triangular and semi-circular geometry, the semi-circular geometry has highest impact absorption capacity. The study also shows that the impact absorption capacity of different GRP covers is different along different directions.

For the drop-objects shown in Table 5.2, square, triangular and semi-circular geometry has the impact absorption capacity for small objects from oil and gas activity. The triangular and semi-circular geometry has the impact absorption capacity for all the fishing activity drop-objects.

(Intentionally left blank)

## Chapter 6

### Conclusion

In the present study, CFD simulation for obtaining essential hydrodynamic force coefficients, on-bottom stability analysis, fishing activity loads analysis and drop-object impact analysis are performed for the different shapes of three Glass Reinforced Plastic (GRP) subsea protection cover geometries (i.e. square, triangular and semi-circular). The main conclusions drawn are:

1. The numerical method used for performing CFD simulation in the present study is capable of predicting hydrodynamic force coefficients with a reasonable accuracy for the GRP covers on the flat seabed.
2. Among the three GRP covers analysed, the sequence of drag coefficient values from the lowest value to the highest is: semi-circular cover, triangular cover and square cover and the sequence of lift coefficient values is: triangular cover, square cover and semi-circular cover.
3. For the on-bottom stability analysis, the sequence from the lowest to the highest vertical forces on the GRP covers is: triangular cover, semi-circular cover and square cover and the sequence of the exposed horizontal forces is: semi-circular cover, triangular cover and square cover. The square cover is found to be the least stable cover for on-bottom stability.
4. Semi-circular GRP cover has the highest fishing activity loads-bearing capacity among all the three covers analysed.
5. For the drop-objects impact analysis, semi-circular cover has the highest impact absorption capacity followed by triangular and square cover in chronological order.

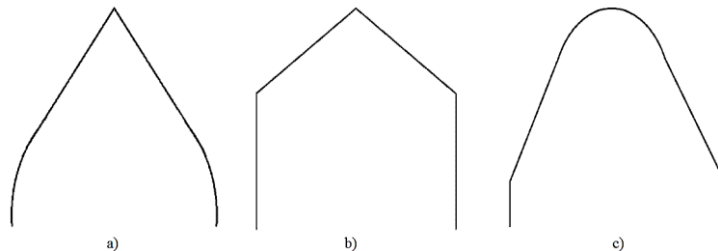
The results in this report have showed that each GRP cover has its own pros and cons. Therefore, it is recommended that the cover should be selected based upon the exposed loading conditions to the cover. For the hydrodynamic loads dominant condition, a triangular geometry

can be used and for the fishing activity dominant condition, a semi-circular geometry can be used. Therefore, a load specific design could best serve the purpose. However, if the field specific data is unavailable; the semi-circular geometry should be the first choice.

## Recommended future work

In this report square, triangular and semi-circular geometries are analysed for geometry optimization. At the end of this report, it is feasible to point out the possible future research areas. Following are the possible future areas of research:

- Subsea covers can be made up with hybrid cross-sections as shown in Figures a), b) & c). The hybrid geometries can serve as an effective option for the GRP cover designs. A detailed study on hybrid geometries can be carried out.
- Installation loadings like (lifting, sea-fastening, lowering through the splash zone and sea bed impact) have not been studied. Thus a detailed study on these loading conditions can be carried out.
- Experimental validation study of all the numerical results calculated in this report can be conducted.



**Figure 6.1 Hybrid cover cross-sections**

(Intentionally left blank)



## References

Adams, E. W., & Johnston, J. P. (1988). Effects of Separating Shear Layer on the Reattachment of Structure. Part 2: Reattachment Length and Wall Shear Stress.

American Bureau of Shipping (2013). Guidance Notes on Accidental Load Analysis and Design for Offshore Structures. Houston.

ANSYS, Inc. (2012). Composite Introduction, ANSYS Inc., Pennsylvania, USA.

ANSYS, Inc. (2013). ANSYS Composite Prep Post User's Guide, ANSYS Inc., Pennsylvania, USA.

Barbero, E. J. (2008). Finite Element Analysis of Composite Materials. CRC Press, West Virginia, USA.

Cengel, Y. A. & Cimbala, J. A. (2006). Fluid Mechanics: Fundamentals and Applications. International Edition, McGraw Hill Publication.

Cengel, Y. A. & Cimbala, J. A. (2010). Fluid Mechanics: Fundamentals and Applications, 2nd Edition, McGraw Hill Publication.

Chawla, K. K. (1987). Composite Materials Science and Engineering. Springer-Verlag, Germany.

Code-Saturne (2014). Cell Size at the Wall. Retrieved on 05-05-2016, from:

<http://code-saturne.org/cms/sites/default/files/fileattach/BPG/BPG-3-Cell-Size-At-The-Wall.pdf>

CSUB (2016). Retrieved on 02-05-2016, from:

<http://csub.com/gallery/3d-presentations/>

DNV-RP-C205 (2010). Environmental Conditions and Environmental Loads. Det Norske Veritas AS.

DNV-OS-C501 (2010). Composite Components. Det Norske Veritas AS.

DNV-OS-H205 (2014). Lifting Operations. Det Norske Veritas AS.

DNV-RP-F109 (2010). On-Bottom Stability Design of Submarine Pipelines. Det Norske Veritas AS.

DNV-RP-H103 (2011). Modelling and Analysis of Marine Operations. Det Norske Veritas AS.

DROPS members, 2010. Subsea Dropped Objects: DROPS Dropped Object Prevention scheme. Retrieved on 07-04-2016, from:

<http://www.dropsonline.org/assets/documents/DROPS-SubseaDROPS.pdf>

Ecke, R. (2005). The Turbulence Problem: An Experimentalist's Perspective. Los Alamos Science.

Ellinas, C. P. (1990). Advances in Subsea Pipeline Engineering and Technology. Advances in Underwater Technology, Ocean and Offshore Engineering.

Frei, W. (2013). Which Turbulence Model should I choose for my CFD Application?. Retrieved on 02-05-2016, from:

<http://www.comsol.com/blogs/which-turbulence-model-should-choose-cfd-application/>

Fujimoto, H., Isomura, M., & Ajisaka, K. (1975). Flow over Rectangular Cylinders Immersed in a Turbulent Boundary Layer, Bulletin of the JSME.

Ghebregiorghis, D. A. (2014). On-bottom Stability Analysis of Subsea Pipelines according to DNV-RP-F109. Master Thesis Spring, University of Stavanger.

Gibson, R. F. (1994). Principles of Composite Material Mechanics. McGraw-Hill Inc., USA.

Good, M. C., & Joubert, P. N. (1968). The Form Drag of 2-Dimensional Bluff-Plates Immersed in Turbulent Boundary Layers. Journal of Fluid Mechanics.

HSE, Health and Safety Executive (2003). PARLOC 2001: The Update of Loss of Containment Data for Offshore Pipelines.

IMO-b (2002). Guidelines for Formal Safety Assessment (FSA) for Use in the IMO Rule-Making Process. MSC/Circ. 392, London, U.K.

Institution of Mechanical Engineers (1998). Foreign Object Impact and Energy Absorbing Structure. 1<sup>st</sup> Edition, Wiley, New York.

Keshmiri, A. (2012). Numerical Sensitivity Analysis of 3D and 2D Rib-Roughened Channels. Heat and Mass Transfer.

Launder, B., & Spalding, D. (1974). The Numerical Computation of Turbulent Flows. Computer Methods in Applied Mechanics and Engineering.

Liu, Y. Z., Ke, F., & Sung, H. J. (2008). Unsteady Separated and Reattaching Turbulent Flow over a Two-Dimensional Square Rib. Journal of Fluids and Structures.

Liu, Y., HU, H. & Zhang, D. (2011). Probability Analysis of Damage to Offshore Pipeline by Ship Factors. Transportation Research Board 92th 27 Annual Meeting 28 for Presentation and Publication, July.

Liu, Y. T., Hu, H. & Zhong, D. (2013). Probability Analysis of Damage to Offshore Pipeline by Ship Factors. TRB annual meeting.

Muhlbauer, W.K. (2004). Pipeline Risk Management Manual Ideas, Techniques, and Resources. 3rd Edition, Gulf Professional Publishing, Burlington, MA, USA.

NAVFAC DM7.01 (1986). Soil Mechanics, Naval Facilities Engineering. Command 200 Stovall Street Alexandria, Virginia 22322-2300.

NORSOK Standard U-002 (1998). Subsea Structures and Piping System. Rev. 2, Norwegian Petroleum Industry.

PJNC (2016). Retrieved on 10-03-2016, from:

<http://www.pjnc.co.uk/>

PRC, International American Gas Association (IAGA) (1999). Final Report on Analysis of DOT Reportable Incidents for Hazardous Liquid Pipelines, 1986 through 1996. The American Petroleum Institute, Pipeline Segment, API publication. Keifner and Associate Inc., Washington, DC, USA.

PRC, International American Gas Association (IAGA) (2000). Analysis of DOT Reportable incidents for gas transmission and gathering system pipelines, 1985 through 1997. Keifner and Associate Inc., Washington, DC, USA.

Sadraey, M. H. (2009). Aircraft Performance Analysis. VDM Verlag Dr. Müller.

Sumer, B. M. & Fredsøe, J. (1997). Hydrodynamics around Cylindrical Structures: Advanced series on Ocean Engineering, World Scientific, Singapore.

Ulversøy, E. (2013). Finite Element Analysis and Experimental Testing of Lifting Capacity for GRP Cover. Master Thesis Spring, University of Stavanger, Stavanger.

Versteeg, H., & Malalasekera, W. (2007). An Introduction to Computational Fluid Dynamics: the Finite Volume Method. Pearson Education Limited.

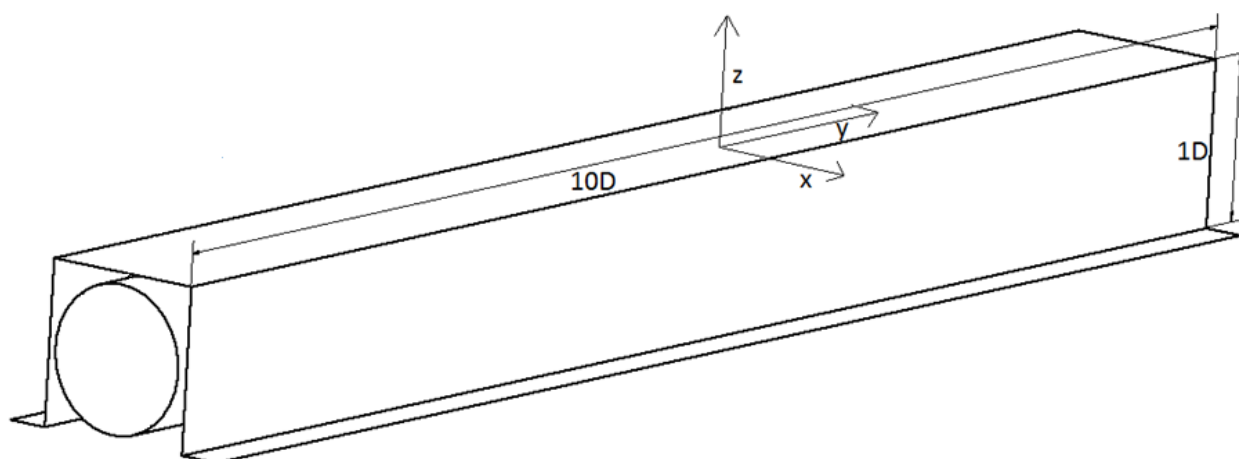
Wimpey Laboratories, Brown I.C. & Perry, S.H. (1989). The Assessment of Impact Damage Caused by Dropped Objects on Concrete Offshore Structures. OTH 87 240, CIRIA/WEG, Westminster.

(Intentionally left blank)

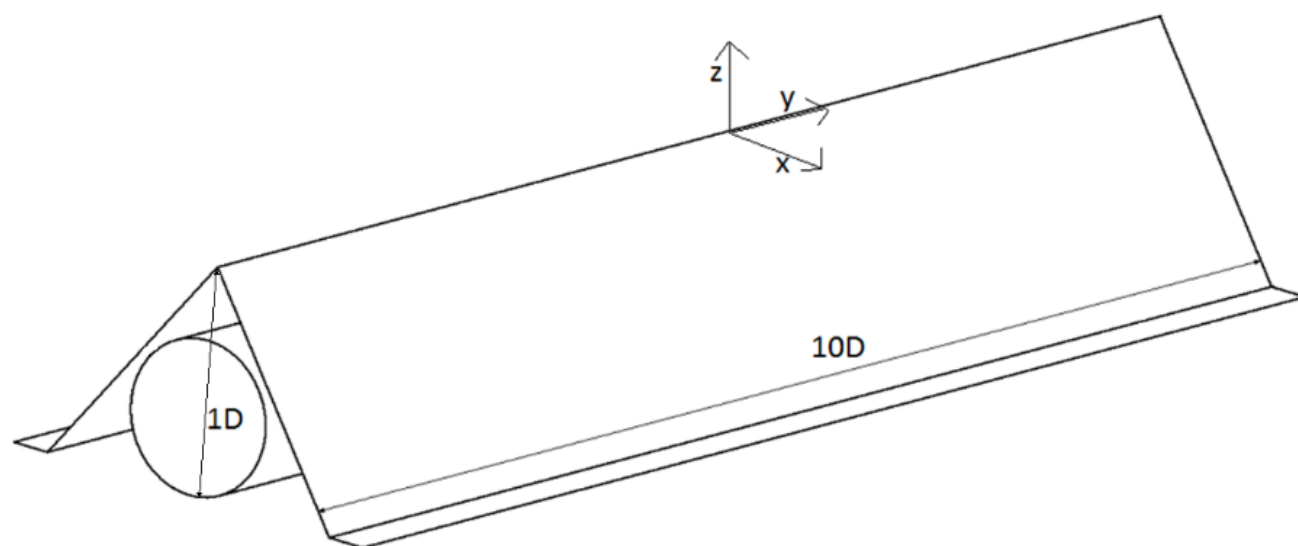
*Appendix A*

Geometry dimensions where  $D = 1\text{m}$

Square cover

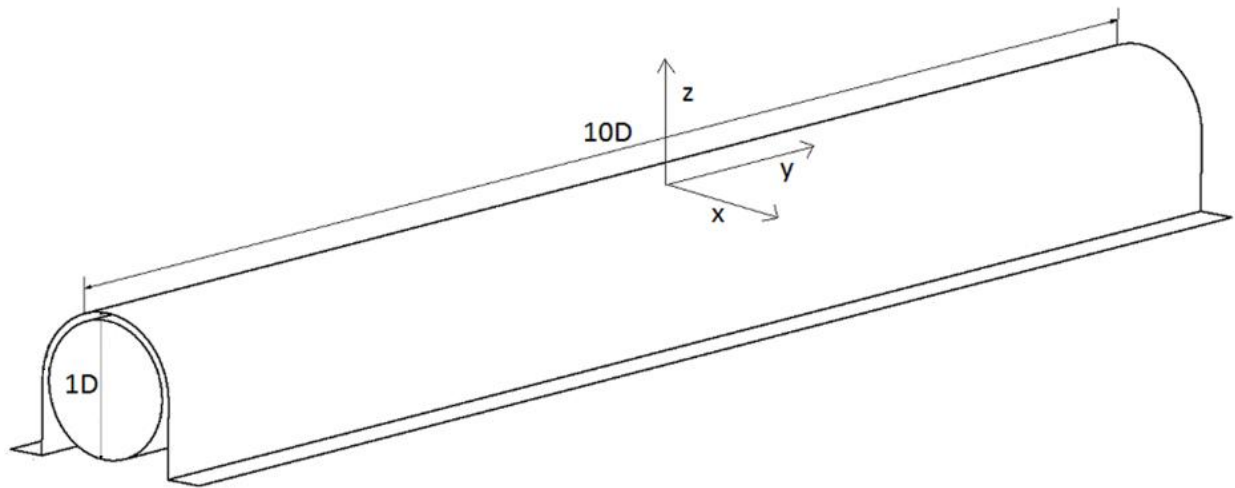


Triangular cover



ii

Semi-circular cover



## Appendix B

### Wave Velocity and Acceleration (10 year)

Calculation for vertical and horizontal, velocity and acceleration for 10 year is as following:

Spectrum Check:

$$3.6 < \frac{T_p}{\sqrt{H_s}} < 5$$

$$3.6 < 4.14 < 5 \quad (\text{DNV-RP-H103, 2013})$$

Hence, a Jonswap spectrum is applicable

$$T = T_p (0.6673 + 0.05037 \gamma - 0.00623 \gamma^2 + 0.0003341 \gamma^3)$$

Since,  $\gamma = \exp\left(5.57 - \frac{1.15 T_p}{\sqrt{H_s}}\right)$  (DNV-RP-H103, 2011)

$$\gamma = 2.24$$

So,  $T = 11.06 \text{ s}$

Dispersion Relation  $\omega^2 = gk \tanh(kd)$

$$\omega = 2\pi/T$$

$$\omega = 0.568$$

As  $a = (0.9 H_s) 1.1 = 12.47 \text{ m}$

Iterating for 'k' in dispersion relation  $k = 0.033$

Horizontal particle velocity  $= u = \omega a \frac{\cosh k(D+d)}{\sinh kd} \cos(\omega t - kx)$

(DNV-RP-C205, 2010)

Setting oscillatory function=1 for maximum velocity,

Max Horizontal particle velocity  $= u = \omega a \frac{\cosh k(D+d)}{\sinh kd} = 0.45 \text{ m/s}$

(DNV-RP-C205, 2010)

Similarly,

$$\text{Max Vertical particle velocity} = v = \omega a \frac{\sinh k(D+d)}{\sinh kd} = 0.015 \text{ m/s}$$

(DNV-RP-C205, 2010)

Similarly,

$$\text{Max Horizontal particle acceleration} = a_u = \omega^2 a \frac{\cosh k(D+d)}{\sinh kd} = 0.26 \text{ m/s}^2$$

(DNV-RP-C205, 2010)

$$\text{Max Vertical particle acceleration} = a_v = \omega^2 a \frac{\sinh k(D+d)}{\sinh kd} = 0.0086 \text{ m/s}^2$$

(DNV-RP-C205, 2010)

### Wave Velocity and Acceleration (1 year)

Calculation for vertical and horizontal, velocity and acceleration for 1 year is as following:

Spectrum Check

$$3.6 < \frac{T_p}{\sqrt{H_s}} < 5$$

$$3.6 < 4.11 < 5$$

So,  $T = T_p (0.6673 + 0.05037 \gamma - 0.00623 \gamma^2 + 0.0003341 \gamma^3)$

$$\gamma = \exp \left( 5.57 - \frac{1.15 T_p}{\sqrt{H_s}} \right)$$

$$\gamma = 2.32$$

$$T = 9.96 \text{ s}$$



Using linear wave theory:

$$\begin{aligned} \text{Dispersion Relation} \quad \omega^2 &= gk \tanh(kd) \\ \omega &= 2\pi/T = 0.63 \text{ Hz} \\ a &= (0.9 \text{ Hs}) 1.1 = 10.20 \text{ m} \end{aligned}$$

$$\text{Iterating for 'k' in dispersion relation } k = 0.041$$

$$\text{Horizontal particle velocity} = u = \omega a \frac{\cosh k(D+d)}{\sinh kd} \cos(\omega t - kx)$$

Setting oscillatory function=1 for maximum velocity value,

$$\text{Max Horizontal particle velocity} = u = \omega a \frac{\cosh k(D+d)}{\sinh kd} = 0.18 \text{ m/s}$$

Similarly,

$$\text{Max Vertical particle velocity} = v = \omega a \frac{\sinh k(D+d)}{\sinh kd} = 0.007 \text{ m/s}$$

$$\text{Max Horizontal particle acceleration} = a_u = \omega^2 a \frac{\cosh k(D+d)}{\sinh kd} = 0.11 \text{ m/s}^2$$

$$\text{Max Vertical particle acceleration} = a_v = \omega^2 a \frac{\sinh k(D+d)}{\sinh kd} = 0.0047 \text{ m/s}^2$$

Validating applicability of Morrison Equation

$$\text{where } \lambda \text{ (wave length)} = gT^2/2\pi \quad (\text{DNV-RP-H103, 2013})$$

$$= 207.1\text{m} \ \& \ 243.3\text{m} \quad (\text{For } T=11.47 \ \& \ T=12.48, \text{ respectively})$$

Morrison equation is applicable if  $D/\lambda < 0.2$

Since,  $D=1\text{m}$ ,  $D/\lambda = 0.005$  &  $D/L = 0.004$

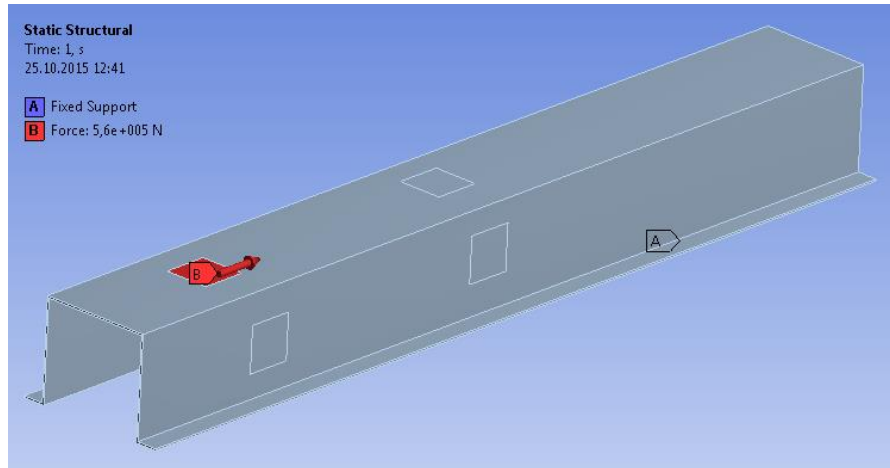
And  $H_s/\lambda < 0.14$  (Non-breaking waves)

$H_s/\lambda = 0.07$  &  $H_s/L = 0.06$

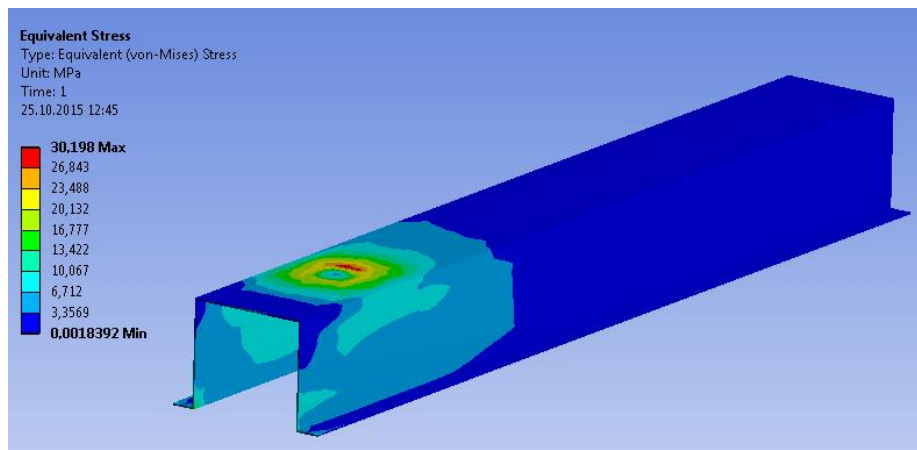
Hence, Morrison equation is applicable.

*Appendix C***Simulation results at other critical locations for trawlnet friction loading**

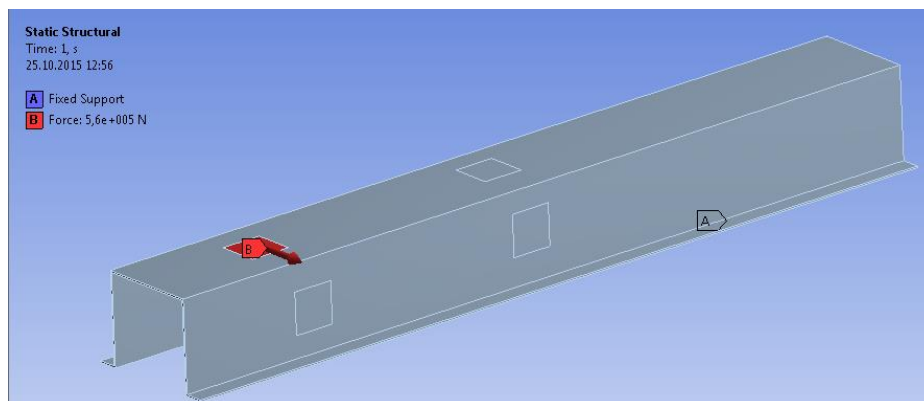
Force along longitudinal axis at the cover end



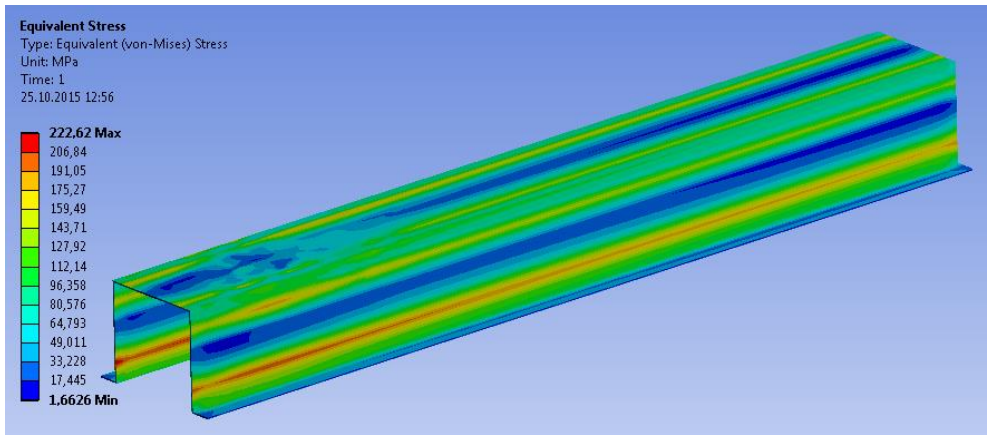
Equivalent Stress for the force along longitudinal axis at the cover end



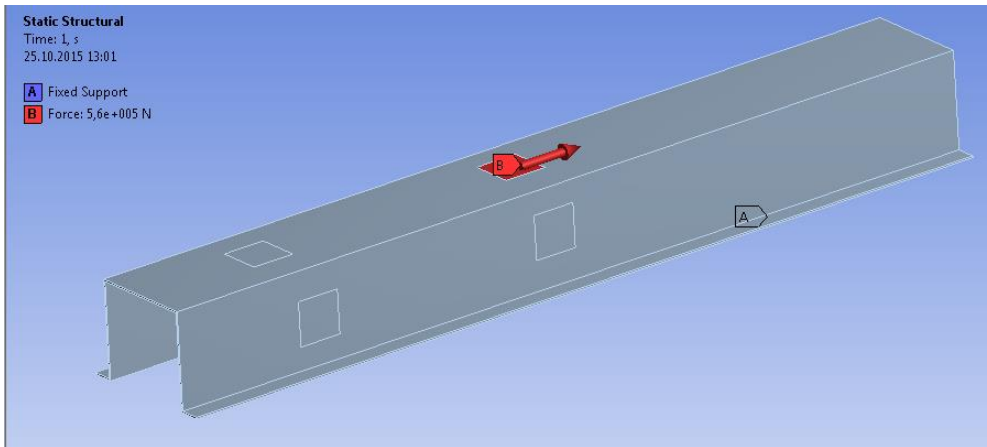
Force along minor axis at the cover end



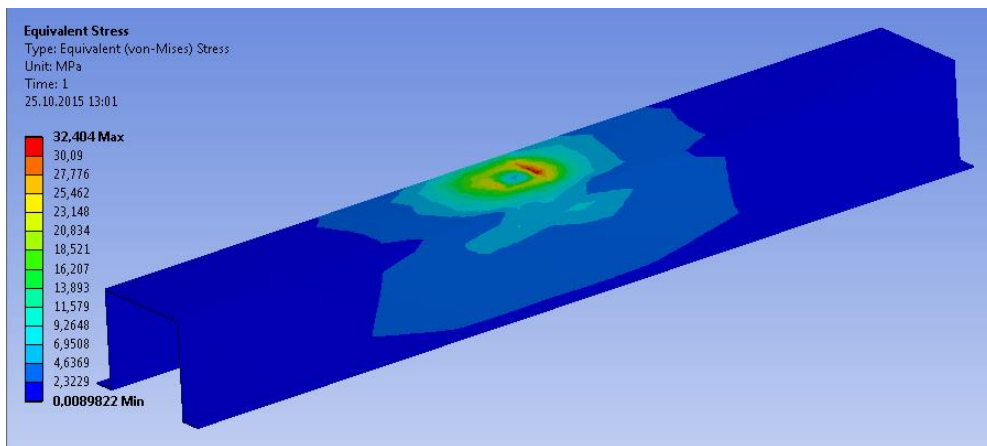
Equivalent Stress for the force along minor axis at the cover end



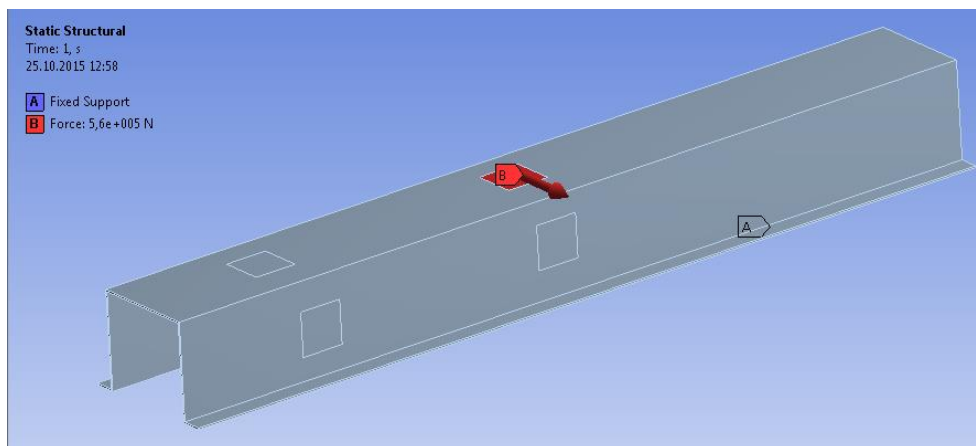
Force along longitudinal axis at the cover centre



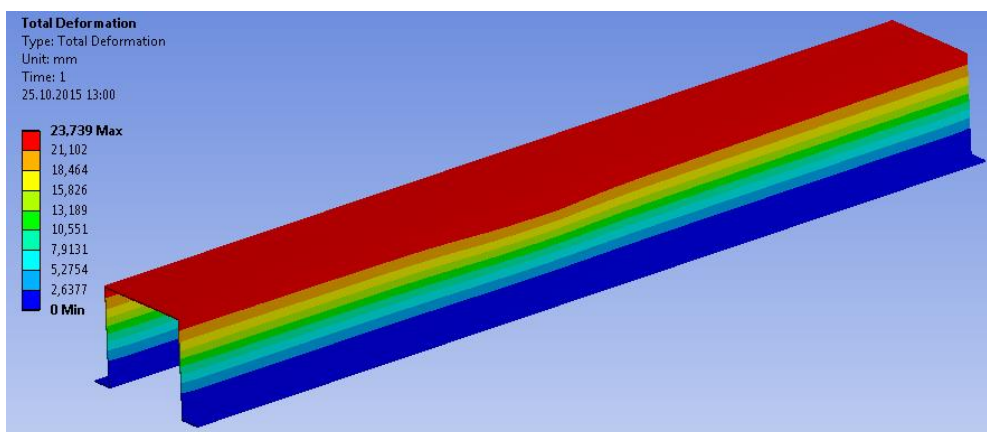
Equivalent Stress for the force along longitudinal axis at the cover centre



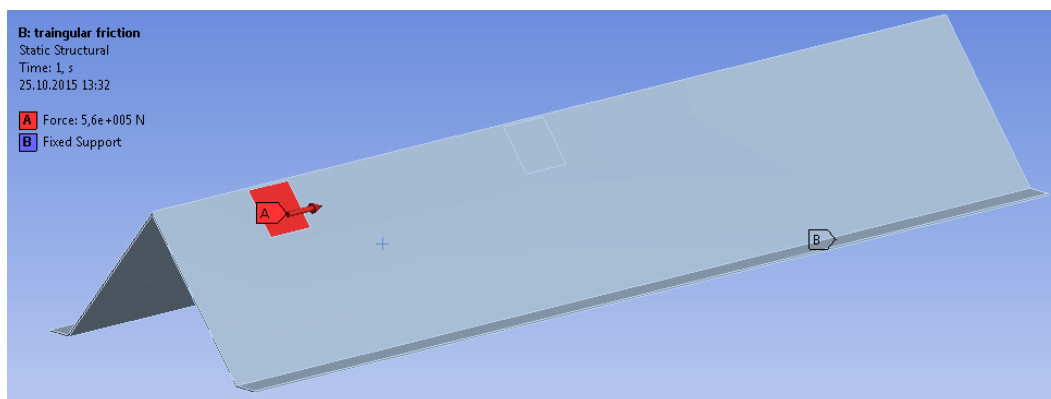
## Force along minor axis at the cover centre



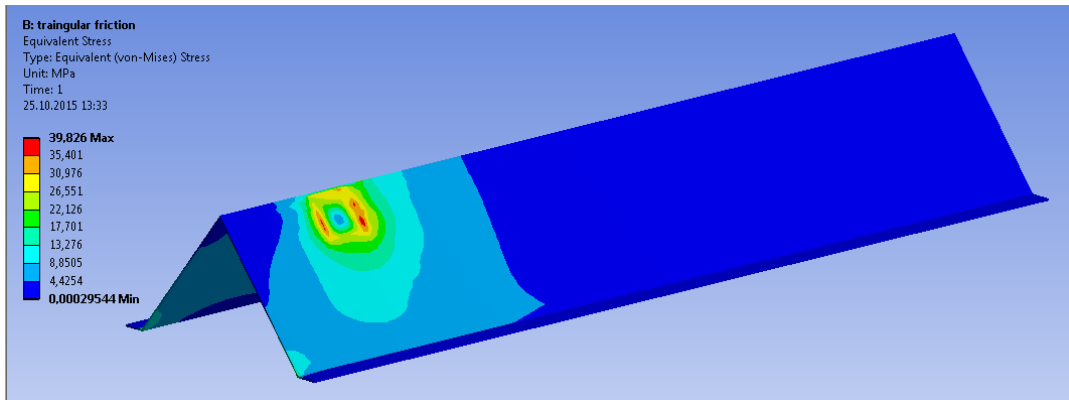
## Equivalent Stress for the force along minor axis at the cover centre



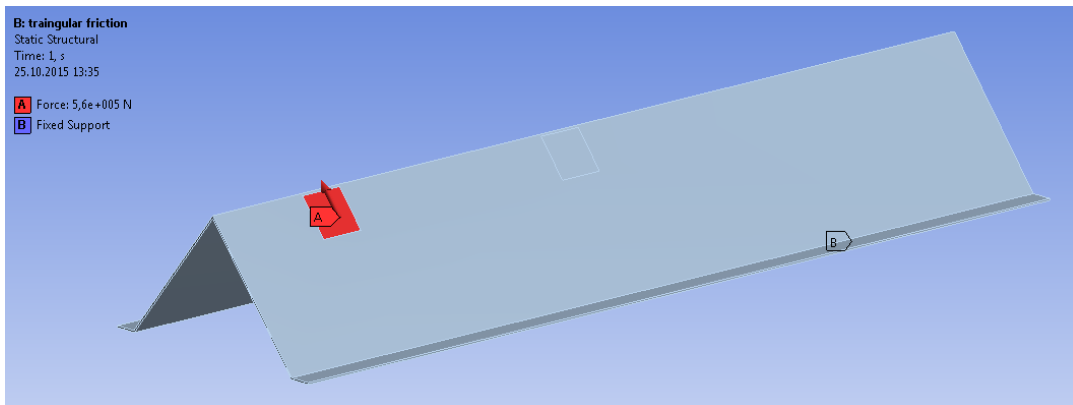
## Force along longitudinal axis at the cover end



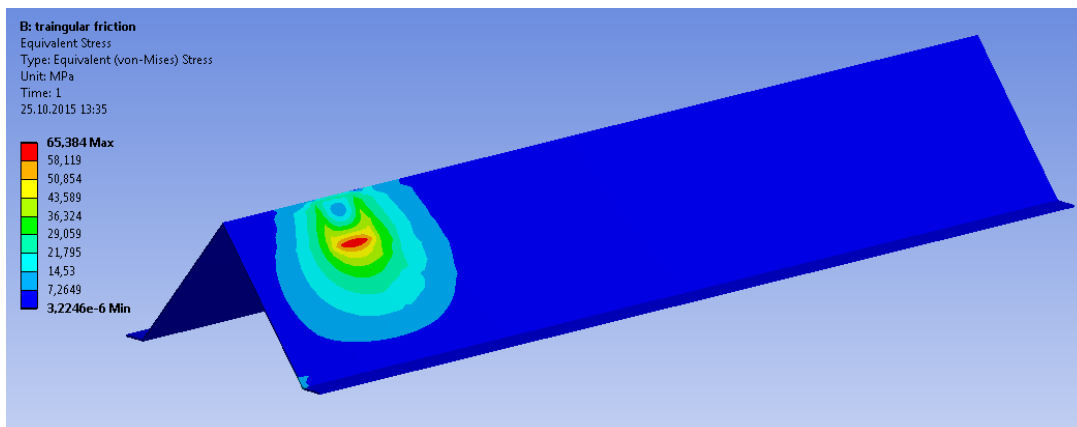
### Equivalent Stress for the force along longitudinal axis at the cover end



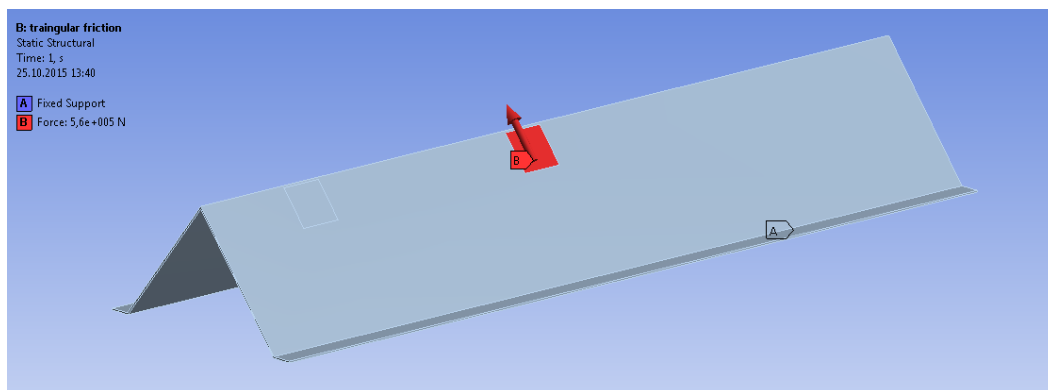
### Force along minor axis at the cover end



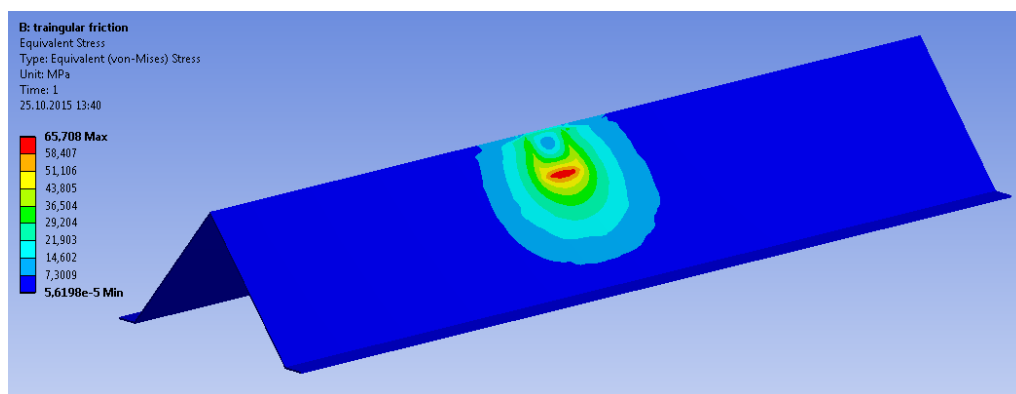
### Equivalent Stress for the force along minor axis at the cover end



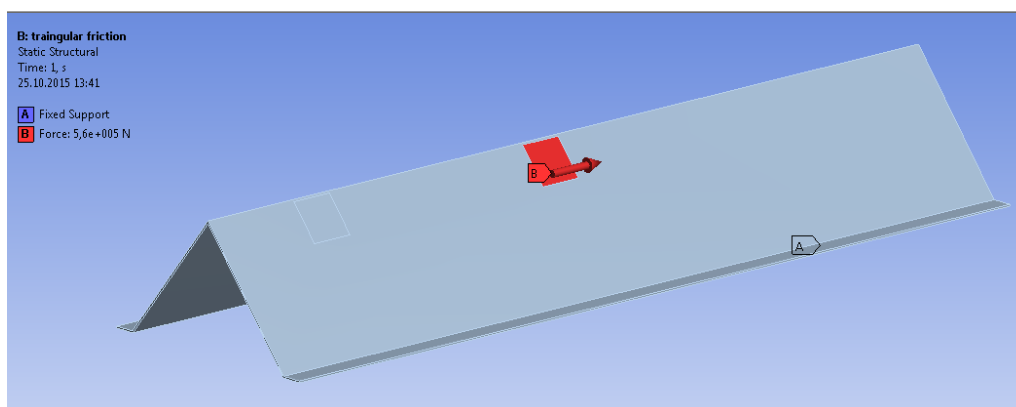
## Force along minor axis at the cover centre



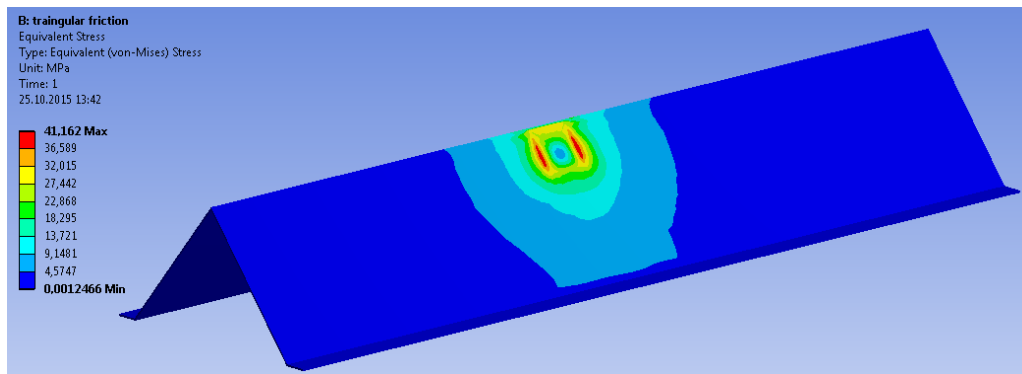
## Equivalent Stress for the force along minor axis at the cover centre



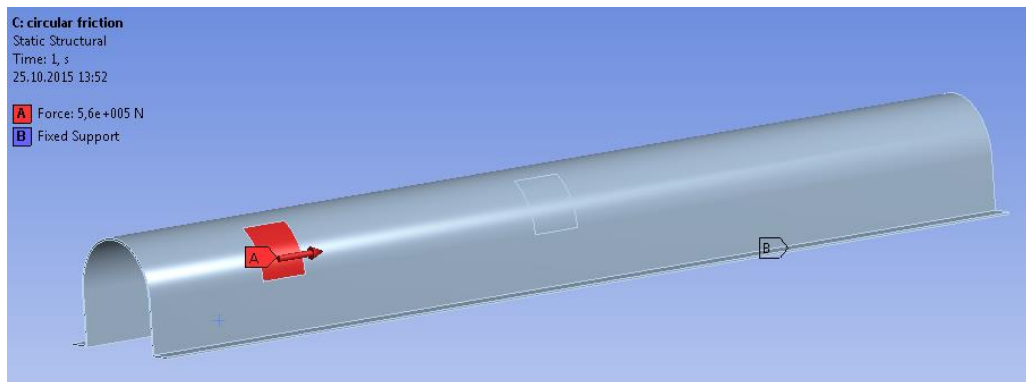
## Force along longitudinal axis at the cover centre



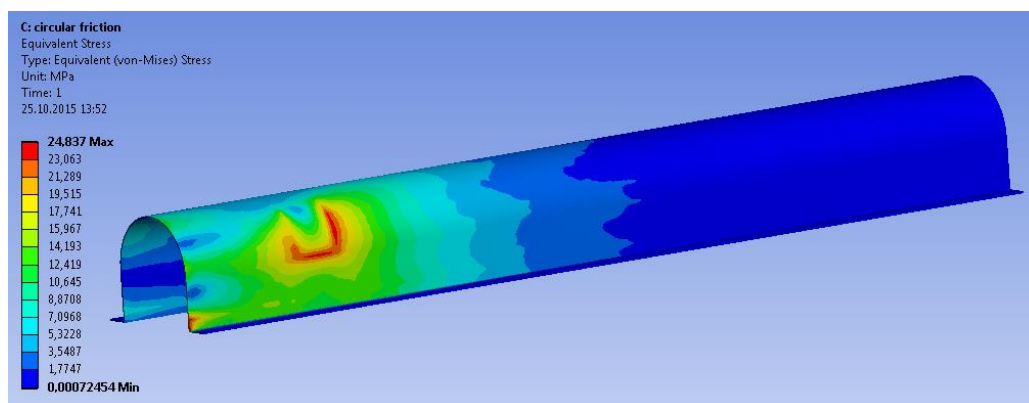
### Equivalent Stress for the force along longitudinal axis at the cover centre



### Force along longitudinal axis at the cover end

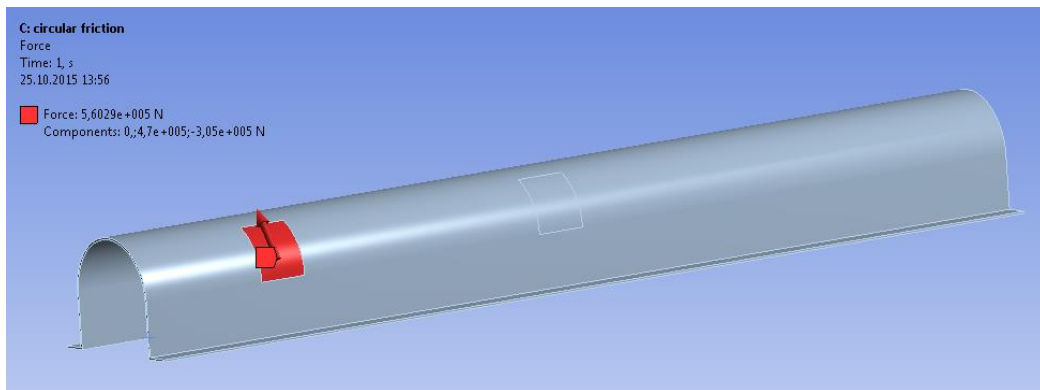


### Equivalent Stress for the force along longitudinal axis at the cover end

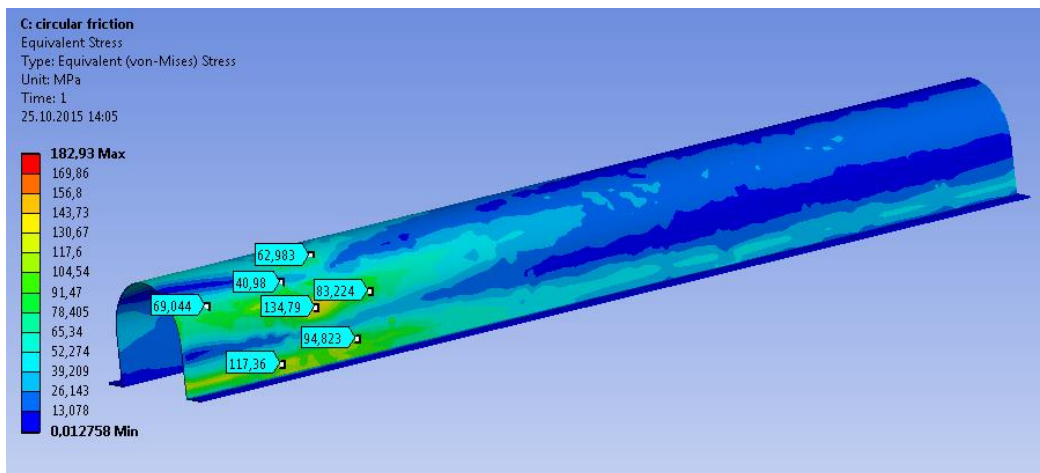
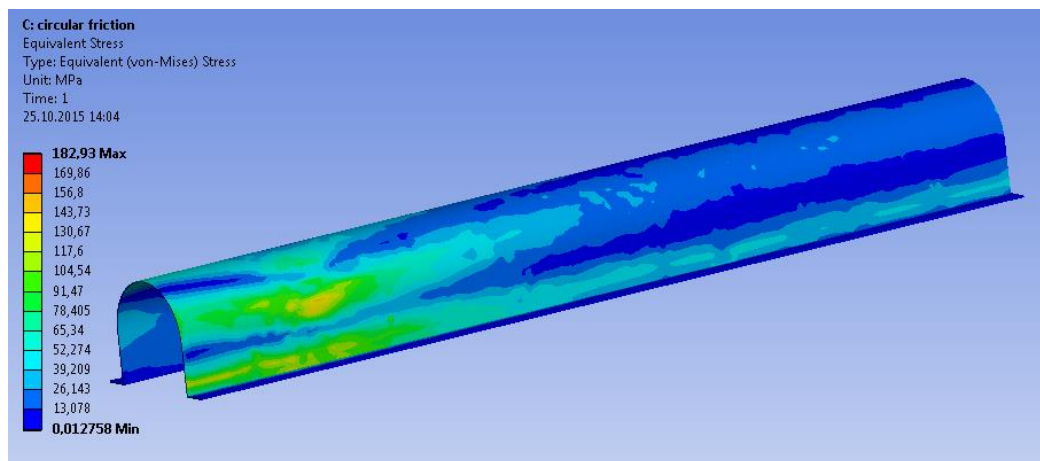




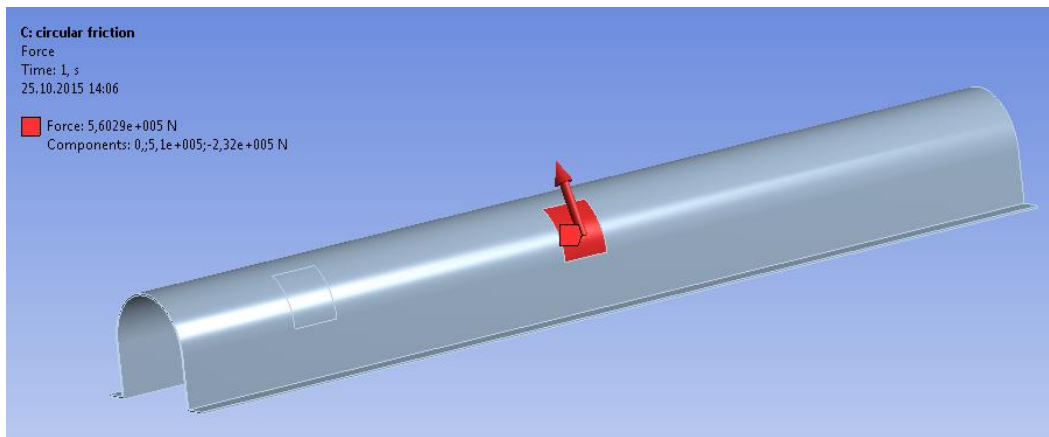
Force along minor axis at the cover end



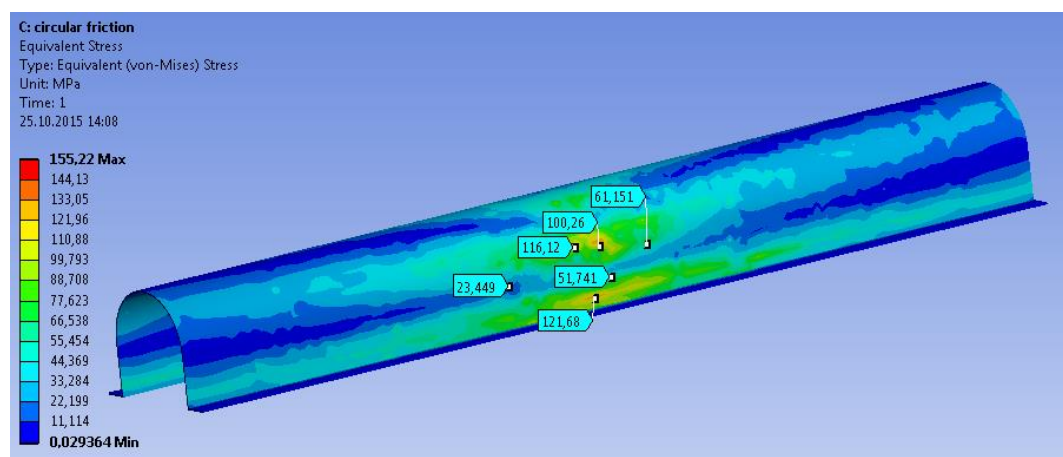
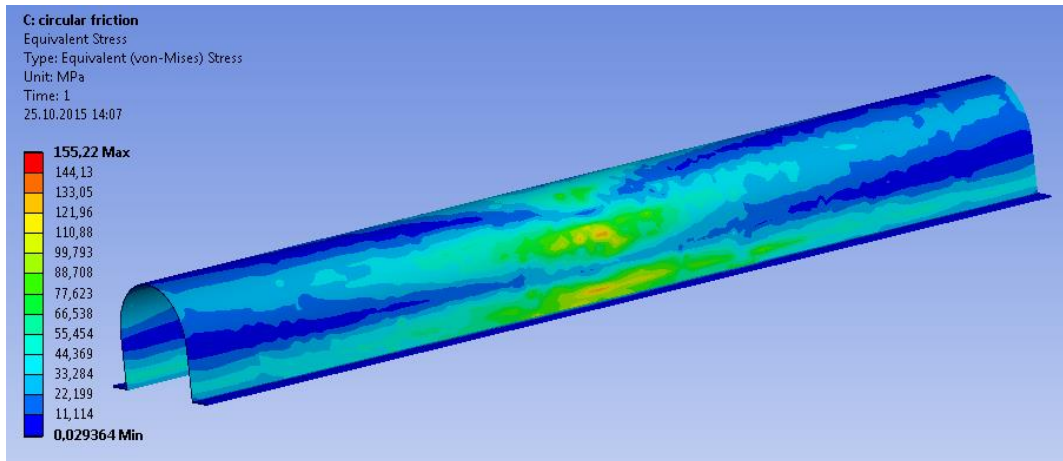
Equivalent Stress for the force along minor axis at the cover end



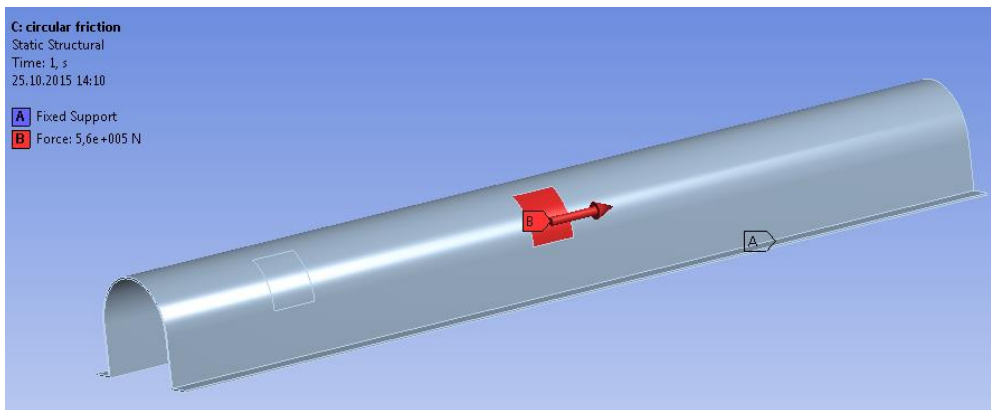
Force along minor axis at the cover centre



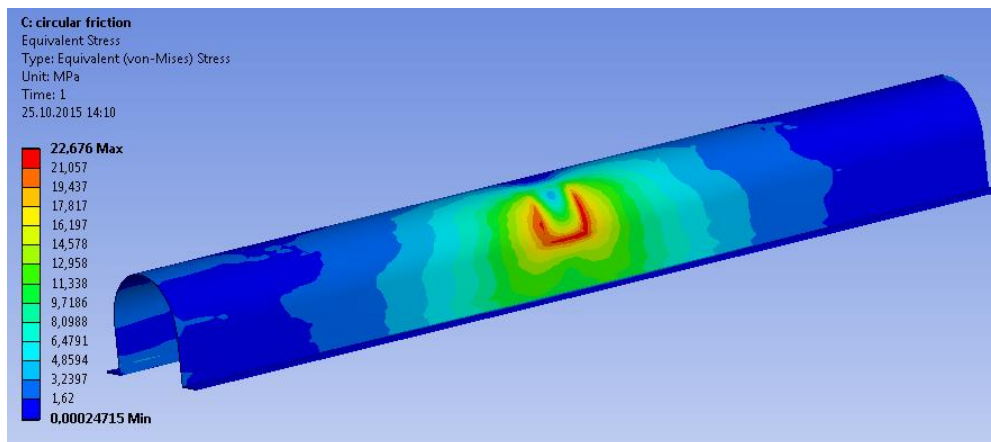
Equivalent Stress for the force along minor axis at the cover centre



Force along longitudinal axis at the cover centre

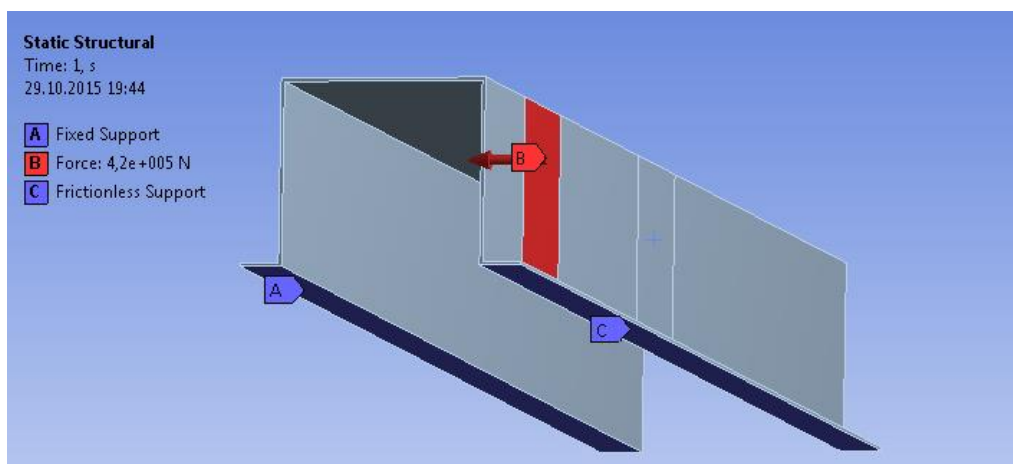


Equivalent Stress for the force along longitudinal axis at the cover centre

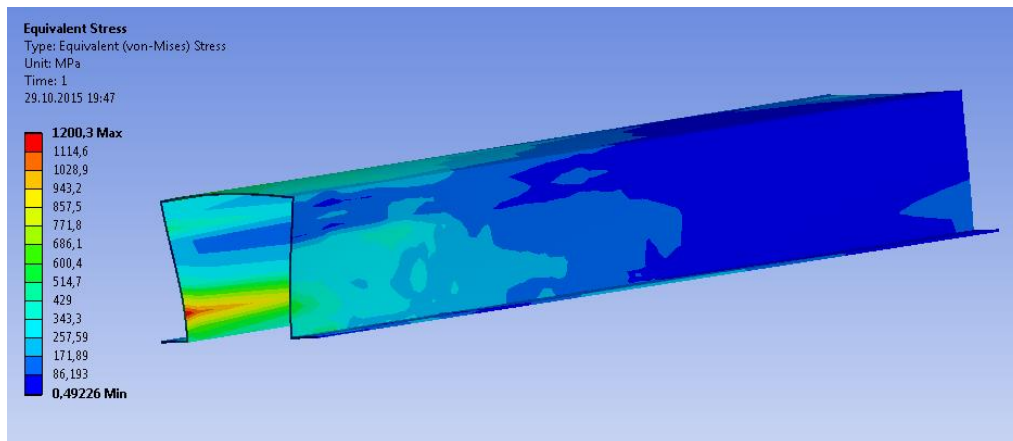


Simulation results at other critical locations for trawlboard overpull loading

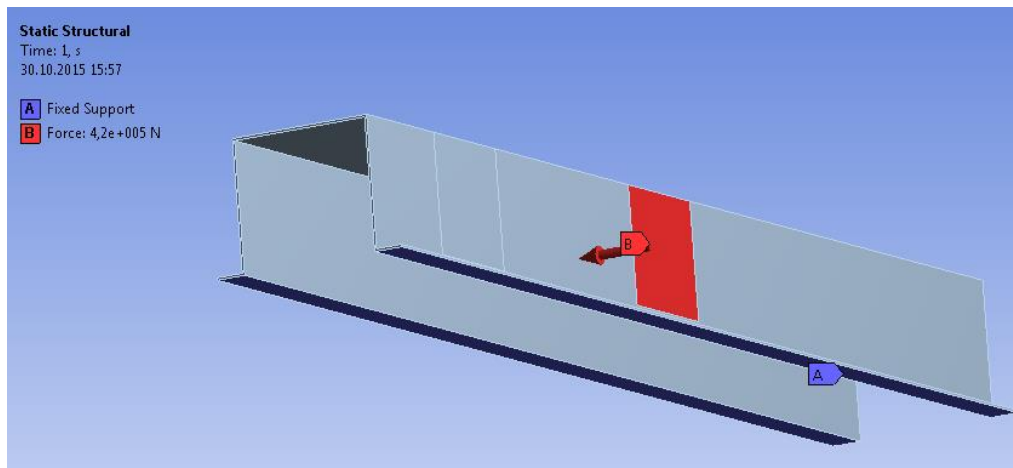
At the cover end



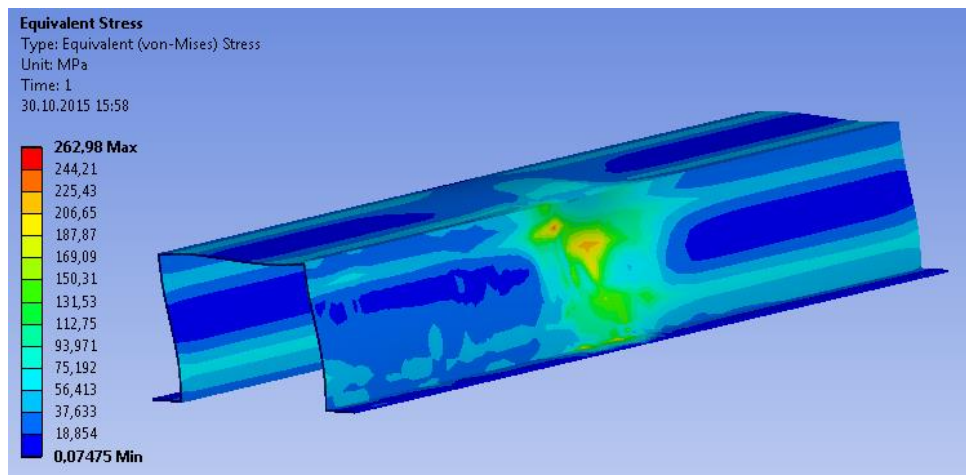
### Equivalent Stress for the Trawlboard Overpull at the cover end



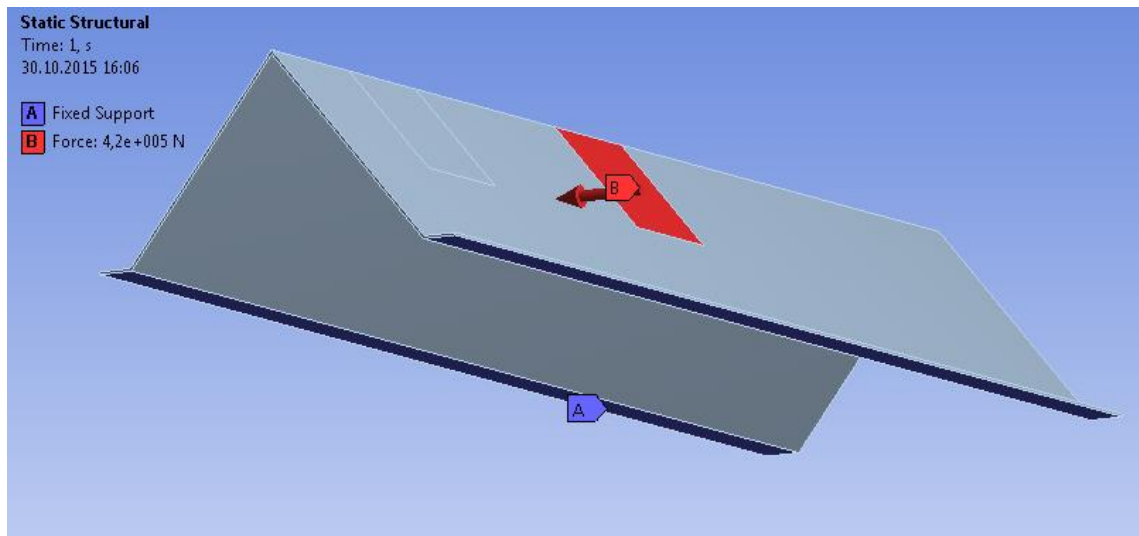
### At the cover centre



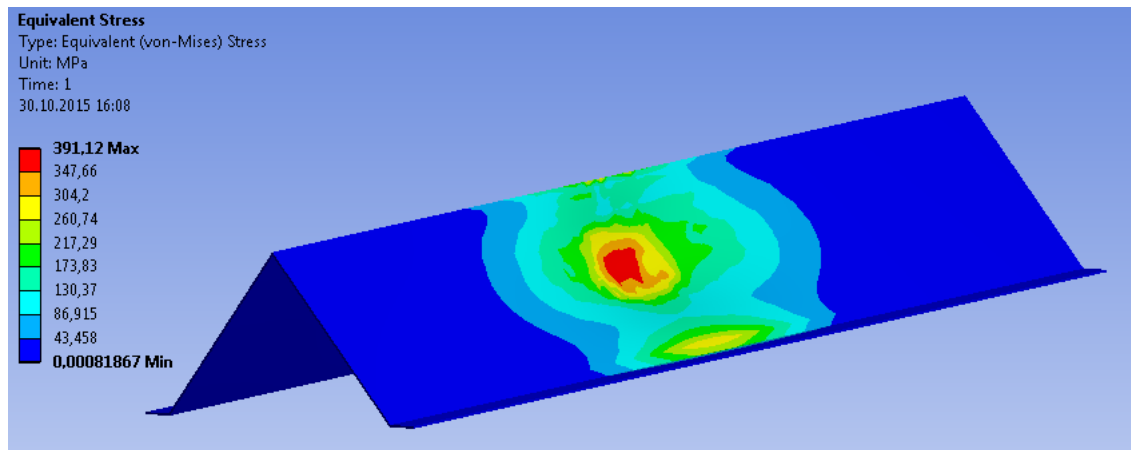
### Equivalent Stress for the Trawlboard Overpull at the cover centre



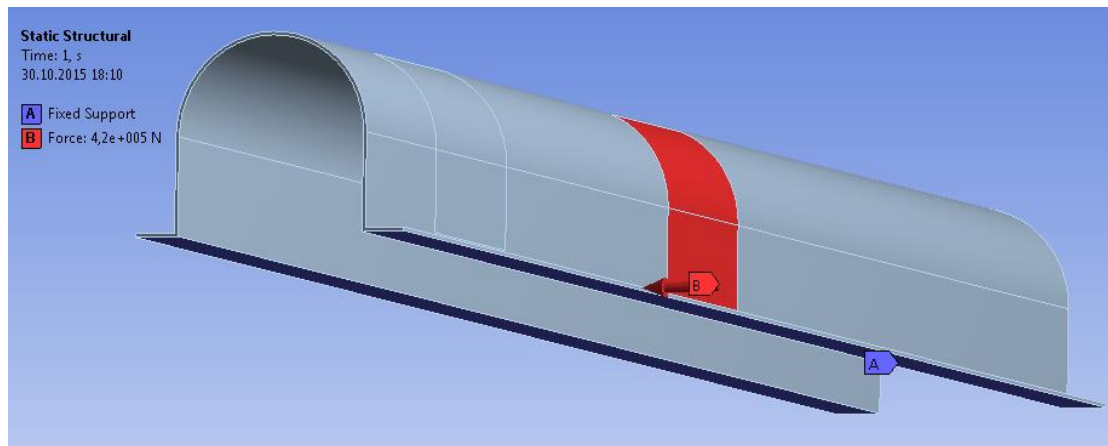
At the cover centre



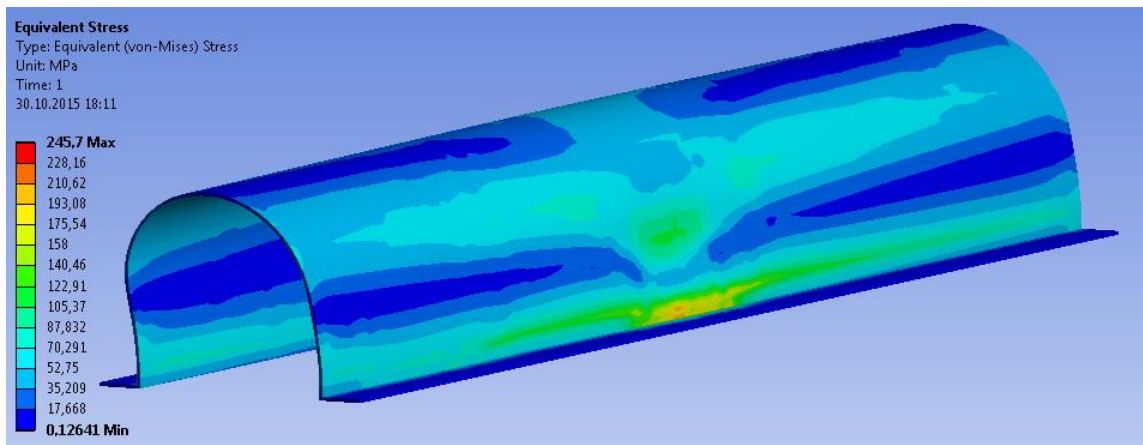
Equivalent Stress for the Trawlboard Overpull at the cover centre



At the cover centre



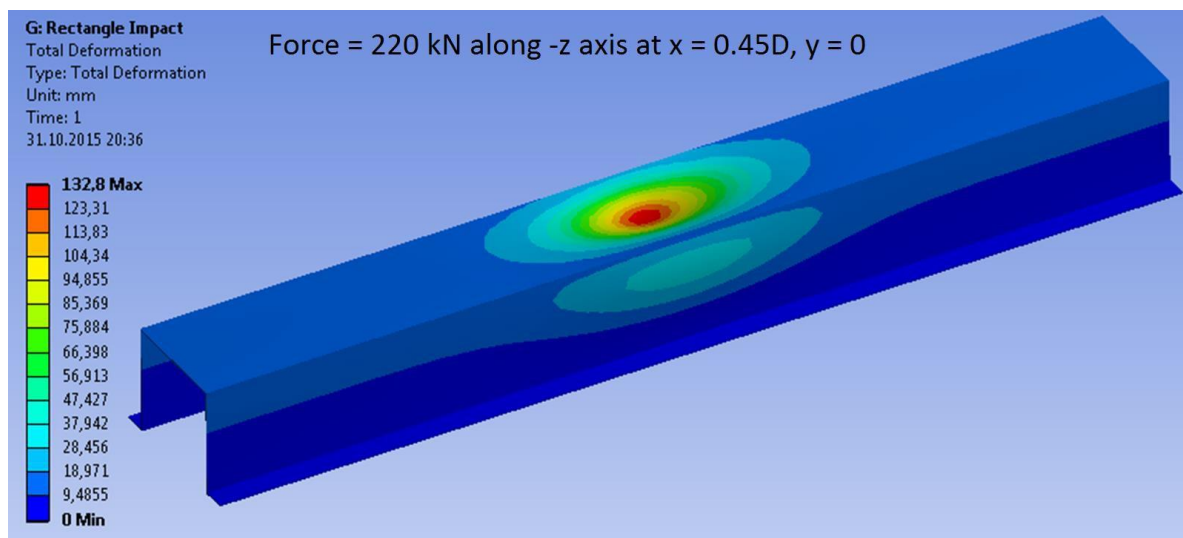
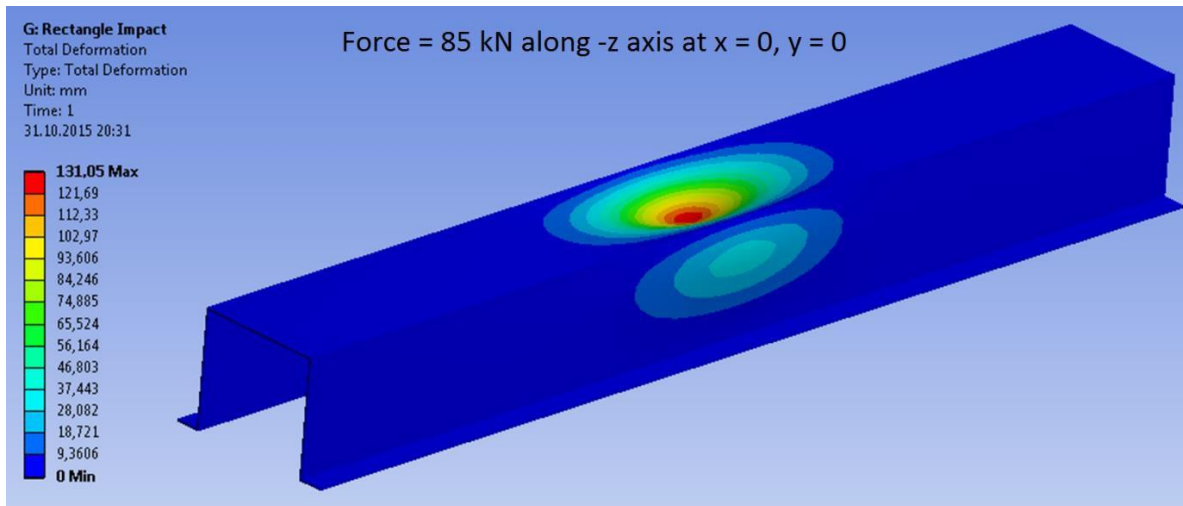
Equivalent Stress for the Trawlboard Overpull at the cover centre

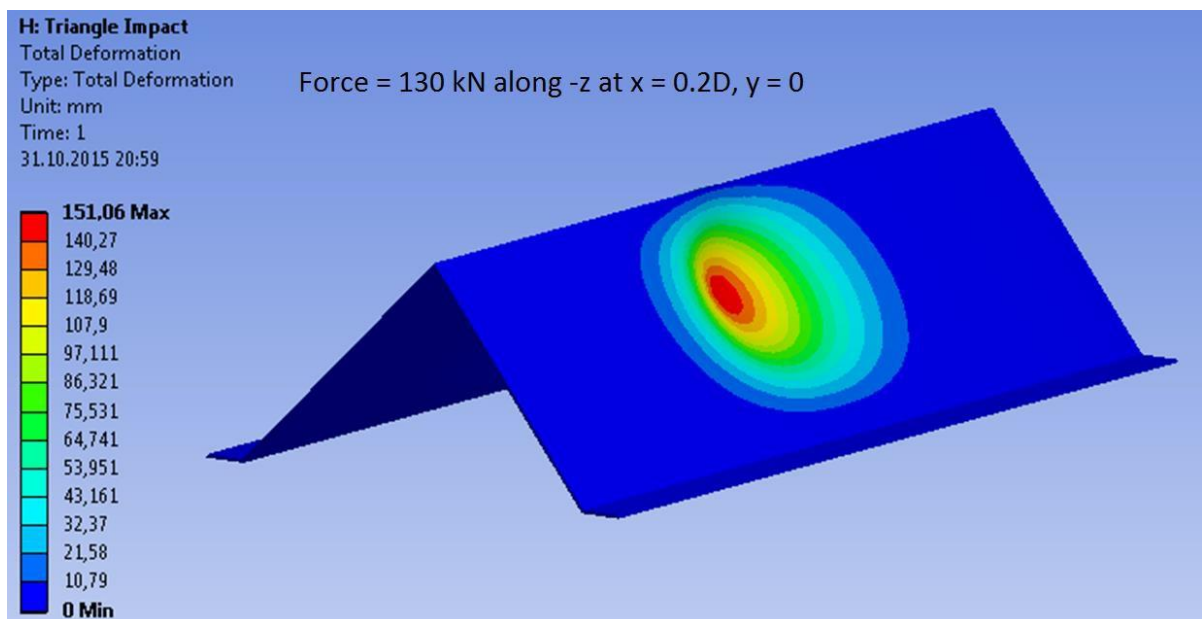
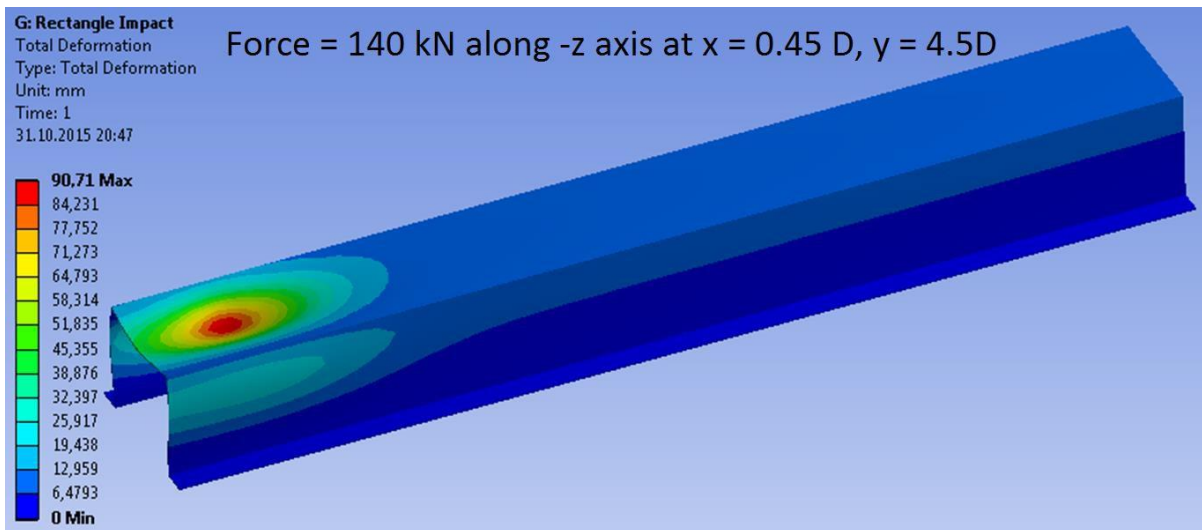
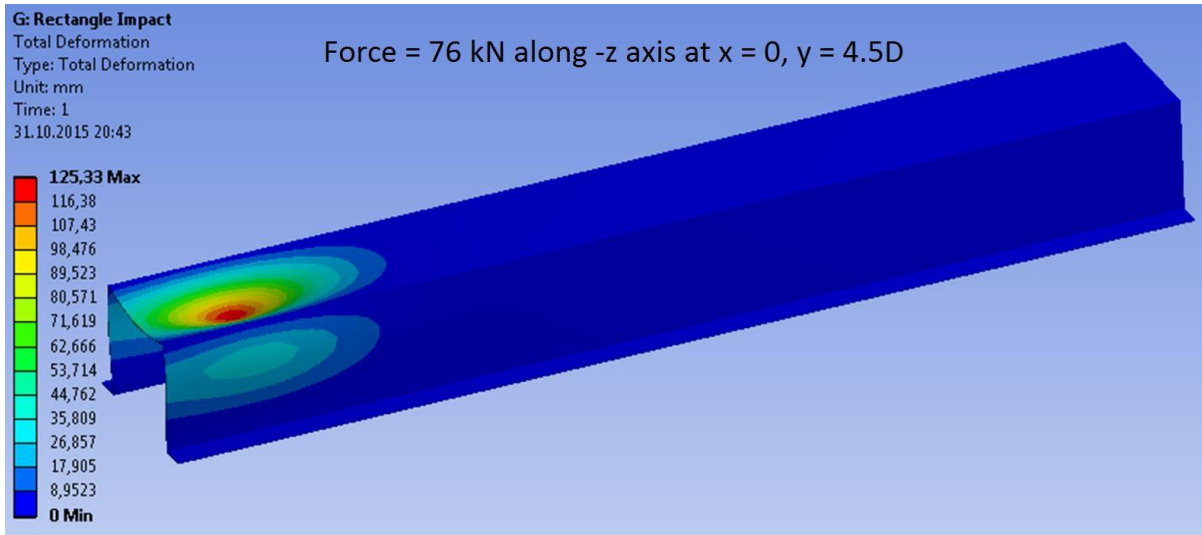




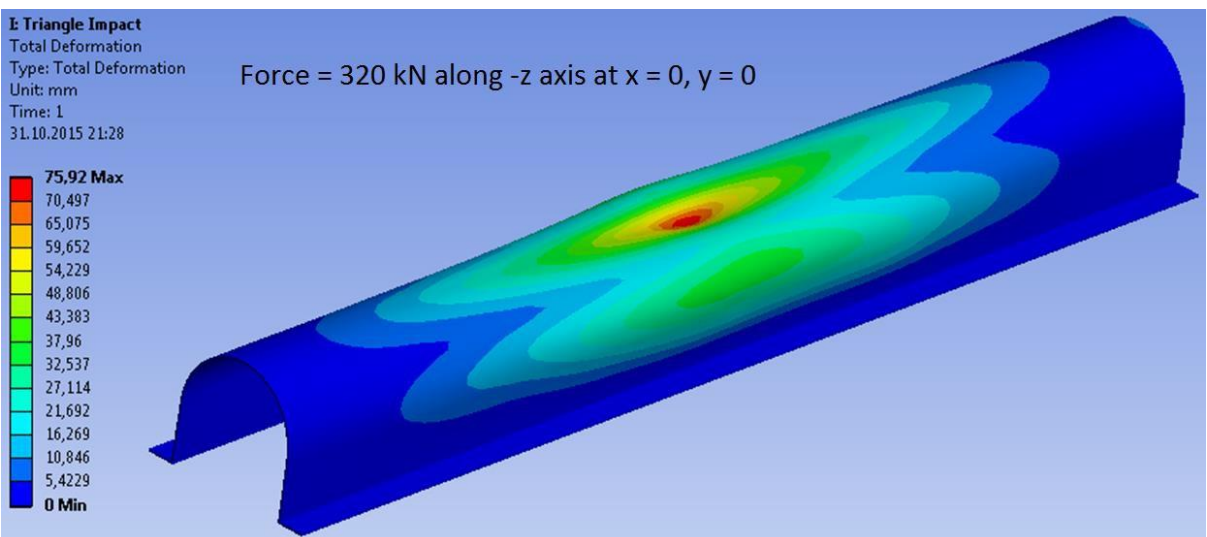
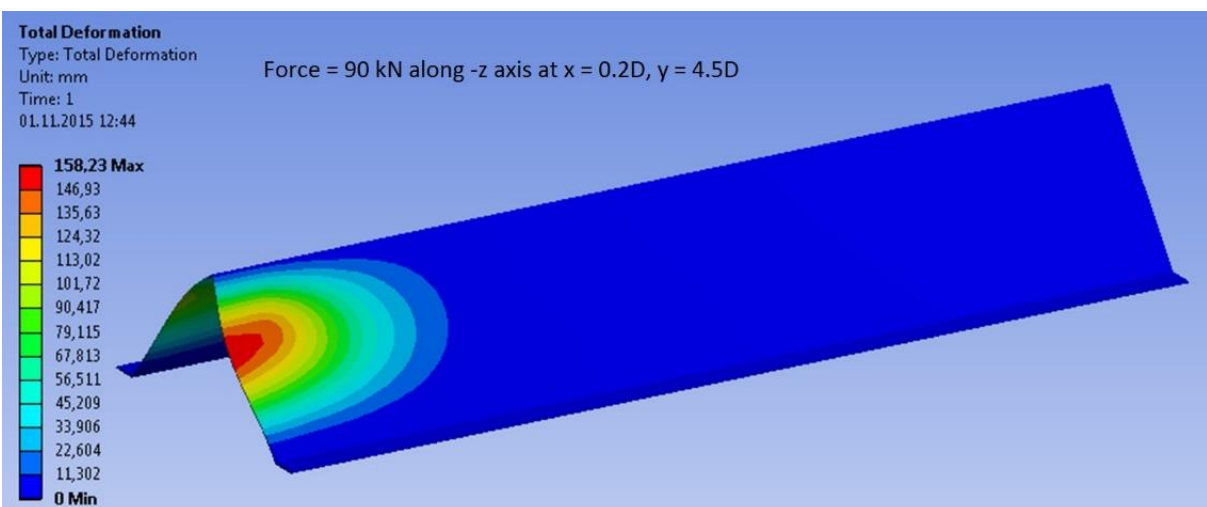
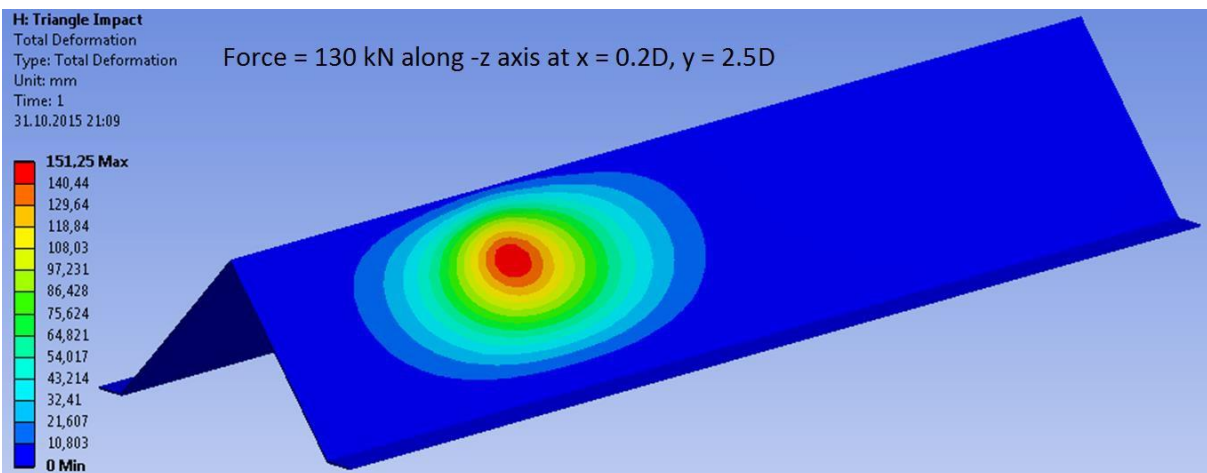
*Appendix D*

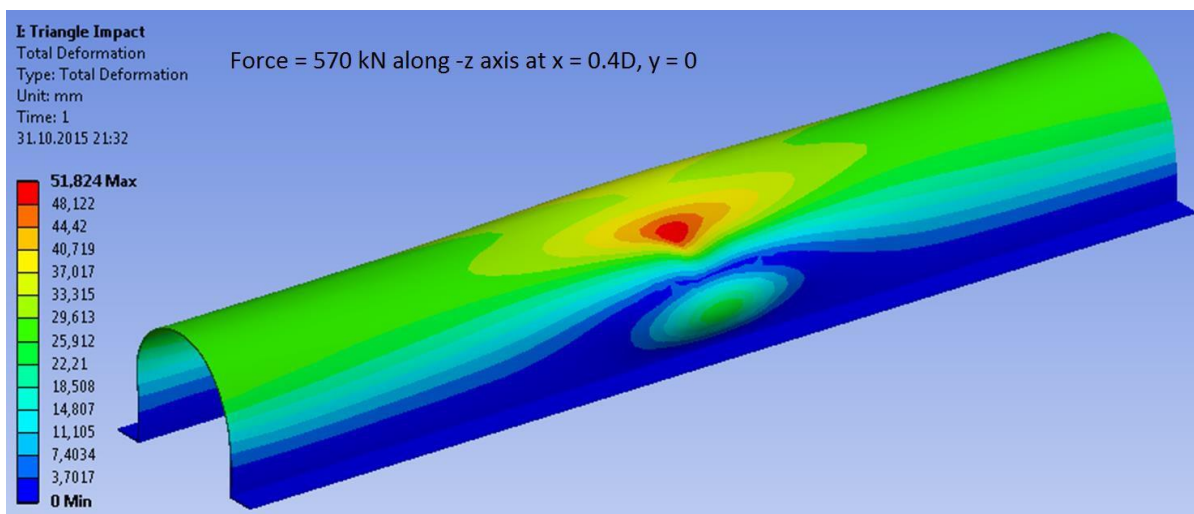
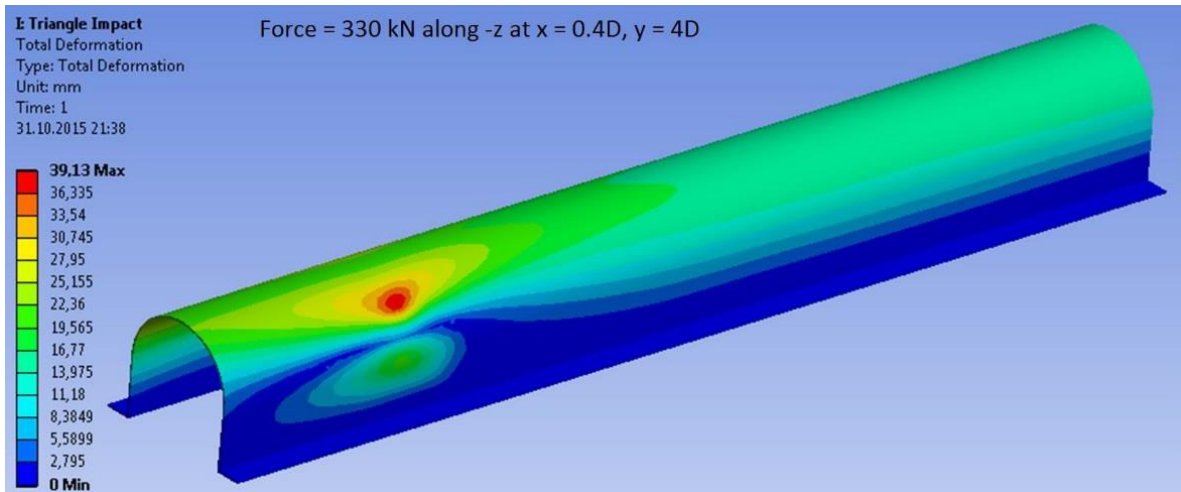
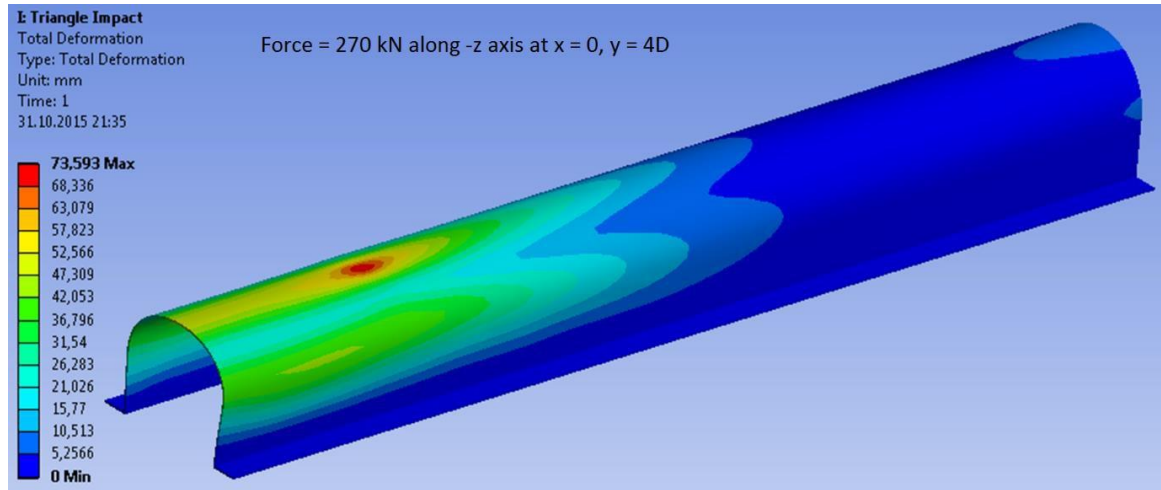
**Drop-object impact simulation results**













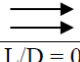
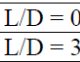
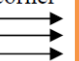
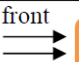
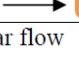
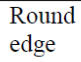
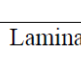
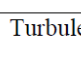

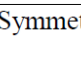

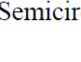

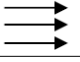

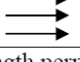


Drag coefficients of different shapes taken from Sadraey (2009):

No	Body	Laminar/turbulent	Status	$C_D$
1	Cube	$Re > 10,000$		1.05
2	Thin circular disk	$Re > 10,000$		1.1
3	Cone ( $\theta = 30^\circ$ )	$Re > 10,000$		0.5
4	Sphere	Laminar $Re \leq 2 \times 10^5$		0.5
		Turbulent $Re \geq 2 \times 10^6$		0.2
5	Ellipsoid	Laminar $Re \leq 2 \times 10^5$		0.3-0.5
		Turbulent $Re \geq 2 \times 10^6$		0.1-0.2
6	Hemisphere	$Re > 10,000$	Concave face	0.4
		$Re > 10,000$	Flat face	1.2
7	Rectangular plate	$Re > 10,000$	Normal to the flow	1.1 - 1.3
8	Vertical cylinder	$Re \leq 2 \times 10^5$	$L/D = 1$	0.6
			$L/D = \infty$	1.2
9	Horizontal cylinder	$Re > 10,000$	$L/D = 0.5$	1.1
			$L/D = 8$	1
10	Parachute	Laminar flow		1.3

b. Three dimensional bodies (L: length, D; diameter)

Drag coefficients of different shapes taken from Sadraey (2009):

No	Body	Status	Shape	$C_D$	
1	Square rod	Sharp corner		2.2	
		Round corner		1.2	
2	Circular rod	Laminar flow		1.2	
		Turbulent flow		0.3	
3	Equilateral triangular rod	Sharp edge face		1.5	
		Flat face		2	
4	Rectangular rod	Sharp corner		$L/D = 0.1$	1.9
				$L/D = 0.5$	2.5
				$L/D = 3$	1.3
		Round front edge		$L/D = 0.5$	1.2
				$L/D = 1$	0.9
				$L/D = 4$	0.7
5	Elliptical rod	Laminar flow		$L/D = 2$	0.6
				$L/D = 8$	0.25
		Turbulent flow		$L/D = 2$	0.2
				$L/D = 8$	0.1
6	Symmetrical shell	Concave face		2.3	
		Convex face		1.2	
7	Semicircular rod	Concave face		1.2	
		Flat face		1.7	

a. Two dimensional bodies (L: length along flow, D; length perpendicular to the flow)